January 2016

Density-to-Potential Inversions in Density Functional Theory

Daniel Spencer Jensen
Purdue University

Graduate School Form
30 Updated 12/26/2015

PURDUE UNIVERSITY
GRADUATE SCHOOL
Thesis/Dissertation Acceptance

This is to certify that the thesis/dissertation prepared

By Daniel Spencer Jensen

Entitled

Density-to-Potential Inversions in Density Functional Theory

For the degree of Doctor of Philosophy

Is approved by the final examining committee:

Adam Wasserman
Chair

Christopher H. Greene

Kenneth P. Ritchie

Yuli Lyanda-Geller

To the best of my knowledge and as understood by the student in the Thesis/Dissertation Agreement, Publication Delay, and Certification Disclaimer (Graduate School Form 32), this thesis/dissertation adheres to the provisions of Purdue University's "Policy of Integrity in Research" and the use of copyright material.

Approved by Major Professor(s): Adam Wasserman

Approved by: John P. Finley 19 July 2016

Head of the Departmental Graduate Program Date

DENSITY-TO-POTENTIAL INVERSIONS IN DENSITY FUNCTIONAL THEORY

A Dissertation

Submitted to the Faculty

of

Purdue University

by

Daniel S. Jensen

In Partial Fulfillment of the

Requirements for the Degree

of

Doctor of Philosophy

August 2016

Purdue University

West Lafayette, Indiana

This work is dedicated to my amazing wife Becky and wonderful children Spencer, Esther, Ammon, and Micah.

ACKNOWLEDGMENTS

I thank Peter Elliott and Kieron Burke for very helpful conversations and tutorials on density functional theory. A special thanks goes to Thomas Baker for computing several of the interacting one-dimensional densities using density matrix renormalization group techniques. I sincerely appreciate the help and support I received from the many members of the Suspenders' group. I am especially indebted to Jonathan Nafziger, Martín Mosquera and our fearless leader Adam Wasserman. I am very grateful for the funding we received from the National Science Foundation CAREER program under Grant No. CHE- 1149968.

TABLE OF CONTENTS

Page

LIST OF TABLES

LIST OF FIGURES

Figure Page

Figure Page

SYMBOLS

E_{p}	partition energy functional
E_{xc}	exchange-correlation functional
$\mathbf{j}$	particle current density of a system
m_e	mass of an electron
m_n	mass of a neutron
m_p	mass of a proton
n	particle density of a system
v_{p}	partition potential; functional derivative of E_{p}
v_{xc}	exchange-correlation potential; functional derivative of E_{xc}

ABBREVIATIONS

DFT	Density functional theory
KSDFT	Kohn-Sham density functional theory
PDE	Partial differential equation
PDFT	Partition density functional theory
PT	Partition theory
P-TDDFT	Time-dependent partition density functional theory
TDCDFT	Time-dependent current density functional theory
TDDFT	Time-dependent density functional theory
TDKS	Time-dependent Kohn-Sham

ABSTRACT

Jensen, Daniel S. Ph.D., Purdue University, August 2016. Density-to-Potential Inversions in Density Functional Theory. Major Professor: Adam Wasserman.

Density functional theory and many of its extensions are formally exact quantum many-body theories. In practice, however, implementations of these theories use approximations for all but the most trivial systems. We present a set of inversion methods to numerically compute the exact potentials corresponding to given input densities. The results of these inversions may then be used to evaluate the quality of different density functional approximations and guide the design of new approximations. The inversion methods use classical gradient-based optimization routines that are constrained to satisfy the governing partial differential equations. Numerous examples are given to illustrate the strengths and weaknesses of the different inversion methods.

1. Introduction

Sections 1.1-1.4 of this chapter have been adapted from the master's thesis entitled 'Real-space Time-domain Approach to Time Dependent Current Density Functional Theory' written by the author. [1]

Density functional theory (DFT) is a formally exact quantum many-body theory. It is usually applied to electronic structure problems where the nuclei are fixed and the electrons depend parametrically on the coordinates of the nuclei. The most popular implementation of DFT uses the Kohn-Sham auxiliary system and results in independent-particle equations that are usually solved self-consistently. In the Kohn-Sham approach to DFT all of the non-trivial many-body effects are placed in the exchange-correlation functional. This work focuses on the inverse problem of DFT, where the exchange-correlation potential for a model system is found from a given input density. The results of inverse problems in DFT are often used to test approximate exchange-correlation functionals and guide the development of new approximations.

1.1 The Quantum Many-Body Problem

The non-relativistic time-independent Hamiltonian of N electrons and K nuclei may be written in the coordinate representation as

$$\begin{aligned}\hat{H} \rightarrow & \overbrace{\sum_{i=1}^{N} \frac{-\Delta_i}{2}}^{T_{\mathrm{e}}} + \overbrace{\sum_{n=1}^{K} \frac{-\Delta_n}{2M_n}}^{T_{\mathrm{n}}} + \overbrace{\sum_{i=1}^{N} \sum_{j>i}^{N} \frac{1}{|\mathbf{r}_i - \mathbf{r}_j|}}^{V_{\mathrm{ee}}} \\ & + \overbrace{\sum_{n=1}^{K} \sum_{i=1}^{N} \frac{-Z_n}{|\mathbf{r}_i - \mathbf{R}_n|}}^{V_{\mathrm{en}}} + \overbrace{\sum_{n=1}^{K} \sum_{n'>n}^{K} \frac{Z_n Z_{n'}}{|\mathbf{R}_n - \mathbf{R}_{n'}|}}^{V_{\mathrm{nn}}},\end{aligned} \tag{1.1}$$

where M_n is the mass of the n$^{\text{th}}$ nucleus, Z_n is the charge of the n$^{\text{th}}$ nucleus, $\mathbf{R}_n$ is the position of the n$^{\text{th}}$ nucleus, $\mathbf{r}_i$ is the position of the i$^{\text{th}}$ electron, and $\Delta = \boldsymbol{\nabla}^2 = \boldsymbol{\nabla} \cdot \boldsymbol{\nabla}$ is the Laplacian. [2, Pg. 44] The first term T_{e} is the kinetic energy of the electrons, T_{n} is the kinetic energy of the nuclei, V_{ee} is the electron-electron potential energy, V_{en} is the electron-nucleus potential energy, and V_{nn} is the nucleus-nucleus potential energy. Equation 1.1 and all other equations in this dissertation are written in the system of atomic units where the unit of energy is the Hartree, which is about twice the ionization energy of hydrogen. [3, Pg. 4]

The many-body wave function Ψ corresponding to the Hamiltonian of Eq. (1.1) is the solution of the time-dependent Schrödinger equation

$$\imath \frac{\partial}{\partial t} \Psi(\mathbf{x}_1, \ldots, \mathbf{x}_N, \mathbf{R}_1, \ldots, \mathbf{R}_K, t) = \hat{H} \Psi(\mathbf{x}_1, \ldots, \mathbf{x}_N, \mathbf{R}_1, \ldots, \mathbf{R}_K, t)\,, \tag{1.2}$$

where $\mathbf{x}_i = (\mathbf{r}_i, \sigma_i)$ and σ_i is the spin coordinate of the i$^{\text{th}}$ electron. The wave function Ψ contains all of the information that can be known about the system at a given time t. [4, Pg. 28] Equation 1.2 is a linear partial differential equation (PDE) with $3M+3N$ spatial variables. Due to the extremely large number of variables in Eq. (1.2), direct solution methods are usually limited to extremely small systems of four particles or less [2, Pg. 44] or use stochastic-like techniques [5, Pg. 369].

1.2 The Born-Oppenheimer Approximation

A major reduction in the complexity of Eq. (1.2) results from separating the degrees of freedom of the nuclei and electrons in what is known as the Born-Oppenheimer approximation. For simplicity we will exclude time-dependent external fields in this introduction so that we can perform separation of variables on Eq. (1.2) and work with just the time-independent Schrödinger equation,

$$\hat{H} \Psi(\mathbf{x}_1, \ldots, \mathbf{x}_N, \mathbf{R}_1, \ldots, \mathbf{R}_K) = E \Psi(\mathbf{x}_1, \ldots, \mathbf{x}_N, \mathbf{R}_1, \ldots, \mathbf{R}_K)\,. \tag{1.3}$$

Equation (1.3) yields a set of eigenvalues E_k and eigenfunctions Ψ_k such that the general solution can be written as

$$\Psi = \sum_k c_k \exp\left(-\frac{\imath}{\hbar} E_k t\right) \Psi_k, \tag{1.4}$$

where the c_k are determined by the initial conditions of our system. [4, Pgs. 42-44]

At the heart of the Born-Oppenheimer approximation is the assumption that the wave function can be written as the product of a nuclear and electronic wave function with the electronic wave function depending only parametrically on the positions of the nuclei,

$$\Psi(\mathbf{x}_1, \ldots, \mathbf{x}_N, \mathbf{R}_1, \ldots, \mathbf{R}_K) = \Phi(\mathbf{x}_1, \ldots, \mathbf{x}_N; \mathbf{R}_1, \ldots, \mathbf{R}_K)\, \Theta(\mathbf{R}_1, \ldots, \mathbf{R}_K)\,, \tag{1.5}$$

where variables after the semicolons are fixed parameters. Using this approximation to replace Ψ in Eq. (1.1) we have the following pair of equations

$$\begin{aligned} H_{\text{elec}}\Phi(\mathbf{x}_1, \ldots, \mathbf{x}_N; \mathbf{R}_1, \ldots, \mathbf{R}_K) =& E_e(; \mathbf{R}_1, \ldots, \mathbf{R}_K) \\ & \cdot \Phi(\mathbf{x}_1, \ldots, \mathbf{x}_N; \mathbf{R}_1, \ldots, \mathbf{R}_K) \qquad (1.6) \\ \text{and } H_{\text{nuc}}\Theta(\mathbf{R}_1, \ldots, \mathbf{R}_K) =& E_n\Theta(\mathbf{R}_1, \ldots, \mathbf{R}_K)\,, \qquad (1.7) \end{aligned}$$

where H_{elec} is the electronic Hamiltonian

$$H_{\text{elec}} \to \overbrace{\sum_{i=1}^{N} \frac{-\Delta_i}{2}}^{T_{\text{e}}} + \overbrace{\sum_{i=1}^{N}\sum_{j>i}^{N} \frac{1}{|\mathbf{r}_i - \mathbf{r}_j|}}^{V_{\text{ee}}} + \overbrace{\sum_{n=1}^{K}\sum_{i=1}^{N} \frac{-Z_n}{|\mathbf{r}_i - \mathbf{R}_n|}}^{V_{\text{en}}} \tag{1.8}$$

and H_{nuc} is the nuclear Hamiltonian

$$H_{\text{nuc}} \to \overbrace{\sum_{n=1}^{K} \frac{-\Delta_n}{2M_n}}^{T_{\text{n}}} + E_e + \overbrace{\sum_{n=1}^{K}\sum_{n'>n}^{K} \frac{Z_n Z_{n'}}{|\mathbf{R}_n - \mathbf{R}_{n'}|}}^{V_{\text{nn}}}. \tag{1.9}$$

In deriving these equations we have neglected the two terms

$$-\Theta(\mathbf{R}_1,\ldots,\mathbf{R}_K)\sum_{n=1}^{K}\frac{1}{2M_n}\Delta_{\boldsymbol{R}_n}\Phi(\mathbf{x}_1,\ldots,\mathbf{x}_N;\,\mathbf{R}_1,\ldots,\mathbf{R}_K)\ \text{and} \tag{1.10a}$$

$$-\sum_{n=1}^{K}\frac{1}{M_n}\boldsymbol{\nabla}_{\boldsymbol{R}_n}\Theta(\mathbf{R}_1,\ldots,\mathbf{R}_K)\cdot\boldsymbol{\nabla}_{\boldsymbol{R}_n}\Phi(\mathbf{x}_1,\ldots,\mathbf{x}_N;\,\mathbf{R}_1,\ldots,\mathbf{R}_K) \tag{1.10b}$$

on the basis that they are small contributions as explained in Ref. [2, Pg. 81].

Simple justification for the Born-Oppenheimer approximation comes from the fact that the nuclei are much more massive than the electrons, ($m_n/m_e \approx 1839$ and $m_p/m_e \approx 1836$), and therefore move much slower on average. The result of this approximation as seen in Eqs. (1.6) and (1.7) is that we have a clear separation of the degrees of freedom of the electrons from those of the nuclei. In the remainder of this document we will focus mainly on the electronic structure problem of Eq. (1.6). The main disadvantage to using the Born-Oppenheimer approximation is that electron-phonon couplings are neglected and their effects must be studied perturbatively when using this approximation.

1.3 Density Functional Theory

Although the Hamiltonian in Eq. (1.8) is greatly simplified over that of Eq. (1.1) it is still intractable due to the large number of degrees of freedom stemming from the V_{ee} term. There are several approaches that attack this problem by replacing this complicated term with an effective potential V_{eff} resulting in a Hamiltonian that is simply a sum of one-electron Hamiltonians,

$$H_{\text{IP}} \to \sum_{i=1}^{N}\left[\overbrace{\frac{-\Delta_i}{2}}^{T_{\text{e}}} + V_{\text{eff}}(\mathbf{x}_i;\,\mathbf{R}_1,\ldots,\mathbf{R}_K) + \overbrace{\sum_{n=1}^{K}\frac{-Z_n}{|\mathbf{r}_i-\mathbf{R}_n|}}^{V_{\text{en}}}\right] \tag{1.11}$$

where H_{IP} is called the 'independent-particle' Hamiltonian.[1] Some approaches, such as the Hartree-Fock approximation, achieve this replacement by treating the term approximately in a manner similar to the mean field theory approach of statistical mechanics. [2, Pg. 47] Other approaches, such as DFT and some post-Hartree-Fock methods, attempt to include all of the effects of V_{ee} in a systematic way while still using an independent-particle Hamiltonian. Although each approach has its advantages and disadvantages, we choose to focus on DFT due to its ability to handle very large numbers of electrons. It should be noted that the potential V_{eff} in Eq. (1.11) is, in general, a nonlocal operator that depends on the same wave function that it is acting upon. This nonlocality in V_{eff} leads to a nonlinear set of equations that are usually solved self-consistently.

As mentioned above, DFT is particularly useful for solving Eq. (1.8) because it can be used to model large finite and periodic systems. (See Ref. [6, Ch. 23] for some examples of large systems including giant fullerenes and DNA molecules.) This is made possible mainly by working with the particle density

$$n(\mathbf{r}) = \frac{\langle \Phi \left| \hat{n}(\mathbf{r}) \right| \Phi \rangle}{\langle \Phi \mid \Phi \rangle} = N \frac{\sum_{\sigma_1} \int \mathrm{d}\mathbf{x}_2 \cdots \mathrm{d}\mathbf{x}_N \left| \Phi(\mathbf{r}, \sigma_1, \mathbf{x}_2, \ldots, \mathbf{x}_N) \right|^2}{\int \mathrm{d}\mathbf{x}_1 \mathrm{d}\mathbf{x}_2 \cdots \mathrm{d}\mathbf{x}_N \left| \Phi(\mathbf{x}_1, \mathbf{x}_2 \ldots, \mathbf{x}_N) \right|^2}, \tag{1.12}$$

where $\hat{n}(\mathbf{r}) = \sum_{i=1}^{N} \delta(\mathbf{r} - \mathbf{r}_i)$ is the density operator. [6, Pg. 54] Notice that $n(\mathbf{r})$ in Eq. (1.12) only depends on 3 spatial variables in comparison with the $3N$ spatial variables that the complicated many-body electronic wave function in Eq. (1.6) depends on. (Here we are still assuming that there are N electrons.) Justification for this switch in focus from wave function to density comes from the Hohenberg-Kohn theorems described below.

The two Hohenberg-Kohn theorems developed in 1964 form the theoretical foundation of DFT. [7] The main result of the first Hohenberg-Kohn theorem is that all

[1] The V_{en} term in Eq. (1.11) is usually called the external potential V_{ext} in DFT and does not have to be the electron-nucleus interaction for DFT to be valid.

properties of a system obeying Eq. (1.6) can be found using only the ground state density

$$n_0(\mathbf{r}) = \frac{\langle \Phi_0 | \hat{n}(\mathbf{r}) | \Phi_0 \rangle}{\langle \Phi_0 \mid \Phi_0 \rangle}, \tag{1.13}$$

where Φ_0 is the ground-state wave function. The main result of the second Hohenberg-Kohn theorem is that there exists a universal functional of the density $E[n]$ with a global minimum equal to the exact ground-state energy for any given external potential. The density that minimizes this functional is the exact ground state density so by combining the two theorems we see that if we have the correct energy functional $E[n]$ then we have an *exact* theory of many-body systems appropriately named density functional theory. [6, Sec. 6.2] That such a functional exists was clarified later in the constrained search formulation of Levy and Lieb, which hinges on the ability to express the density in terms of an N-electron wave function. [6, Pg. 126]

1.4 The Kohn-Sham Approach

The Hohenberg-Kohn theorems provide a theoretical foundation for DFT but they do not describe a procedure for actually finding the functional $E[n]$ in the second Hohenberg-Kohn theorem. One procedure was provided by Kohn and Sham in 1965 [8] and is the reason why DFT has become such a powerful tool in electronic structure calculations. In this approach the functional in the second Hohenberg-Kohn theorem is written as[2]

$$E[n] = T_s[n] + \int \mathrm{d}\mathbf{r}\, n(\mathbf{r})\, V_{\mathrm{en}}(\boldsymbol{r}) + E_{\mathrm{H}}[n] + E_{\mathrm{xc}}[n]\,, \tag{1.14}$$

where T_s is the kinetic energy functional of a noninteracting electron gas, E_{H} is the classical Coulomb interaction functional

$$E_{\mathrm{H}}[n] = \frac{1}{2} \int \mathrm{d}\mathbf{r} \int \mathrm{d}\mathbf{r}' \frac{n(\mathbf{r})\, n(\mathbf{r}')}{|\mathbf{r} - \mathbf{r}'|} \tag{1.15}$$

[2]This energy functional is only well-defined for periodic systems if we add the ion-ion interaction energy functional to make the system neutral.

and E_{xc} is the exchange-correlation functional representing the energy from all correlation effects[3] and any other energy not accounted for in the other three terms.

Applying the calculus of variations to Eq. (1.14) results in the Kohn-Sham (KS) Schrödinger-like equations,

$$\epsilon_k \phi_k^\sigma(\mathbf{r}) = \left[-\frac{\Delta}{2} + V_{\text{eff}}^\sigma\left(\left[n^\uparrow, n^\downarrow\right], \mathbf{r}\right) \right] \phi_k^\sigma(\mathbf{r}) \,, \tag{1.16a}$$

$$n(\mathbf{r}) = \sum_{\sigma=\uparrow,\downarrow} n(\mathbf{r}, \sigma) = \sum_{\sigma=\uparrow,\downarrow} \sum_{k=1}^{N^\sigma} \left|\phi_k^\sigma(\mathbf{r})\right|^2 , \tag{1.16b}$$

$$V_{\text{eff}}^\sigma\left(\left[n^\uparrow, n^\downarrow\right], \mathbf{r}\right) = V_{\text{en}}(\mathbf{r}) + V_{\text{H}}([n], \mathbf{r}) + V_{\text{xc}}^\sigma\left(\left[n^\uparrow, n^\downarrow\right], \mathbf{r}\right) , \tag{1.16c}$$

where $V_{\text{xc}}^\sigma = \frac{\delta E_{\text{xc}}\left[n^\uparrow, n^\downarrow\right]}{\delta n^\sigma}$ is the exchange-correlation potential and

$$V_{\text{H}}([n], \mathbf{r}) = \int \mathrm{d}\mathbf{r}' \, n(\mathbf{r}') \, \frac{1}{|\mathbf{r} - \mathbf{r}'|} \tag{1.17}$$

is the Hartree potential. These equations are of the desired independent-electron form shown in Eq. (1.11) but must be solved self-consistently since the potential V_{eff}^σ depends on the spin densities $n^\uparrow$ and $n^\downarrow$, which in turn depends on the unknown independent-electron orbitals $\left\{\phi_k^\uparrow\right\}$ and $\left\{\phi_k^\downarrow\right\}$. As seen in Eq. (1.16), the KS approach rests on the assumption that the true ground-state electron density can be written as the density of an independent-electron system.[4] This assumption is known as the KS *ansatz* and has been proven for discretized systems. [9] If the KS *ansatz* is true for a given system then the KS approach will, in principle, solve Eq. (1.6) exactly.

The KS approach to DFT is very powerful because the exchange-correlation energy is generally a small contribution to the total energy and is independent of the external potential $V_{\text{en}}(\boldsymbol{r})$. [10] Although the exact exchange-correlation functional is not known, hundreds of exchange-correlation approximations have been proposed and

[3] Exchange is just a special form of correlation stemming from the Pauli exclusion principle.
[4] The Kohn-Sham ansatz is often referred to in DFT literature as the noninteracting-v-representability question.

are readily available for inclusion in DFT programs. [11] These approximations typically treat E_{xc} as a local or nearly local functional of the density. [6] Despite the large number of approximate exchange-correlation functionals, there is a continual effort to improve their accuracy, generality, and reliability to better predict the electronic structure of matter. [10]

The KS method described above can be generalized and applied to a wider range of problems. [6, Pg. 148] Time-dependent density functional theory (TDDFT) extends DFT into the time domain and allows us to describe excitations. Partition density functional theory (PDFT) and its time-dependent extension are two more generalizations that allow us to work intuitively with fragments. These generalizations and others often require approximations to new functionals and their corresponding functional derivatives. A basic introduction to these generalizations is presented in Chs. 3-5.

1.5 Density-to-Potential Inverse Problems

In the direct problem of DFT we use an approximate exchange-correlation potential to solve the KS equations [Eq. (1.16)] for the unknown density. In the inverse problem of DFT, the KS equations are used to find the exchange-correlation potential from a known density. This difference in input and output variables is shown in Tab. 1.1 and leads to major differences in solution methods for the two problems. We refer to the inverse problem of DFT as a density-to-potential inversion and the numerical methods required for solving this problem are the main focus of this work. In this section we give a brief introduction to inverse problems and explain how density-to-potential inversions can be used within DFT.

Inverse problems are common in science and have been central in quantum mechanics since its inception. Much of what we know about the structure of matter has come from scattering experiments, [4, Pg. 278] which can be described mathematically as inverse problems. A variety of mathematical and numerical techniques exist

Table 1.1.
Input and output of the direct and inverse DFT problems.

Problem	Input	Output
Direct	V_{xc}^{σ}	n
Inverse	n	V_{xc}^{σ}

for solving scattering problems as well as other inverse problems. [12] These methods are often very different from the methods used for solving the direct problems due to the inverse problems' mathematical structure and input data.

According to Hadamard, [13] a problem is well-posed if a solution exists, it is unique, and it depends continuously on the data. If any of the three properties listed above are violated then the problem is ill-posed. The forward or direct problem of DFT is well-posed thanks to the proofs mentioned in Sec. 1.3 and the usually analytic nature of the functionals in Eq. (1.14). The inverse problem of DFT can also be well-posed for discretized systems as proven in Ref. 9 but often errors and missing information in the input density lead to the violation of Hadamard's well-posed conditions. In such cases special precautions must be taken in designing inversion methods that converge to the true solution of the inverse problem.

Regularization is the general term used to describe a method for solving ill-posed problems. Some regularization methods are as simple as stopping an optimization according to an a posteriori parameter choice rule while others, such as total variation, can be sophisticated and very challenging mathematical and programming exercises. [14, Pg. 9] Often the form of regularization is chosen to penalize features known to be incorrect based on a priori information about the solution. For a thorough review of regularization and inverse problem theory see Refs. 14–16. The density-to-potential inversion methods presented in this work are designed explicitly to include regularization when needed.

By designing our inversion methods to include regularization, we are able to build robust algorithms that do not rely on inverse crimes. The term 'inverse crime' is commonly used in inverse problem theory to describe an inversion method relying

on a cancellation of errors between the data simulation and reconstruction methods. [16, Pg. 7] Inverse crimes are often committed in DFT inversions when the same discretization is used for both the direct and inverse problems. Inversion methods that rely on inverse crimes are very limiting in the number of systems that can be studied and will likely fail when applied to experimental data.

One possible motivation for studying the inverse problem of DFT is to benchmark the many approximate exchange-correlation functionals mentioned in Sec. 1.4. Benchmarking is usually done on model systems where the density is either known analytically or found numerically through a direct solution of the electronic Schrödinger equation [Eq. (1.6)]. As seen in Ch. 2, major features of the exact exchange-correlation potential are often found to be missing in popular approximations and thus the inverse problem can help guide the development of new approximations.

Perhaps an even more important reason to study the inverse problem of DFT comes from its connection with the optimized effective potential (OEP) method. In the OEP method the exchange-correlation functional is an explicit functional of the KS orbitals and therefore an implicit functional of the density. As pointed out in Ref. [17], the optimization procedures used in the OEP method can be adapted to perform density-to-potential inversions and vice versa. Similarly, when TDDFT is applied to problems in quantum optimal control theory (QOCT) the resulting equations and algorithms are very similar to the algorithms used in the time-dependent density-to-potential inversions. These connections with the OEP method and QOCT show that density-to-potential inversions are also important predictive tools in addition to their use in benchmarking approximate functionals.

1.6 Overview

The preceding sections serve as a very general introduction to DFT and density-to-potential inversions. In this section we summarize the tools and theory used throughout the remainder of this work. A visual depiction of these tools and theory can be

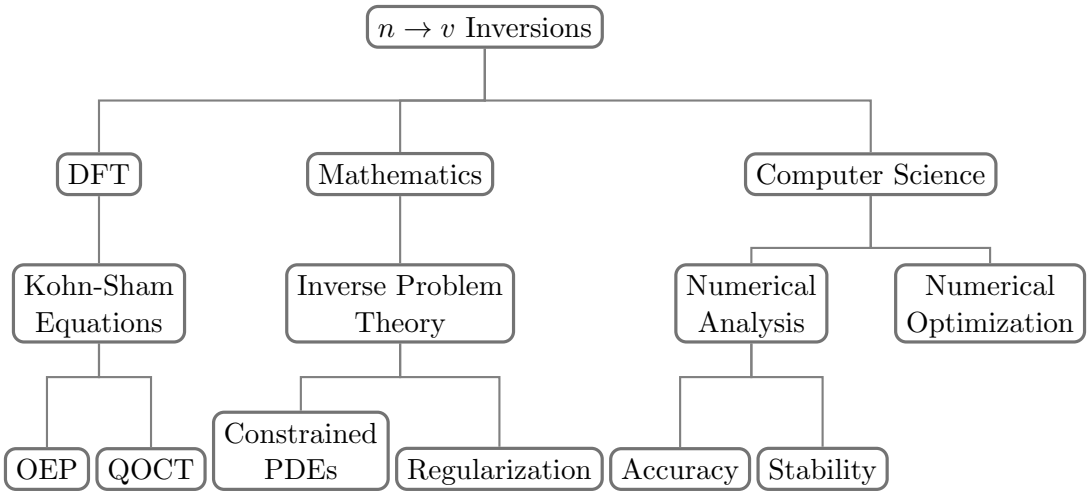

Figure 1.1. A tree diagram showing the tools and theory involved in density-to-potential inversions.

seen in Fig. 1.1. We also describe the scope of the document and some properties of our inversion algorithms that are common to all of the methods presented in Chs. 2-5.

As explained in Sec. 1.5, we are primarily concerned with finding the exchange-correlation potentials of different target densities. Some inversion methods are also capable of finding the value of the exchange-correlation functional evaluated at a given target density. [17] Not all of our methods are capable of recovering this information and it is not discussed further in this work.

We make a special effort to verify the integrity and robustness of our inversion algorithms presented in Chs. 2-5. Our test cases are mostly noninteracting systems because we can focus just on recovering the known external potential. These systems may seem trivial but the inverse problems are just as difficult as the inverse problems corresponding to interacting densities and provide great insight into the design of inversion algorithms. We also strive to use different algorithms and grids for the direct problems in the cases that we don't have analytic formulas for the target densities. This is not strictly necessary but helps avoid any reliance on inverse crimes as described in Sec. 1.5. The numerical errors in both the inversion methods and

the target densities used as input are also tracked carefully to avoid problems with overfitting. In general, a great deal of numerical analysis is used throughout this work to make sure that our inversion methods are both correct and efficient.

All of the examples in this work are one-dimensional systems for simplicity but the formulas are written for multidimensional systems to aid future development. We use the finite difference method for our calculations similar to the Octopus TDDFT code. [18] The finite difference method has proven to be capable of producing distributional solutions and other sharp features that would be difficult to find using basis sets. We also limit our studies to spin-compensated systems and drop the spin index on most formulas. For better agreement with common notation in DFT, we use lowercase letters for the potentials and refer to the electron-nucleus potential as the external potential (i.e. $V_{\text{en}} = v_{\text{ext}}$).

Chapter 2 contains a more in-depth description of the KS equations and a variety of numerical methods for solving both the direct and inverse problems of DFT. Chapters 3-5 discuss PDFT, TDDFT, and partition time-dependent density functional theory (P-TDDFT) in relation to density-to-potential inversions. We conclude in Ch. 6 with a brief summary of the different inversion methods presented in this work and several proposals for improving them.

2. Inversions in Density Functional Theory

In this chapter we explore density functional theory (DFT) within the Kohn-Sham (KS) formalism. We examine both the direct and inverse problems of DFT with a special emphasis on the algorithms for solving the inverse problem. Two new inversion methods based on PDE-constrained optimization and constrained variational methods are introduced in Secs. 2.3.3 and 2.3.4. We compare and constrast the different inversion methods using several one-dimensional model systems.

2.1 Density Functional Theory

The intent of this section is to delve deeper into the mathematical structure of the KS equations already introduced in Sec. 1.4. Although the direct and inverse problems of DFT share the same KS equations, there are several important differences between them that we highlight in this section. These differences lead to very different algorithms and convergence criteria as seen in Secs. 2.2-2.3.

The KS equations for a closed-shell system with $2N$ electrons can be written as

$$\varepsilon_j \underline{\phi_j(\mathbf{r})} = \left[-\frac{\Delta}{2} + v_{\mathrm{KS}}([\underline{n}], \mathbf{r}) \right] \underline{\phi_j(\mathbf{r})}, \tag{2.1a}$$

$$\underline{n(\mathbf{r})} = 2 \sum_{j=1}^{N} \left| \underline{\phi_j(\mathbf{r})} \right|^2, \tag{2.1b}$$

$$v_{\mathrm{KS}}([\underline{n}], \mathbf{r}) = v_{\mathrm{ext}}(\mathbf{r}) + v_{\mathrm{H}}([\underline{n}], \mathbf{r}) + v_{\mathrm{xc}}([\underline{n}], \mathbf{r}), \tag{2.1c}$$

where the orbitals are constrained to be orthonormal:

$$\langle \phi_j | \phi_k \rangle = \delta_{j,k} = \begin{cases} 1 & \text{if } j = k \\ 0 & \text{otherwise} \end{cases}. \tag{2.2}$$

The potentials in Eq. (2.1) are defined in Sec. 1.4 and the underlined quantities are unknown when solving the direct problem. The orbitals are usually chosen such that their corresponding eigenvalues $\{\varepsilon_j\}$ form the set of lowest possible eigenvalues. The KS equations for the inverse problem of DFT

$$\varepsilon_j \underline{\phi_j(\mathbf{r})} = \left[-\frac{\Delta}{2} + v_{\mathrm{KS}}([n]\,,\mathbf{r})\right] \underline{\phi_j(\mathbf{r})}, \tag{2.3a}$$

$$n(\mathbf{r}) = 2\sum_{j=1}^{N} \left|\underline{\phi_j(\mathbf{r})}\right|^2, \tag{2.3b}$$

$$v_{\mathrm{KS}}([n]\,,\mathbf{r}) = v_{\mathrm{ext}}(\mathbf{r}) + v_{\mathrm{H}}([n]\,,\mathbf{r}) + \underline{v_{\mathrm{xc}}([n]\,,\mathbf{r})}, \tag{2.3c}$$

only differ from the direct problem in the unknowns as indicated by underlining.

Equation (2.1a) is a nonlinear eigenvalue problem due to the KS potential's density dependence whereas Eq. (2.3a) is a linear eigenvalue problem. The inverse problem is still nonlinear but the nonlinearity comes from the definition of the density shown in Eq. (2.3b). This subtle difference in nonlinearity means that the mixing schemes prevalent in numerical methods for the direct problem, (see, e.g., Sec. 2.2), are not needed in solving the eigenvalue problem in Eq.(2.3a). Additionally, the definition of the density in Eq. (2.3b) puts constraints on the values of the KS orbitals when solving the inverse problem that aren't present in the direct problem. These additional constraints are exploited in the inversion method described in Sec. 2.3.4. Finally, the nonlinearity in both problems makes the choice of initial guess very important as convergence is not guaranteed in many numerical methods when poor initial guesses are used. [5]

The KS equations apply to both finite and extended systems provided that the appropriate boundary conditions are applied. In the direct problem of DFT the orbitals are usually constrained to satisfy periodic or box-type (Dirichlet) boundary conditions as dictated by the system being studied. [19] In the inverse problem the boundary conditions only need to be correctly represented in the Laplacian and the density constraint forces the orbitals to have the correct behavior at the boundaries.

If boundary conditions are imposed on the orbitals in the inverse problem then it is important that they agree with the density constraint as explained in Sec. A.1.

As mentioned in Sec. 1.5, uniqueness is a key ingredient in solving both direct and inverse problems. Although the density in DFT is a unique quantity in both the forward and inverse problems, the KS orbitals that it is built from are not unique. As seen in Eq. (2.1b), the density is formed from the absolute value squared of the orbitals and therefore the orbitals can only be unique up to a phase factor. Furthermore, any unitary transformation of the KS orbitals will also produce the same density and some variational methods can exploit this property to speed up convergence as seen in Sec. 2.3.4. The potentials in Eq. (2.1c) are also a source of nonuniqueness as they are only unique up to a constant. [9]. As seen in Sec. 2.3, most density-to-potential inversion methods force the unknown potential to be unique by imposing restrictions of some form.

Convergence in the direct problem of DFT is usually achieved by refining the discretization of the system by adding more basis functions, plane waves, grid points, etc. [6] Since the potentials are usually given by analytic formulas, the KS equations can be solved to a prescribed tolerance dependent only on the level of discretization employed. In the inverse problem of DFT, convergence is limited by both the discretization method and the quality of the target density. Although most of the test cases presented in this work have analytic formulas for the target densities, most target densities of real interest are not known analytically. If the numerical error present in a given target density is not accounted for properly in a density-to-potential inversion then overfitting becomes a problem and unphysical features develop in the recovered potential. Examples of overfitting and convergence limits related to the relative error of the target density are given in Sec. A.1.

2.2 Direct-Problem Methods

A variety of numerical methods for solving the KS equations exist and can be placed in essentially three different categories: plane waves and grid methods, localized atomic-(like) orbitals, and atomic sphere methods. [6] We use the finite difference grid method throughout this work due to its simplicity and for other reasons mentioned in Sec. 1.6. In this section we review several aspects of the finite difference formulation of DFT that are necessary for solving the direct problem and also relevant to some of the inverse problem methods in Sec. 2.3. A more thorough review of the finite difference method applied to DFT can be found in Ref. 20.

The orbitals, potentials, and density in the KS equations are represented as discrete points on a grid when using the finite difference method. The potentials are diagonal in the coordinate representation and the Laplacian is a very sparse matrix operator depending on the approximation used. An example fourth-order Laplacian with box-type boundary conditions on a regularly spaced grid with ten points is

$$\frac{1}{h^2}\begin{bmatrix} \frac{15}{4} & -\frac{77}{6} & \frac{107}{6} & -13 & \frac{61}{12} & -\frac{5}{6} & 0 & 0 & 0 & 0 \\ \frac{5}{6} & -\frac{5}{4} & -\frac{1}{3} & \frac{7}{6} & -\frac{1}{2} & \frac{1}{12} & 0 & 0 & 0 & 0 \\ -\frac{1}{12} & \frac{4}{3} & -\frac{5}{2} & \frac{4}{3} & -\frac{1}{12} & 0 & 0 & 0 & 0 & 0 \\ 0 & -\frac{1}{12} & \frac{4}{3} & -\frac{5}{2} & \frac{4}{3} & -\frac{1}{12} & 0 & 0 & 0 & 0 \\ 0 & 0 & -\frac{1}{12} & \frac{4}{3} & -\frac{5}{2} & \frac{4}{3} & -\frac{1}{12} & 0 & 0 & 0 \\ 0 & 0 & 0 & -\frac{1}{12} & \frac{4}{3} & -\frac{5}{2} & \frac{4}{3} & -\frac{1}{12} & 0 & 0 \\ 0 & 0 & 0 & 0 & -\frac{1}{12} & \frac{4}{3} & -\frac{5}{2} & \frac{4}{3} & -\frac{1}{12} & 0 \\ 0 & 0 & 0 & 0 & 0 & -\frac{1}{12} & \frac{4}{3} & -\frac{5}{2} & \frac{4}{3} & -\frac{1}{12} \\ 0 & 0 & 0 & 0 & \frac{1}{12} & -\frac{1}{2} & \frac{7}{6} & -\frac{1}{3} & -\frac{5}{4} & \frac{5}{6} \\ 0 & 0 & 0 & 0 & -\frac{5}{6} & \frac{61}{12} & -13 & \frac{107}{6} & -\frac{77}{6} & \frac{15}{4} \end{bmatrix}, \tag{2.4}$$

where h is the grid spacing. Different orders of approximate finite difference operators can be derived using the algorithm described in Ref. 21. Custom meshes can also be used that conform to the geometry of a given system as explained in Ref. 19. One

disadvantage of the finite difference method applied to DFT is the lack of a variational principle but this can be remedied using the formulation given in Ref. [22] if needed.

A variety of numerical algorithms are available for computing the potentials in Eq. (2.1c). The Hartree potential v_{H} shown in Eq. (1.17) is equivalent to the Poisson equation

$$\Delta v(\mathbf{r}) = -4\pi n(\mathbf{r}) \tag{2.5}$$

and has been studied extensively. The fast Fourier transform, fast multipole method, and conjugate gradient methods are just a few of the available algorithms for computing v_{H}; a thorough review of these methods can be found in Ref. 23. Since most of the interacting examples in this work are one-dimensional and use custom electron-electron interaction potentials, we use direct numerical integration to compute the interaction potential via the formula

$$v_{\mathrm{H}}([n]\,,\mathbf{r}) = \int \mathrm{d}\mathbf{r}'\, n(\mathbf{r}')\, v_{\mathrm{ee}}\left(\mathbf{r}-\mathbf{r}'\right). \tag{2.6}$$

As explained in Sec. 1.4, there are many approximate exchange-correlation functionals and corresponding potentials. The LIBXC library contains a wide selection of these approximations and is easily incorporated in DFT programs. [11] Exchange-correlation approximations can also be derived for systems with custom electron-electron interactions as shown in Refs. 24 and 25.

The KS equations are usually solved using sparse matrix eigenvalue solvers in contrast to the dense solvers typically used in basis-set methods. [20] The examples in this work use the `eigs` and `eig_banded` eigenvalue solvers in the SciPy library, which are interfaces to routines in the LAPACK and ARPACK libraries respectively. [26] These solvers are capable of computing the eigenvalues and eigenvectors of a sparse matrix to machine precision and are very efficient when only a few eigenvalues and eigenvectors are needed. If the potentials used in a given calculation are exact and the solvers are allowed to converge to machine precision then the majority of the numerical error will come from the discretization of the Laplacian. An example of this error is shown in

Fig. 2.1 for the ground state density of the harmonic oscillator using a second-order approximate Laplacian. Although the majority of the error is in the central region, Fig. 2.2 shows that the relative error is actually largest in the asymptotic regions. The approximate finite difference operators are very accurate in regions where the orbitals are well represented by polynomials and are less accurate in the asymptotic region where the orbitals are dominated by exponential decay. The large relative error is largely inconsequential for most direct DFT problems with almost no effect on the total energies but it does play a strong role in the inverse problem as shown in Sec. 2.3. This example also shows that the errors in most direct DFT problems are systematic rather than random noise typical of experimental data and must also be accounted for in the inverse problem as explained in App. A.

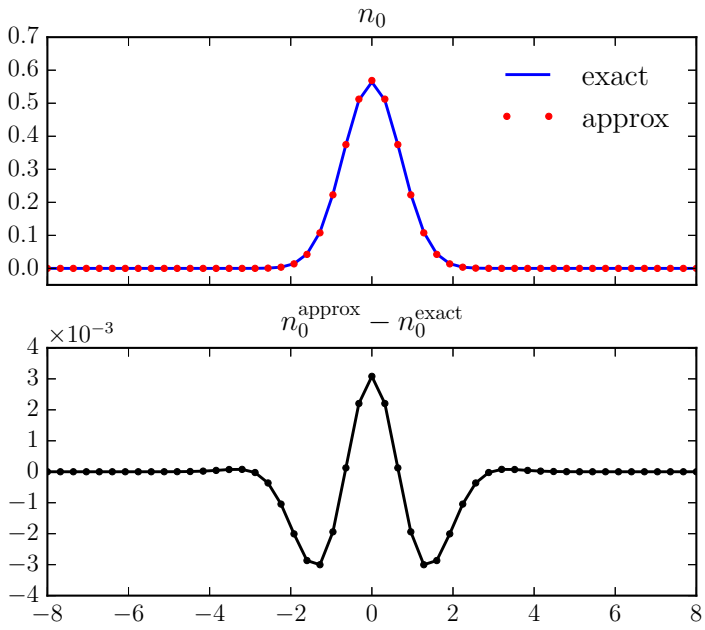

Figure 2.1. The ground state density of the harmonic oscillator compared to a numerical approximation using the EIG_BANDED routine and a second-order finite difference approximation to the Laplacian (top). The majority of the error is in the high-density central region (bottom).

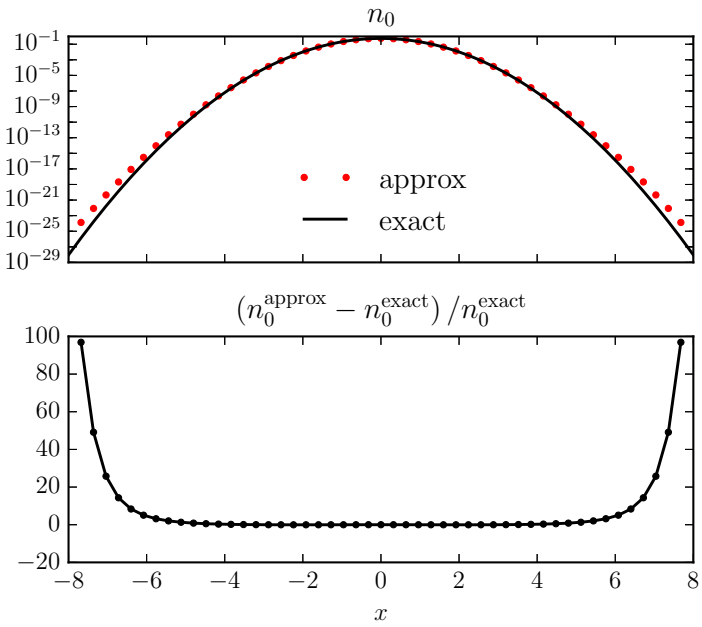

Figure 2.2. The same densities displayed in Fig. 2.1 are displayed on a logarithmic scale (top). The relative error in the asymptotic regions is orders of magnitude larger than the relative error in the central region (bottom).

The previous example of a noninteracting system only required solving one eigenvalue problem but a typical DFT calculation for an interacting system requires multiple eigenvalue solves in what is known as the self-consistent field (SCF) method. The initial density guess for a given system is inserted into the right-hand side of Eq. (2.1a), the eigenvalue problem is solved for a new set of orbitals, the orbitals are inserted into Eq. (2.1b) to produce a new density, and the cycle repeats until a convergence criterion is reached. This method is usually modified to avoid oscillating densities by mixing the new density with previous densities via the direct inversion in the iterative subspace (DIIS) method [27]) or some other form of mixing. [19] Often the SCF loop is stopped when the change in density or the change in each eigenvalue becomes smaller than a prescribed value but this does not guarantee global conver-

gence. A more detailed analysis of numerical convergence in DFT calculations can be found in Ref. 5.

2.3 Inverse-Problem Methods

As is the case with the direct problem, there exist an assortment of numerical methods for solving the inverse problem of DFT each with its own set of advantages and disadvantages. Here we review several density-to-potential algorithms, introduce two new inversion methods, and benchmark the different schemes using a variety of target densities. All of the methods are presented using the finite-difference method and may include small adaptations made to convert algorithms that were originally designed for basis-set methods. We conclude this section with a set of benchmark density-to-potential inversions.

2.3.1 One-Orbital Formula

The one-orbital inversion formula

$$v_{\mathrm{KS}}([n]\,,\mathbf{r}) = \frac{\Delta\phi_0(\mathbf{r})}{2\phi_0(\mathbf{r})} = \frac{\Delta\sqrt{n_0(\mathbf{r})}}{2\sqrt{n_0(\mathbf{r})}} \tag{2.7}$$

can be derived simply by setting the energy to zero and solving for the KS potential in Eq. (2.1) in terms of the ground state density n_0. (We are allowed to set the energy to zero because the potential is only unique up to a constant as explained in Sec. 2.1.) This formula is exact for one electron or two electrons with opposite spins and is often referred to as the bosonic or one-electron potential. [28] Although at first glance the one-orbital formula appears somewhat trivial, it is helpful in unraveling many of the numerical problems common to all density-to-potential algorithms and can even serve as a useful approximation for systems with many electrons.

Although the one-orbital formula is exact for one-electron and most closed-shell two-electron systems, it must be carefully implemented numerically to avoid spurious

results. As seen in Sec. A.1, noisy densities can easily produce wildly inaccurate potentials when using Eq. (2.7) and finite difference operators. Such noisy behavior is unphysical because densities arising from the Schrödinger equation are theoretically continuous even when generated by singular potentials. [4] The following examples show how to appropriately smooth target densities based on the noise level before inserting them into the one-orbital formula.

We first illustrate smoothing using the particle-in-a-box ground state density as shown in Sec. C.1. If we take the exact ground-state density n_0^{exact} and add a small amount of weighted noise generated from the standard normal distribution $\mathrm{N}(\mu, \sigma^2)$ [29] according to the formula

$$n_0^{\text{noise}} = n_0^{\text{exact}} \left[1 + \mathrm{N}\big(0, 1 \times 10^{-10}\big)\right], \tag{2.8}$$

then the potential resulting from the one-orbital formula will also be noisy with a level proportional to the number of grid points. This noise can be removed by fitting a cubic spline to the target density weighted by the inverse of the approximate standard deviation $w = 1/(\sigma * n_0^{\text{approx}})$. We implement this smoothing procedure using the `UnivariateSpline` routine in the SciPy library and the results are shown in Fig. 2.3 for a box of length 5 with varying numbers of grid points. This example shows that smoothing is essential for dense grids with errors but not as important on coarse grids since the derivative of the error doesn't dominate in the one-orbital formula as explained in Sec. A.1.

The target density in the previous example was well approximated by a cubic spline but other target densities may need additional modifications before smoothing is applied. In particular, exponentially decaying densities are not adequately described by cubic splines unless they are first logarithmically transformed. We show how this can be done using the ground-state of the harmonic oscillator with the same weighted noise given by Eq. (2.8). In this case we take the logarithm of the noisy density, fit this new quantity to a cubic spline using the weights $w = 1/\log(1 + \sigma)$,

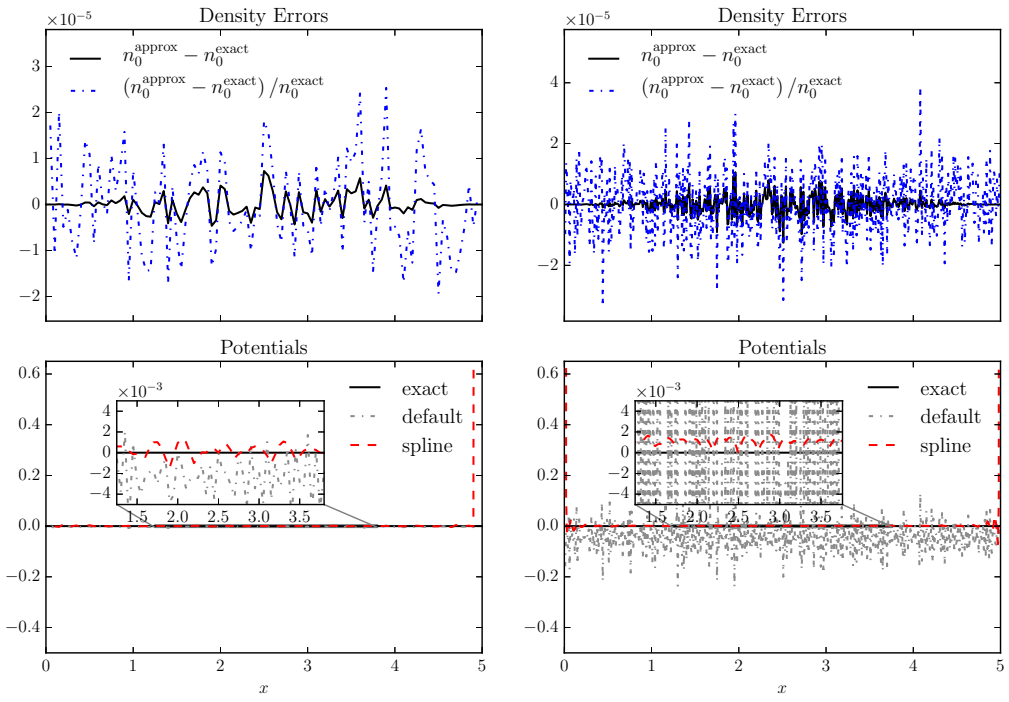

Figure 2.3. The ground-state density of a particle-in-a-box is contaminated with weighted randomly-distributed noise (top) and then inserted into the one-orbital formula before smoothing (default) and after smoothing (spline) via a weighted cubic spline (bottom). The smoothing has increasing importance as the number of grid points is increased from 101 (left) to 501 (right) even thought the target density's error level is the same.

and then exponentiate the result to get the smoothed target density. The potential produced using this logarithmic scaling before fitting is much more accurate in the asympototic region than the potential produced with no scaling before smoothing as seen in Fig. 2.4. We refer to this smoothing procedure later in this work as the logarithmic smoothing method. Figure 2.4 also shows that even highly singular potentials can be recovered using this method provided that the locations of zero density are first averaged with their nearest neighbors before applying the scaling and smoothing. As the grid is refined, the singular nature of the potentials becomes more pronounced with this procedure.

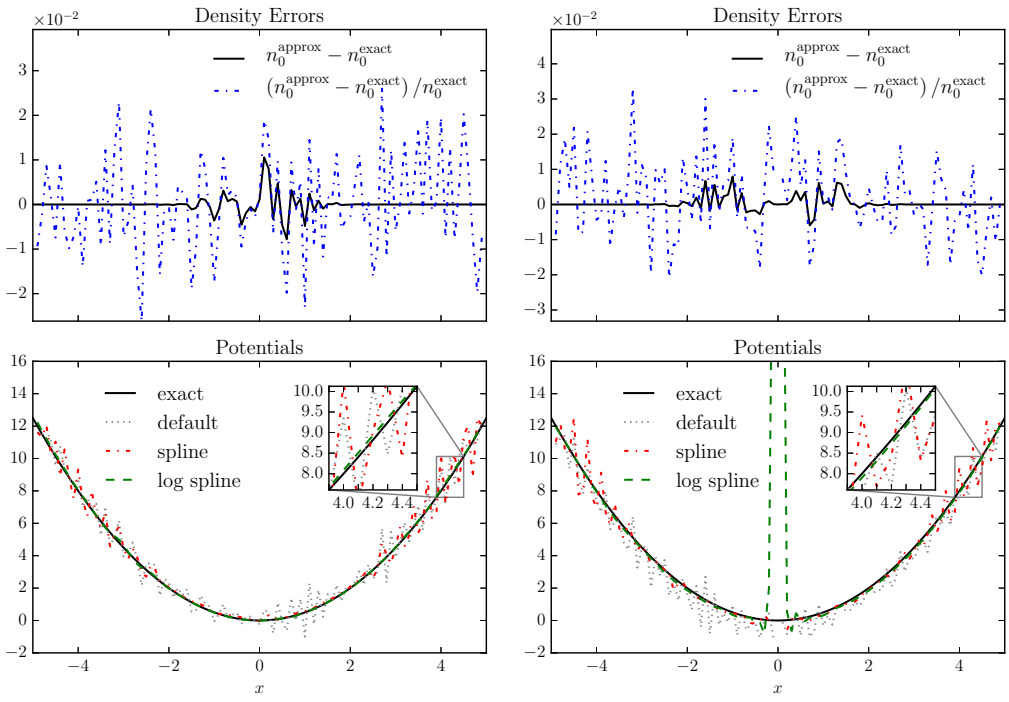

Figure 2.4. The ground-state density of the harmonic oscillator is contaminated with weighted randomly-distributed noise (top left) and then inserted into the one-orbital formula without smoothing (default), with smoothing (spline), and with a logarithmic transform before smoothing (log spline) via a weighted cubic spline (bottom left). The process is repeated on the right for the density of the first excited state and the distinct delta-well singularity [30] in the potential at $x = 0$ is recovered.

In the previous examples we were able to correctly smooth the target densities by having estimates of the standard deviation at each grid point. Such information would be typical of an experimentally determined density but most of the error patterns encountered in our density-to-potential inversions come from computationally determined densities using interacting wave function methods. In these cases we can use error estimates to compute the correct weights for the smoothing procedure. We show how this can be done by computing the ground state density of the harmonic oscillator using the infinite-to-finite spatial grid mapping of Ref. 31 with a scaling

parameter of $\alpha = 2$. (We purposely use a different grid to compute the target density in order to avoid comitting an inverse crime.) We compute the target density on this grid once with a second-order discretization of the Laplacian and 101 points, (labeled $n^{\mathcal{O}(2)}$), and then again with a fourth-order approximate Laplacian and 201 points, (labeled $n^{\mathcal{O}(4)}$). These two densities are linearly interpolated to the same equally-spaced grid shown in Fig. 2.4 and subtracted from each other to form an error estimate at each grid point. We then apply the logarithmically scaled spline fitting procedure described above with the approximate weights $w = 1/\left|\log n^{\mathcal{O}(2)} - \log n^{\mathcal{O}(4)}\right|$ and the exact weights $w = 1/\left|\log n^{\mathcal{O}(2)} - \log n^{\text{exact}}\right|$. The results of this calculation are displayed in Fig. 2.5 and show that the error pattern of the approximate target density is far more systematic than the random noise error patterns in the previous examples. The smoothing using approximate weights underestimates the potential at the edges of the box because the error estimate is too small in that region. If the error estimate is computed using 501 points instead of 201 points in the fourth-order density computation then the potential is recovered correctly in the entire box. This example illustrates the need not only for error estimates but also for the need to put bounds on the error estimates either through computing additional error estimates or through statistical means.

Even if the target density is correctly smoothed before applying the one-orbital formula, the finite difference operator used to approximate the Laplacian can severely limit the accuracy of a density-to-potential inversion. As was the case with the spline fitting procedure described above for exponentially decaying densities, the finite difference method performs poorly in the asymptotic region unless extra precautions are taken. In Sec. 2.3.3 we show how the finite difference operators can be modified to treat much of the exponential decay analytically through a scaling procedure. Figure 2.6 shows a comparison of the one-orbital formula applied to the exact ground state of the harmonic oscillator with and without scaling the finite difference operator.

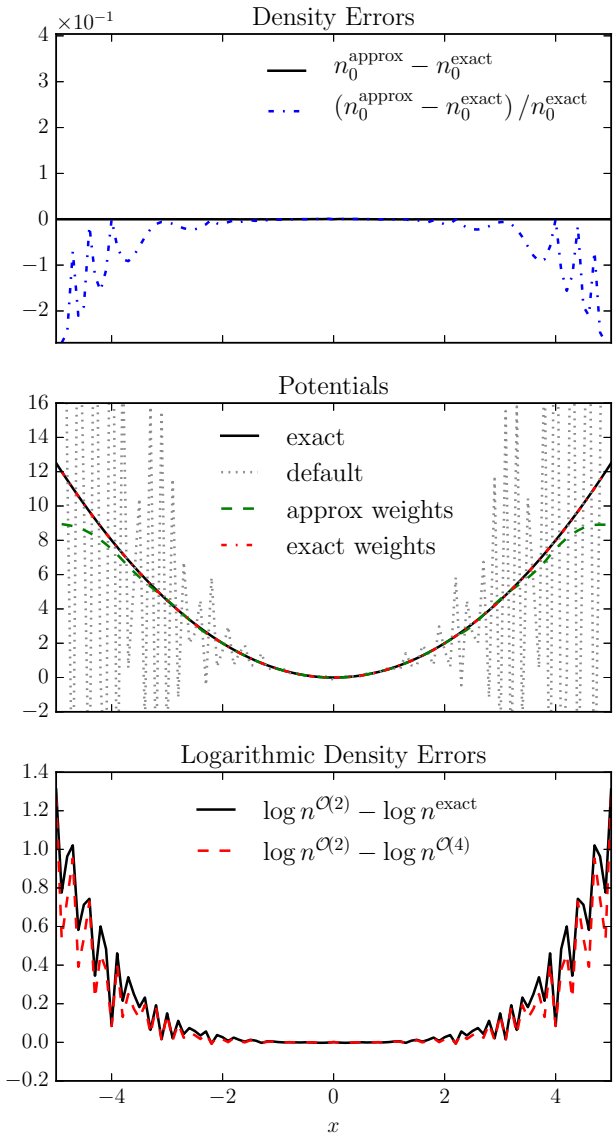

Figure 2.5. The ground-state density of the harmonic oscillator is computed using an infinite-to-finite spatial grid mapping (top) and then inserted into the one-orbital formula with both approximate and exact scaling weights (middle). The approximate weights are computed using an error estimate that tends to underestimate the error in the asymptotic region (bottom) and leads to an underestimated potential in that region.

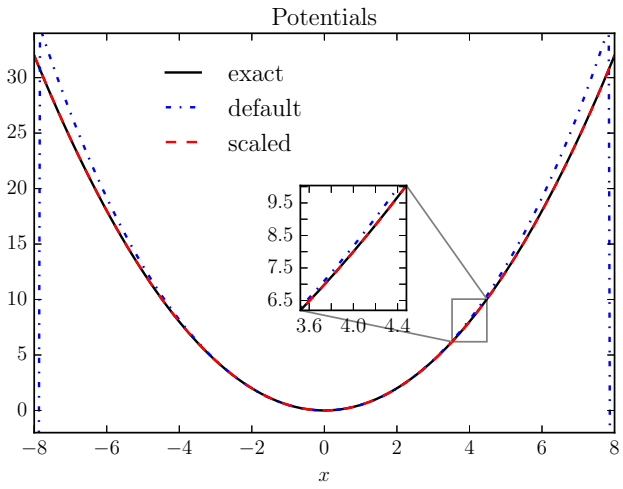

Figure 2.6. The ground-state density of the harmonic oscillator is inserted into the one-orbital formula without scaling (default) and with density scaling (scaled). The scaled finite difference operator performs much better in the asymptotic region $|x| > 4$ and doesn't have problems near the edges of the box.

Although the one-orbital formula is only exact for one- or two-electron systems, it is a remarkably good approximation for systems with large regions where the target density is dominated by one orbital. We illustrate the power of this approximation by applying it to a target density formed from the sum of the ground state and first two excited states of the harmonic oscillator. The harmonic potential is correctly recovered in the asymptotic region where most of the density comes from the second excited state as seen in Fig 2.7. The potential in the central region is not correct but it is a smooth approximation and is the same order of magnitude as the correct potential. Furthermore, the cost of the this approximation is simply one sparse matrix-vector multiplication followed by an array division, which is negligible in comparison to the many sparse matrix-vector multiplications typically needed to solve the eigenvalue problem in Eq. (2.3a).

The examples in this section demonstrate how the convergence criteria for DFT inverse problems are different from those of the direct problem. These examples and

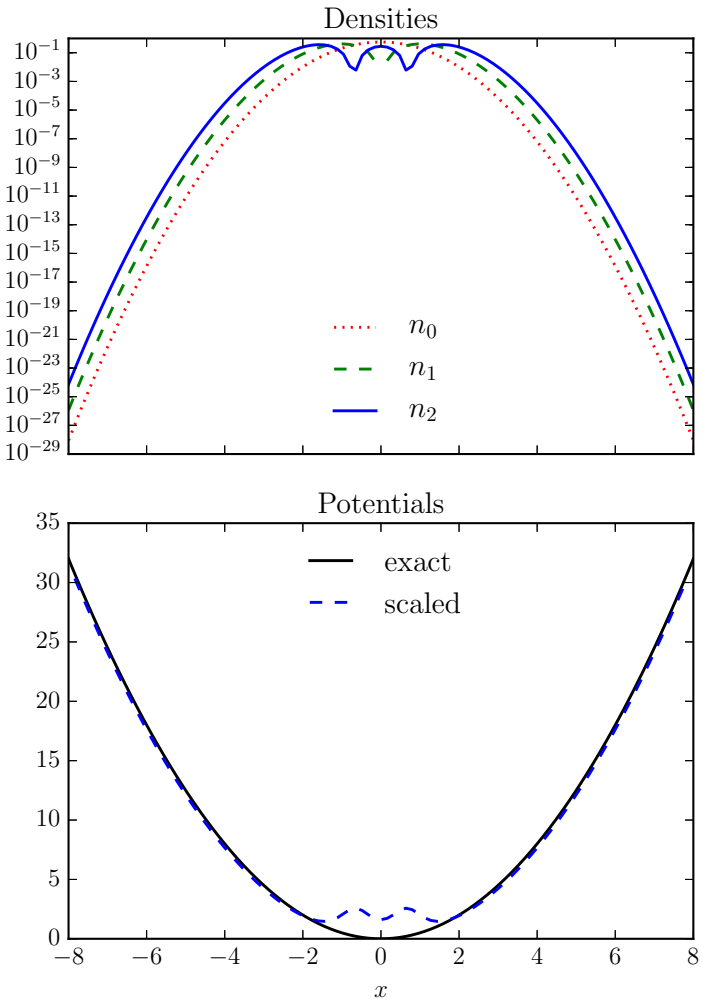

Figure 2.7. The densities of the ground-state and first two excited states of the harmonic oscillator (top) are summed and inserted into the one-orbital formula with density scaling (scaled). The resulting potential is an excellent approximation in the region $|x| > 2$ where the second excited state density is the dominant contribution to the total density.

Sec. A.1 clearly show that the size and location of the relative error in the target density is the main constraint on the accuracy of the potential resulting from a density-to-potential inversion. In many cases the target density must first be smoothed before performing an inversion and its standard deviation is the key ingredient in performing

this smoothing operation correctly. The accuracy of the finite difference operators also puts a strict limit on the quality of the recovered potential as some operators simply aren't good approximations in certain regions of rapidly changing density. Finally, the computational cost of the inverse problem using the one-orbital formula is much cheaper in these examples than the forward problem and can serve as a useful approximation for many-electron systems.

2.3.2 Previous Methods

A number of density-to-potential inversion methods have been developed besides the one-orbital inversion formula described in Sec. 2.3.1. In this section we look at the iterative inversion method of Ref. 32 and the direct optimization method of Ref. 17. A more complete review of the available density-to-potential inversion methods is found in Ref. 17. The two inversion schemes described in this section are fairly representative of the available methods and serve as useful benchmarks later in this chapter. The target density in the remainder of this chapter is written as $\tilde{n}$ for consistency with later chapters and to distiguish it from the intermediate densities created in the iterative procedures that we describe here. We also drop the KS subscript on the KS potential $v_{\mathrm{KS}}(\mathbf{r})$ to simplify the presentation.

The iterative inversion method of van Leeuwen and Baerends described in Ref. 32 is derived by multiplying both sides of Eq. (2.3a) by ϕ_j^*, summing over j, and then dividing by the density given in Eq. (2.3b) to produce the formula

$$v_{\mathrm{KS}}(\mathbf{r}) = \frac{2}{n(\mathbf{r})} \sum_{j=1}^{N} \phi_j^*(\mathbf{r}) \frac{\Delta}{2} \phi_j(\mathbf{r}) + \varepsilon_j \left|\phi_j(\mathbf{r})\right|^2 . \tag{2.9}$$

This formula is then turned into an iterative scheme by placing the target density in the denominator and iterating until convergence via the formula

$$\begin{aligned} v_{\mathrm{KS}}^{k+1}(\mathbf{r}) &= \frac{2}{\tilde{n}(\mathbf{r})} \sum_{j}^{N} \frac{1}{2} \phi_j^{k*}(\mathbf{r}) \, \boldsymbol{\nabla}^2 \phi_j^k(\boldsymbol{r}) + \epsilon_j^k \left| \phi_j^k(\mathbf{r}) \right|^2 \\ &= \frac{1}{\tilde{n}(\mathbf{r})} \left[n^k(\mathbf{r}) \, v^k(\mathbf{r}) \right] = \frac{n^k(\mathbf{r})}{\tilde{n}(\mathbf{r})} v^k(\mathbf{r}) \,, \end{aligned} \tag{2.10}$$

where k is the iteration index. This iterative scheme simply increases $v_{\mathrm{KS}}^{k+1}(\mathbf{r})$ in regions where $n^k(\mathbf{r}) > \tilde{n}(\mathbf{r})$ and decreases it in regions where $n^k(\mathbf{r}) < \tilde{n}(\mathbf{r})$ as seen in the last line of Eq. (2.10). The iterations are stopped when

$$\max_{\mathbf{r}} \left| 1 - \frac{n^k(\mathbf{r})}{\tilde{n}(\mathbf{r})} \right| < \epsilon \tag{2.11}$$

for some desired threshold ε. This scheme is sensitive to the initial potential guess $v_{\mathrm{KS}}^0(\mathbf{r})$ and usually requires a prefactor to avoid wild potential oscillations. Reference 32 suggests choosing this prefactor by enforcing the condition

$$1 - \delta < \gamma \frac{n^0(\mathbf{r})}{\tilde{n}(\mathbf{r})} < 1 + \delta, \tag{2.12}$$

where $\delta \approx 0.05$ and γ is the prefactor.

This iterative inversion scheme of van Leeuwen and Baerends is very easy to implement as it only requires a partial differential equation (PDE) solver to produce the new density $n^k(\mathbf{r})$ at each iteration. We do, however, make some modifications to the original scheme by not enforcing boundary conditions on the potential and by using the formula

$$v_{\mathrm{KS}}^{k+1}(\mathbf{r}) = v^k(\mathbf{r}) + \gamma \frac{n^k(\mathbf{r}) - \tilde{n}(\mathbf{r})}{\tilde{n}(\mathbf{r})} \tag{2.13}$$

instead of Eq. (2.10). We don't enforce boundary conditions on the potential because many of the test cases we use recover the external potential with unknown boundary conditions as opposed to just the exchange-correlation potential with its known asymptotic behavior. [32] We use Eq. (2.13) instead of Eq. (2.10) because it

still uses the same principle of increasing (decreasing) the potential in regions where the density is too large (small) but does not need boundary conditions to function properly. (Other modifications are also possible such as the use of an approximate density-density response matrix to help guide the iterations.) [33] This method produces smooth potentials by construction provided that the underlying eigenvalue solver produces smooth orbitals. The reliance on a prefactor, however, requires some manual intervention or sophisticated selection rules to ensure convergence. Large prefactors may result in wildly oscillating potentials that never converge while small prefactors may produce very small potential changes that take an inordinate amount of time to converge. Choosing a prefactor is usually not a problem for isolated inversions but can become very tedious when repeatedly applying the procedure to cases with many similar inversions such as in the creation of dissociation curves. [34]

The Wu-Yang inversion algorithm first introduced in Ref. 17 is one of the more sophisticated and versatile DFT inversion methods. In this inversion algorithm the Levy constrained-search formulation of DFT is modified to produce a direct optimization method for the KS kinetic energy density functional. The functional

$$W_s[v(\mathbf{r})] = \sum_{j=1}^{N} \left\langle \phi_j \left| \hat{T} \right| \phi_j \right\rangle + \int \mathrm{d}\mathbf{r}\, v(\mathbf{r}) \left[n(\mathbf{r}) - \tilde{n}(\mathbf{r}) \right] \tag{2.14}$$

is maximized to produce the optimal potential corresponding to the target density $\tilde{n}(\mathbf{r})$. This maximization is usually performed using classical optimization routines and is very efficient because the required first derivatives (Jacobian values) are given by the simple formula

$$\frac{\delta W_s[v(\mathbf{r})]}{\delta v(\mathbf{r})} = n(\mathbf{r}) - \tilde{n}(\mathbf{r})\,. \tag{2.15}$$

There is very little extra computational effort required to compute these derivatives because the density is already computed at each iteration while computing Eq. (2.14). The second derivatives (Hessian values) can also be computed either through first-order perturbation theory [17] or via the discrete adjoint-method described in Sec. 2.3.3.

The Wu-Yang inversion algorithm was developed originally for the optimized effective potential (OEP) method of DFT and later modified for the DFT inverse problem. [17, 35] The method is efficient and robust when implemented properly but can suffer from rounding errors as shown at the end of Sec. A.1. It can also produce unphysical highly oscillatory potentials when an unbalanced basis set is used without regularization. [36]

2.3.3 PDE-Constrained Optimization

The inversion schemes described in Sec. 2.3.2 rely on modifications to the KS equations or underlying energy functionals. Such modifications are not essential in creating DFT inversion methods as we show in this section through the use of PDE-constrained optimization. Although conceptually simpler than many other inversion procedures, PDE-constrained optimization can be difficult to implement due to the large number of unknowns and and programming challenges involved in the optimization procedure. In this section we give a brief introduction to PDE-constrained optimization in the context of DFT inverse problems and address many of these challenges. We also introduce an important scaling concept that plays a critical role in increasing the accuracy of the potential in the asymptotic regions of DFT inverse problems.

PDE-constrained optimization applied to the DFT inverse problem amounts to a fitting procedure in which the unknown potential is optimized until the corresponding density matches the target density. We use the weighted least-squares cost functional

$$F[v] = \frac{1}{2} \left\| \sqrt{w(\mathbf{r})} \left[n([v], \mathbf{r}) - \tilde{n}(\mathbf{r}) \right] \right\|_2^2 \tag{2.16}$$

as our measure of fitness, where the subscript 2 indicates the L^2 norm and $w(\mathbf{r})$ is a positive definite weighting function. The density $n([v], \mathbf{r})$ comes from solving Eqs. (2.3a) and (2.3b) for a given potential chosen during the optimization procedure. The numerical minimization of the discretized Eq. (2.16) usually involves a

very large number of unknown potential values and generally requires the use of gradient/Jacobian-based optimization algorithms. [37] The derivation, programming, and computation of these gradients, [functional derivatives of the cost functional given by Eq. (2.16)], is the main difficulty in applying PDE-constrained optimization to the DFT inverse problem.

We use the discrete adjoint-method to compute the cost functional derivatives of Eq. (2.16). This method is also called the discretize-then-differentiate method because the cost functional is first discretized and then differentiated with respect to the potential. [38] Section B.1 contains a complete derivation of the discrete adjoint equations for the DFT inverse problem in multiple dimensions. These derivatives are then employed in the truncated-Newton (TN) algorithm of Ref. 39 as implemented in the SciPy library [26] to optimize the unknown potential until a desired density fit is found. The computational cost of computing the cost functional derivatives via the discrete adjoint-method is roughly the same as computing the cost functional depending on the choice of linear solver.

The PDE-constrained inversion method outlined above can also suffer from rounding errors similar to the Wu-Yang algorithm described in Sec. 2.3.2. These errors can be avoided simply by weighting the densities in the asymptotic region more heavily than the high-density regions. One possibility is to set $w(\mathbf{r}) = 1/\left[\tilde{n}(\mathbf{r})\right]^2$ so that the relative error is minimized instead of the absolute error. This weighting scheme in combination with the rescaling described below allows us to accurately reproduce the unknown potential in all regions of a given density-to-potential problem.

As mentioned in Sec. 2.3.1, the finite difference operators used to approximate the Laplacian are not very accurate in regions where the exponential decay dominates the behavior of the KS orbitals. The finite difference operators would be accurate in all regions if we could apply them to the logarithm of the orbitals similar to the logarithmic spline fitting procedure described in Sec. 2.3.1. The KS orbitals, however,

are not positive semidefinite like the particle density so we instead write them as $\phi_j(\mathbf{r}) = \sqrt{\tilde{n}(\mathbf{r})}\chi_j(\mathbf{r})$ and solve for the scaled orbitals $\{\chi_j(\mathbf{r})\}$ in the KS equations

$$\varepsilon_j \sqrt{n(\mathbf{r})}\chi_j(\mathbf{r}) = \left[-\frac{\Delta}{2} + v(\mathbf{r})\right] \sqrt{n(\mathbf{r})}\chi_j(\mathbf{r}) \text{ and} \tag{2.17a}$$

$$n(\mathbf{r}) = 2\sum_{j=1}^{N} \left|\sqrt{n(\mathbf{r})}\chi_j(\mathbf{r})\right|^2 . \tag{2.17b}$$

After distributing the Laplacian and canceling common factors, Eq. (2.17a) can be rewritten as

$$\varepsilon_j \chi_j(\mathbf{r}) = -\frac{1}{2}\left[\frac{\Delta\sqrt{n(\mathbf{r})}}{\sqrt{n(\mathbf{r})}}\chi_j(\mathbf{r}) + 2\frac{\boldsymbol{\nabla}\sqrt{n(\mathbf{r})}}{\sqrt{n(\mathbf{r})}} \cdot \boldsymbol{\nabla}\chi_j(\mathbf{r}) + \Delta\chi_j(\mathbf{r})\right] + v(\mathbf{r})\,\chi_j(\mathbf{r})\,. \tag{2.18}$$

The scaling factor can also be written as

$$\sqrt{\tilde{n}(\mathbf{r})} = \exp\left\{\frac{1}{2}\log\tilde{n}(\mathbf{r})\right\} \tag{2.19}$$

and differentiated to produce the terms

$$\frac{\boldsymbol{\nabla}\sqrt{\tilde{n}(\mathbf{r})}}{\sqrt{\tilde{n}(\mathbf{r})}} = \frac{1}{2}\boldsymbol{\nabla}\log\tilde{n}(\mathbf{r}) \text{ and} \tag{2.20}$$

$$\frac{\Delta\sqrt{\tilde{n}(\mathbf{r})}}{\sqrt{\tilde{n}(\mathbf{r})}} = \frac{1}{2}\left[\frac{1}{2}\left|\boldsymbol{\nabla}\log\tilde{n}(\mathbf{r})\right|^2 + \Delta\log\tilde{n}(\mathbf{r})\right]. \tag{2.21}$$

The derivatives of $\log\tilde{n}(\mathbf{r})$ and $\{\chi_j(\mathbf{r})\}$ are well approximated by the finite difference operators described in Sec. 2.2 because they do not decay exponentially. An example of the scaled orbitals for a system consisting of the first three orbitals of the harmonic oscillator can be seen in Fig. 2.8.

Although it is common to enforce boundary conditions on the orbitals when solving the KS equations, we simply let the numerical optimization routine choose the ideal boundary conditions by modifying the potential at the edges of the simulation box.

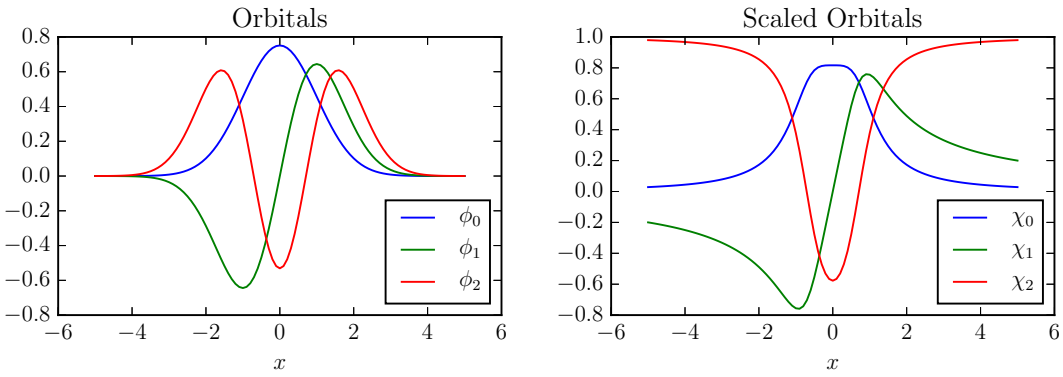

Figure 2.8. The first three orbitals of the one-dimensional simple harmonic oscillator without scaling (top) and with scaling by the square root of the molecular density (bottom).

Section A.1 shows how difficult it can be to match the true boundary conditions of the orbitals and also the negative impact approximate boundary conditions can have on the potential near the boundaries. This negative impact is also illustrated in Fig. 2.9 in which the PDE-constrained optimization procedure outlined above is applied to a target density formed from the sum of the ground state and first two excited states of the harmonic oscillator. This example clearly shows that enforcing approximate zero derivative boundary conditions on the scaled orbitals results in the incorrect potential at the boundary whereas the potential is recovered correctly when no boundary conditions are applied. If the target density happens to be produced using artificial boundary conditions then the potential recovered when not applying boundary conditions on the orbitals may have several incorrect values at the edge of the simulation box as shown in some of the examples of Sec. 2.4.

2.3.4 Constrained Variational Method

The previous inversion methods described in this chapter all require the solution of an eigenvalue problem at each iteration. In the case of small systems this is not a se-

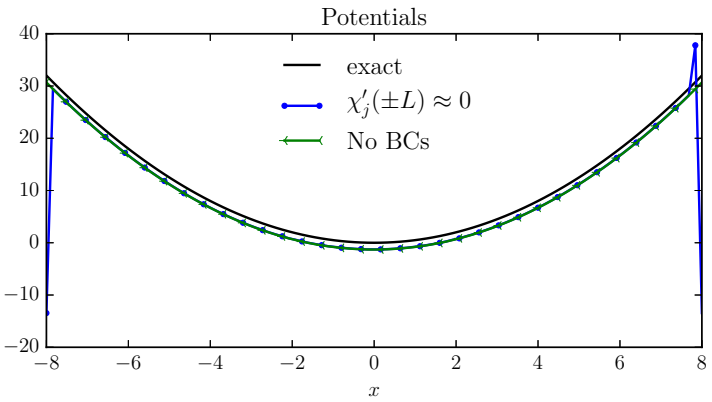

Figure 2.9. The potentials produced in a density-to-potential inversion using the inversion method of Sec. 2.3.3 and a target density formed from the sum of the ground state and first two excited states of the harmonic oscillator. The potential is correct at the boundaries when no boundary conditions are applied to the scaled orbitals (No BCs) and incorrect when the first derivative of the scaled orbitals is set to zero at the boundaries ($\chi_j'(\pm L) \approx 0$).

vere constraint but as the system size increases the solution of the eigenvalue problem begins to dominate the computation. [5] Although dismissed in Ref. [17] as "difficult to perform", the Levy constrained-search formulation can be used directly to perform a density-to-potential inversion without repeatedly solving eigenvalue problems at each iteration. In this section we show how to overcome many of the difficulties involved in this constrained-search inversion method through the use of scaling and regularization.

In the Levy constrained-search formulation of DFT, the noninteracting kinetic energy is minimized subject to the constraints that the orbitals are orthonormal and

produce the molecular density of the real system. The functional to be minimized in this search can be written using Lagrange multipliers as

$$J\left(\{\phi_j\}\right) = \sum_{j=1}^{N_{\text{orbs}}} \int \mathrm{d}\mathbf{r} \left\{ \left|\boldsymbol{\nabla}\phi_j\right|^2 + v_{\text{KS}}(\mathbf{r}) \left[\phi_j^2(\mathbf{r}) - \tilde{n}(\mathbf{r})\right] + \sum_{k=j}^{N_{\text{orbs}}} \varepsilon_{j,k} \left(\phi_j(\mathbf{r})\, \phi_k(\mathbf{r}) - \delta_{j,k}\right) \right\}, \quad (2.22)$$

where the orbitals are assumed to be real for simplicity of presentation. This expression can be used directly in a constrained numerical optimization program to find the orbitals and KS potential for a given target density without the need to solve an eigenvalue problem at each iteration. It does, however, suffer from the same rounding errors involved in the Wu-Yang algorithm as it still involves a minimization of the noninteracting kinetic energy. Furthermore, the orthonormality and density constraints can easily lead to unphysical orbitals as they compete with one another in the optimization.

In order to resolve the issues mentioned above, we use the scaled orbitals introduced in Sec. 2.3.3 and regularize them via the expression

$$\alpha \sum_{j=1}^{N_{\text{orbs}}} \int \mathrm{d}\mathbf{r} \left|\boldsymbol{\nabla}\chi_j(\mathbf{r})\right|^2, \quad (2.23)$$

where $\alpha > 0$ is the regularization parameter chosen via the discrepancy principle. [14] The density constraint with the scaled orbitals is

$$\sum_{j=1}^{N_{\text{orbs}}} \int \mathrm{d}\mathbf{r} \left[\chi_j^2(\mathbf{r}) - 1\right]. \quad (2.24)$$

$$0 = 2\phi^\alpha v + \left(\sum_{m=1}^{\alpha} \varepsilon^{m,\alpha} \phi^m + \sum_{n=\alpha}^{N_{\text{orbs}}} \varepsilon^{\alpha,n} \phi^n \right) - \Delta\phi^\alpha, \quad (2.25)$$

No boundary conditions are applied to the orbitals for reasons explained in Sec. 2.3.3.

Optimizing the noninteracting kinetic energy using the scaled and regularized orbitals produces a set of orthonormal orbitals that are a unitary transformation of the KS orbitals. [40] We use the IPOPT library [41] to perform this constrained minimization. The KS potential can be extracted from these orbitals by solving the set of linear equations

$$\left\{ \int \mathrm{d}\mathbf{r}\, \phi_\beta(\mathbf{r})\, \Delta\phi_\alpha(\mathbf{r}) = 2 \int \mathrm{d}\mathbf{r}\, \phi_\beta(\mathbf{r})\, \phi_\alpha(\mathbf{r})\, v_{\mathrm{KS}}(\mathbf{r}) + \left(\sum_{m=1}^{\alpha} \varepsilon_{m,\alpha} \phi_m(\mathbf{r}) + \sum_{n=\alpha}^{N_{\mathrm{orbs}}} \varepsilon_{\alpha,n} \phi_n(\mathbf{r}) \right) \right\} \quad (2.26)$$

where $\alpha, \beta = 1, \ldots, N_{\mathrm{orbs}}$. This linear system can be solved efficiently using a sparse least-squares solver in which the full matrix is never explicitly created. An example of this density-to-potential inversion procedure with two different regularization parameters is shown in Fig. 2.10 for a target density formed from the sum of the ground state and first two excited state densities of the harmonic oscillator.

2.4 Inversion Examples

The inversion methods described in Sec. 2.3 each have strengths and weaknesses that are best illustrated by examples. We first present several DFT inversions for noninteracting systems in which the external potential is recovered and compared with the exact answer. We then present density-to-potential inversions for one-dimensional models of an atom and a molecule. Unless otherwise noted, the examples all use the one-orbital approximation as the initial guess for the unknown potential. Table 2.1 displays the abbreviations used in this section to distiguish the different inversion methods.

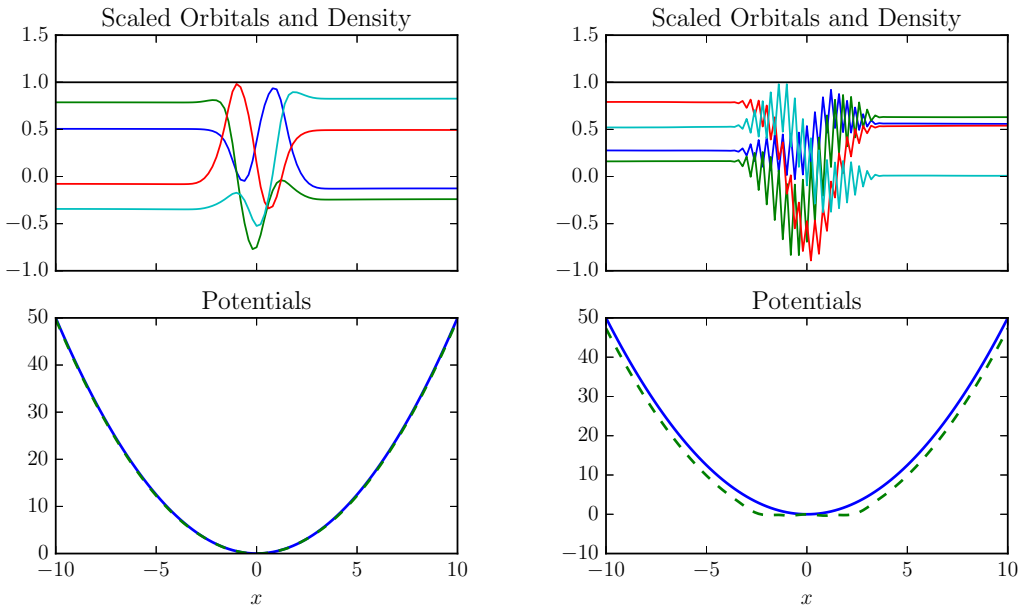

$\alpha = 10^{-1}$ $\alpha = 10^{-2}$

Figure 2.10. The scaled orbitals and density of a constrained variational density-to-potential inversion with two different regularization parameters (top). The orthonormalization constraint dominates in the under-regularized example (right) producing wild oscillations in the high-density region. The corresponding potentials (bottom) are found by solving Eq. 2.26.

Table 2.1.

The labels used to identify each DFT inversion method for the inversion examples of Sec. 2.4.

Inversion Method	Label	Description
PDE-constrained optimization	PDE	Sec. 2.3.3
van Leeuwen and Baerends	vLB	Sec. 2.3.2
Wu and Yang	WY	Sec. 2.3.2
Constrained Variational	CV	Sec. 2.3.4

2.4.1 Noninteracting Harmonic Potential Inversion

Our first inversion example is a noninteracting system of six electrons in the harmonic potential $v(x) = \frac{1}{2}x^2$. The target density is the sum of the ground state

and first two excited-state densities formed from Eqs. C.6-C.8 with each orbital doubly occupied as indicated in Eq. 2.1b. The potentials recovered from this density using the inversion methods of Sec. 2.3 are shown in Fig. 2.11. The potential is only unique up to a constant so we also plot the differences between the recovered and exact potentials with the more constant differences indicating better recovered potentials. The rounding errors in the WY algorithm's functional dominate in the region $|x| > 4$ as explained near the end of Sec. A.1. The unscaled finite-difference scheme used in the vLB method is not accurate in the region $|x| > 4$ and leads to an incorrect higher curvature in that region. Both the WY and vLB methods can likely be modified to include scaling to better match the CV and PDE methods.

2.4.2 One-Dimensional Beryllium

One-dimensional atomic and molecular models are often used in exploring DFT because many quantities can be found exactly or to very high accuracy with little computational effort. [33] In this section we look at a one-dimensional model of beryllium using the exponential interaction

$$v_{\text{exp}}(x) = A \exp\left(\kappa \left|x\right|\right), \tag{2.27}$$

where $A = 1.071295$ and $\kappa^{-1} = 2.385345$. This electronic interaction was first introduced in Ref. 24 as an alternative to the soft-Coulomb interaction. The tails of this interaction are weaker than the soft-Coulomb interaction to more closely match the shorter-ranged three-dimensional Coulomb interaction when screening is considered. Cusps are also present in this interaction in analogy with three-dimensional Coulombic systems as seen in this and the following LiH examples.

The target density of our one-dimensional beryllium atom is computed using the density matrix renormalization group (DMRG), where the exponential interaction is much faster to compute. [24] This density does contain some numerical error in the asymptotic regions so we smooth it using the logarithmic smoothing procedure

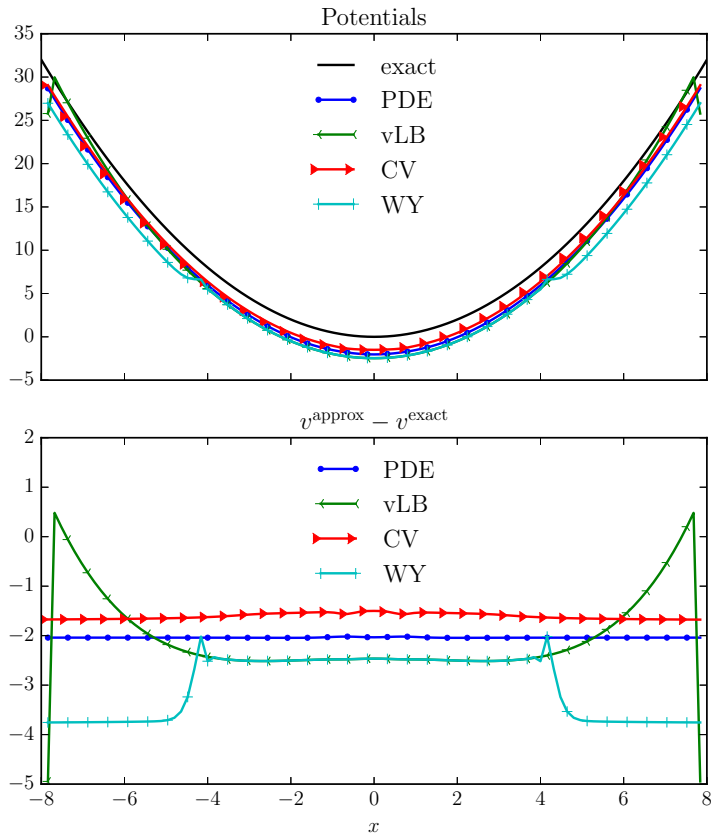

Figure 2.11. The potentials produced in a density-to-potential inversion using the inversion methods described in Sec. 2.3 and a target density formed from the sum of the ground state and first two excited states of the harmonic oscillator (top). The correct potential is only unique up to a constant so we also plot the difference $v^{\text{approx}} - v^{\text{exact}}$ (bottom) with the more constant lines being an indication of correctness.

described in Sec. 2.3.1 The external potential is $v_{\text{ext}}(x) = -4v_{\text{exp}}(x)$ and the Hartree potential is found using Eq. 2.6 with $v_{\text{ee}}(x) = v_{\text{exp}}(x)$. The KS potential is found using the method described in Sec. 2.3.3. The exchange-correlation potential is then found by subtracting the Hartree and external potentials from the KS potential. The results are shown in Fig. 2.4.2 and clearly show the cusp behavior resulting from the exponential interaction.

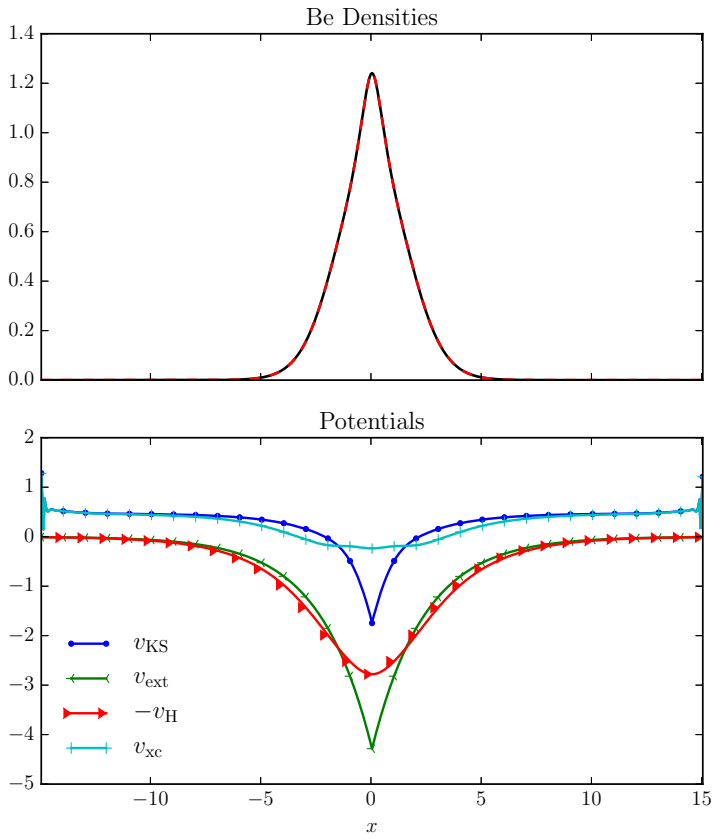

Figure 2.12. The density (top) for a one-dimensional model of beryllium using an exponential interaction as described in Sec. 2.4.2. The Hartree, external, KS and exchange-correlation potentials are also displayed (bottom).

2.4.3 One-Dimensional Lithium Hydride

In this section we consider a one-dimensional model of lithium hydride using the exponential interaction described in Sec. 2.4.2. The external potential is $v_{\mathrm{ext}}(x) = -v_{\mathrm{exp}}(x) - 3v_{\mathrm{exp}}(x)$ and the Hartree potential is again found using Eq. 2.6 with $v_{\mathrm{ee}}(x) = v_{\mathrm{exp}}(x)$. The target density is found using the DMRG and the KS potential is computed using the method described in Sec. 2.3.3. The densities and potentials are shown at four separation distances in Fig. 2.13. As the molecule dissociates, the

KS potential forms a characteristic step and peak in the internuclear region present in similar studies. [42] These features can be seen in more detail in Fig. 2.14.

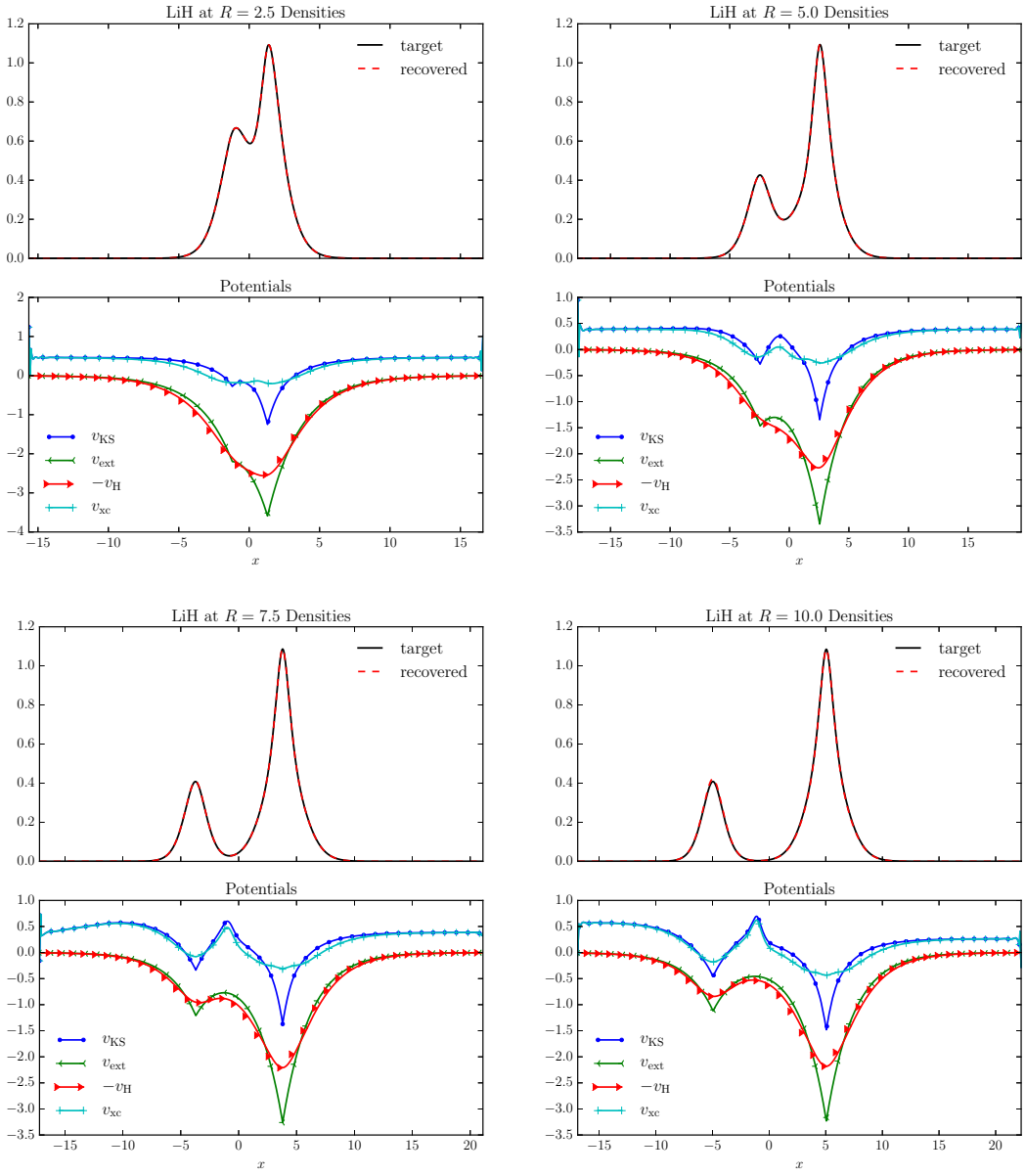

Figure 2.13. The density and corresponding potentials for a one-dimensional model of lithium hydride using an exponential interaction. The quantities are computed at various separation distances R to show the formation of a peak in the exchange-correlation potential in the internuclear region at large separations.

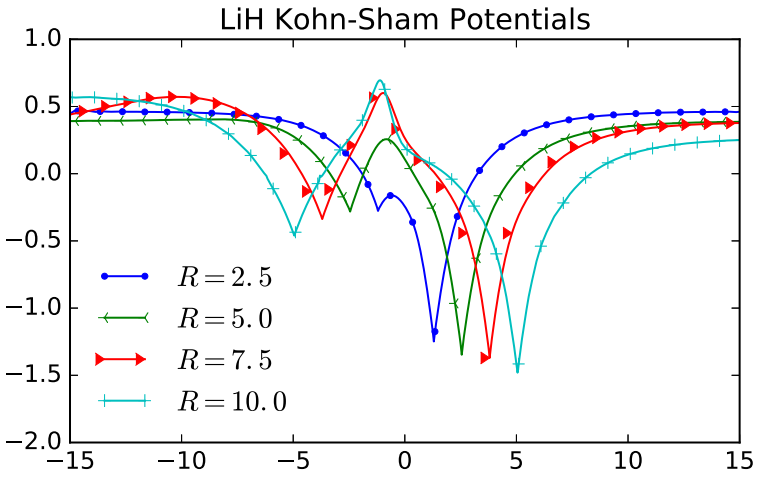

Figure 2.14. The Kohn-Sham potentials for a model one-dimensional lithium hydride system at four different internuclear separations.

3. Inversions in Partition Density Functional Theory

This chapter contains work from the article entitled 'Comment on "Application of partition density-functional theory to one-dimensional models"' written by Peter Elliott, Adam Wasserman, Kieron Burke, and the author. [43]

3.1 Partition Density Functional Theory

Partition theory is one of several methods for partitioning the electronic density of a system into a sum of fragment densities. [44] It was originally designed to resolve several issues in chemical reactivity theory [45] and has since been unified with density functional theory (DFT) to calculate molecular properties of systems via DFT calculations on isolated fragments. [43, 46] This fragment-based DFT is known as partition density functional theory (PDFT) and is analogous to DFT in that systems of interacting fragments are mapped onto systems of noninteracting fragments experiencing a common potential similar to how a system of interacting electrons is mapped onto a system of noninteracting electrons in DFT. The common potential that the noninteracting fragments feel is known as the partition potential and it is the functional derivative of the partition energy.

Partition density functional theory has several unique features that differentiate it from many other fragment-based density functional theories. [44] The partition potential in PDFT is the same for all fragments and the resulting fragment densities are *uniquely* determined by the fragmentation choice. [45] Noninteger numbers of electrons are allowed in the fragments through the use of the ensemble method of Ref. 47. These and other properties of PDFT are being used to develop new approximations that address the limitations of current approximations within DFT. In particular, progress is being made in resolving delocalization and static correlation errors that

plague standard DFT calculations through the development of simple partition energy functionals that use standard exchange-correlation functionals. [34]

In this chapter we review the basic theory of PDFT and introduce the reader to the inverse PDFT problem. The inversion method of Ref. 46 is used to find the partition potential and fragment occupations numbers for several one-dimensional model systems.

3.1.1 The Direct and Inverse Problems

In PDFT the external potential $v_{\text{ext}}(\mathbf{r})$ is split into a sum of fragment potentials $\{v_\alpha(\mathbf{r})\}$ such that

$$v_{\text{ext}}(\mathbf{r}) = \sum_\alpha v_\alpha(\mathbf{r})\,, \tag{3.1}$$

where the fragment potentials are arbitrary but usually chosen based on chemical intuition. [44] The energy of each fragment E_α and the total fragment energy E_f are defined as

$$E_\alpha[n_\alpha] = F[n_\alpha] + \int \mathrm{d}\mathbf{r}\, n_\alpha(\mathbf{r})\, v_\alpha(\mathbf{r}) \text{ and} \tag{3.2}$$

$$E_f[n_\alpha] = \sum_\alpha E_\alpha[n_\alpha]\,. \tag{3.3}$$

Partition theory requires E_f to be minimized subject to the constraint that the fragment densities add up to the correct molecular density

$$n(\mathbf{r}) = \sum_\alpha n_\alpha(\mathbf{r}) \tag{3.4}$$

and that the fragment occupations add up to the correct number of electrons

$$N = \sum_\alpha N_\alpha. \tag{3.5}$$

These constraints can be enforced using Lagrange multipliers and minimizing the grand potential [48]

$$\mathcal{G} = E_f + \int \mathrm{d}^3\mathbf{r}\, v_\mathrm{p}(\mathbf{r}) \left(\sum_\alpha n_\alpha(\mathbf{r}) - n(\mathbf{r}) \right) - \mu \left(\sum_\alpha N_\alpha - N \right). \tag{3.6}$$

The Lagrange multiplier μ is the chemical potential of the system and the Lagrange multiplier $v_\mathrm{p}(\mathbf{r})$ is the global partition potential. Each fragment is allowed to have noninteger occupations as described below.

Minimization of the grand potential in Eq. (3.6) is one way to solve the PDFT problem but it requires access to the density of the entire system at the outset. Although there are cases where the system density is already known in advance, it is usually found self consistently via a set of Kohn-Sham (KS)-like equations. In this chapter we use the procedure given in Ref. 46 with the equations

$$\epsilon_{j,\alpha}\phi_{j,\alpha}(\mathbf{r}) = -\frac{\Delta}{2}\phi_{j,\alpha}(\mathbf{r}) + v_{\mathrm{KS,f},\alpha}[n_\alpha, \overline{n}_\alpha](\mathbf{r})\, \phi_{j,\alpha}(\mathbf{r}), \tag{3.7a}$$

$$v_{\mathrm{KS,f},\alpha}[n_\alpha, \overline{n}_\alpha](\mathbf{r}) = v_\mathrm{KS}[n_\alpha](\mathbf{r}) + \{v_\mathrm{ext}(\mathbf{r}) + v_\mathrm{Hxc}[n](\mathbf{r}) - v_\mathrm{KS}[n](\mathbf{r})\}, \tag{3.7b}$$

$$= v_\alpha(\mathbf{r}) + v_\mathrm{p}(\mathbf{r}) + v_\mathrm{Hxc}[n_\alpha](\mathbf{r}), \text{ and} \tag{3.7c}$$

$$\overline{n}_\alpha(\mathbf{r}) = n(\mathbf{r}) - n_\alpha(\mathbf{r}). \tag{3.7d}$$

The subscript 'KS, f' indicates an effective KS-like potential for the fragment α and the 'Hxc' subscript refers to the Hartree-exchange-correlation potential $v_\mathrm{H}([n], \mathbf{r}) + v_\mathrm{xc}([n], \mathbf{r})$. The fragment densities are defined according to the Perdew, Parr, Levy, and Balduz (PPLB) ensemble formulation of DFT with

$$n_\alpha(\mathbf{r}) = (1 - \nu_\alpha)\, n_{p_\alpha}(\mathbf{r}) + \nu_\alpha n_{p_\alpha+1}(\mathbf{r}) \tag{3.8}$$

where $N_\alpha = p_\alpha + \nu_\alpha$, p_α a nonnegative integer, $0 \leq \nu_\alpha \leq 1$, and

$$F[n_\alpha] = (1 - \nu_\alpha)\, F[n_{p_\alpha}] + \nu_\alpha F[n_{p_\alpha+1}]. \tag{3.9}$$

The functional F is the so-called universal functional

$$F[n] = \min_{\Psi \to n(\mathbf{r})} \langle \Psi | \hat{T} + \hat{V}_{\text{ee}} | \Psi \rangle \,. \tag{3.10}$$

In the direct problem of PDFT an approximate partition potential and corresponding functional are usually used to compute the fragment densities and total molecular density. [49] This approximation is additional to any DFT approximations used in the fragment calculations for the exchange-correlation functional and corresponding potential. If the exact partition potential is known and the same exchange-correlation approximation is used consistently in a PDFT calculation then the resulting molecular density will be identical to a standard DFT calculation using the same exchange-correlation approximation. [50] There are, however, some advantages to using approximate partition energy functionals and Ref. 49 shows how they can be used to avoid errors in standard DFT calculations.

Several simple one-dimensional examples of PDFT are given in Figs. 3.1-3.4 to help illustrate how it works in practice. Figure 3.1 shows a molecular calculation of four noninteracting electrons in the external potential $v_{\text{ext}}(x) = \sum_{a=1}^{4} \tilde{v}_a(x)$, where

$$\tilde{v}_1(x) = \frac{-1.2}{\cosh^2\left(x+4\right)/1.5}, \; \tilde{v}_2(x) = \frac{-1.2}{\cosh^2\left(x+2\right)/1.5}, \; \tilde{v}_3(x) = \frac{-1}{\cosh^2\left(x-2\right)}, \\ \text{and } \tilde{v}_4(x) = \frac{-1}{\cosh^2\left(x-4\right)}. \tag{3.11}$$

Figures 3.2, 3.3, and 3.4 show how the external potential of the total system can be partitioned into two, three, and four separate fragments, respectively. The resulting fragment densities are very localized and the partition potential is attractive between all of the fragments. The partition potential, however, will not always be attractive as can be seen in places around the left fragments in Fig. 3.4 due to the large amount of density overlap in that region. The partition potential and occupation numbers are found numerically in all of these examples by way of a density-to-potential inversion using the procedures described in Sec. 3.2.

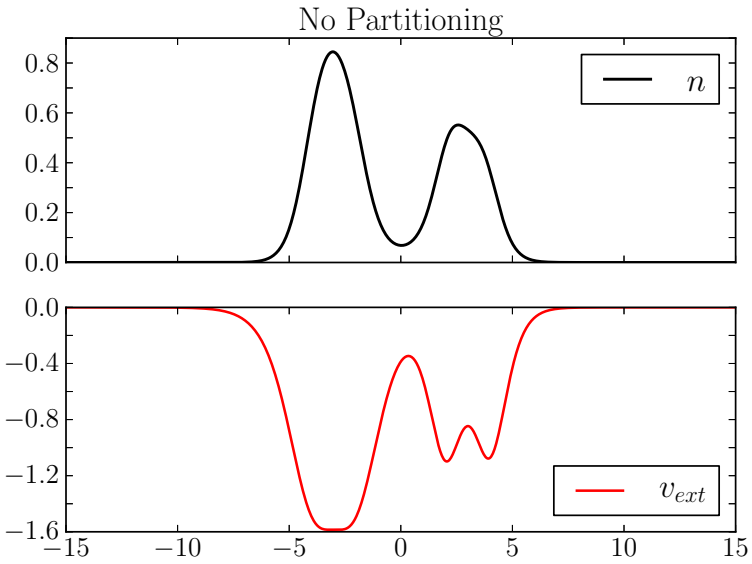

Figure 3.1. The molecular density (top) and external potential (bottom) for a system of four noninteracting electrons in one partition.

In the inverse problem of PDFT the partition potential and fragment occupations are recovered from a given target molecular density and choice of external potential partitioning. This is similar to the DFT inverse problem except for the fact that the exchange-correlation potential is also used in the PDFT problem and is an additional unknown for interacting systems. Thus the partition potential can be found within a given exchange-correlation approximation or using additional inversions to find the exact exchange-correlation potentials. In this chapter we only treat noninteracting systems in which the exchange-correlation potentials are zero for simplicity.

3.2 Inversion Algorithm

The partition potential $v_{\mathrm{p}}(\mathbf{r})$, chemical potential μ, and occupation numbers $\{N_\alpha\}$ are the central quantities in an inverse PDFT problem. Several methods exist to extract these quantities as explained in Ref. 49. As mentioned earlier, we use the

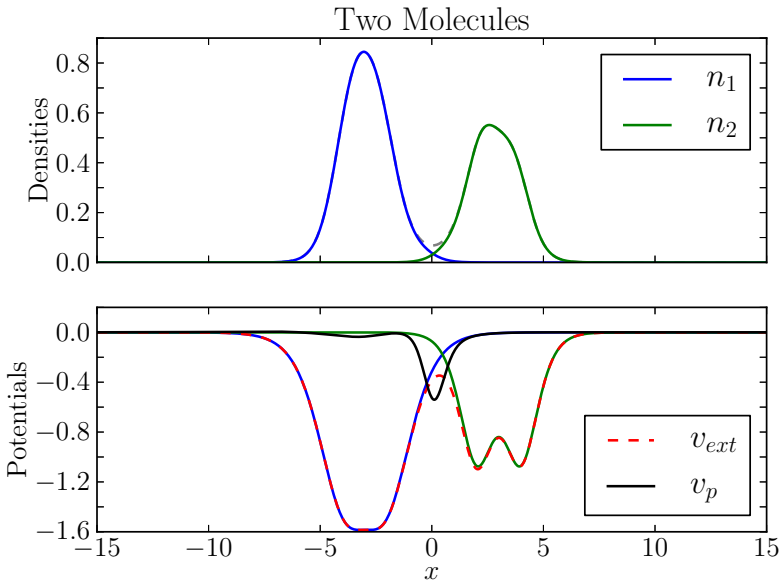

Figure 3.2. The fragment densities (top) and potentials (bottom) for a system of four noninteracting electrons with the molecules on the left and right in different partitions.

method of Ref. 46 to solve for these unknowns and illustrate the convergence of this procedure with an example.

The inversion procedure begins by solving the standard DFT problem for each isolated fragment to produce a set of densities $\left\{n_\alpha^{(0)}\right\}$ as an initial guess. We set the initial partition potential $v_{\mathrm{p}}^{(0)}(\mathbf{r})$ to zero as an initial guess. The partition potential and fragment occupations are then updated according to the formulas

$$v_{\mathrm{p}}^{(k+1)}(\mathbf{r}) = v_{\mathrm{p}}^{(k)}(\mathbf{r}) + \left(v_{\mathrm{ext}}(\mathbf{r}) - v_{\mathrm{ext}}\left[n^{(k)}\right](\mathbf{r})\right) \text{ and} \tag{3.12}$$

$$N_\alpha^{(k+1)} = N_\alpha^{(k)} - \Gamma\left(\mu_\alpha^{(k)} - \bar{\mu}^{(k)}\right), \tag{3.13}$$

where Γ is a positive constant, $\bar{\mu}$ is the average of the fragment chemical potentials, and $v_{\mathrm{ext}}\left[n^{(k)}\right](\mathbf{r})$ is the result of a DFT inversion for the molecular density at iteration k. The update procedure described in Eq. (3.12) ensures that the partition potential

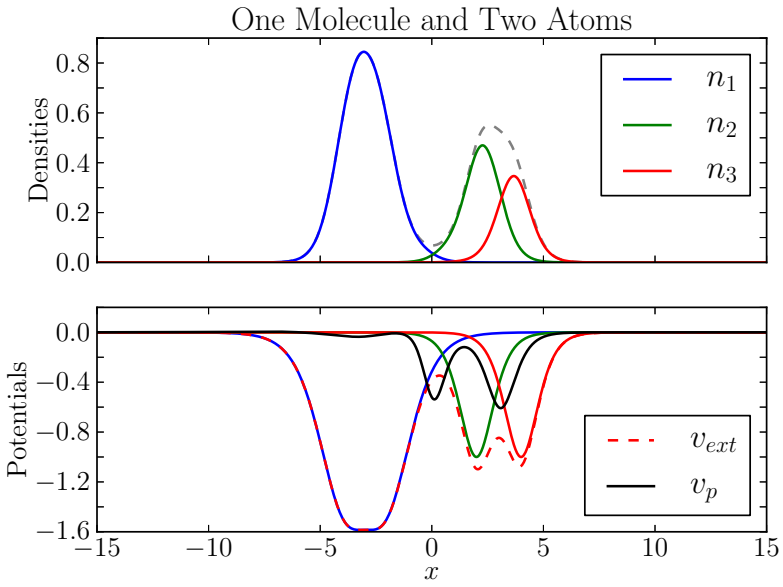

Figure 3.3. The fragment densities (top) and potentials (bottom) for a system of four noninteracting electrons. The molecules on the left and right are in separate partitions and the molecule on the right is broken into two additional partitions.

is the same for each fragment as discussed in Ref. 43. The choice of Γ simply affects the convergence rate of the occupation numbers.

As an example of this inversion procedure we calculate the partition potential, occupation numbers, and chemical potential of a noninteracting system of eight electrons in the potential $v_{\text{ext}}(x) = \sum_{a=1}^{8} \tilde{v}_a(x)$, where

$$\tilde{v}_a(x) = \frac{-1}{\cosh^2\left[x - (-10.5 + 3a)\right]} \tag{3.14}$$

The fragment potentials are $v_1(x) = \sum_{a=1}^{2} \tilde{v}_a(x)$, $v_2(x) = \sum_{a=3}^{4} \tilde{v}_a(x)$, $v_3(x) = \sum_{a=5}^{6} \tilde{v}_a(x)$, and $v_4(x) = \sum_{a=7}^{8} \tilde{v}_a(x)$. The results of this PDFT inversion are shown in Fig. 3.5 and the converged chemical potential is -0.578. The partition potential is attractive in the central region and between the fragments but it is slightly repulsive in the region $|x| > 6$. The convergence of the occupation numbers for two different

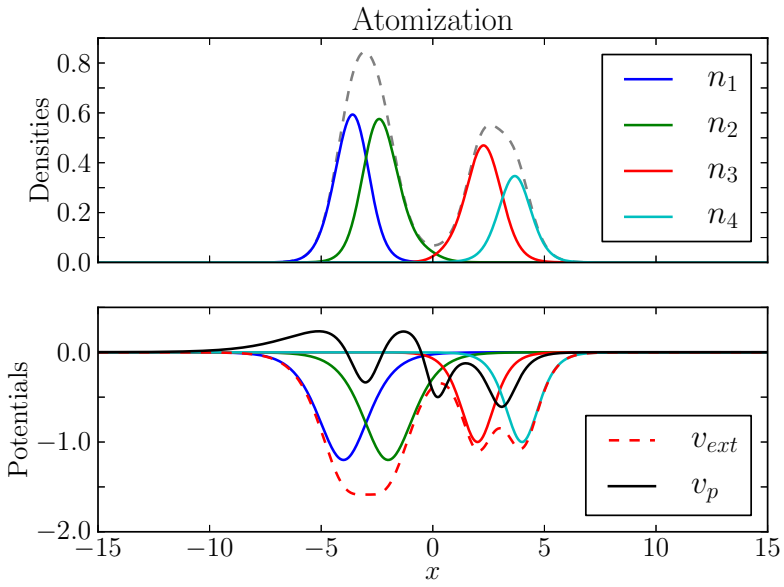

Figure 3.4. The fragment densities (top) and potentials (bottom) for a system of four noninteracting electrons. Each of the four nuclei forms a separate partition.

Γ values is also shown in Fig. 3.5 and have the same limit. (Only the occupation numbers for one side of the box are shown because the system is symmetric through the origin.) It is important in this inversion method to ensure that the DFT inversion performed at each iteration in computing $v_{\text{ext}}\left[n^{(k)}\right](\mathbf{r})$ contains no systematic errors because they will build up and pollute the partition potential at later iterations.

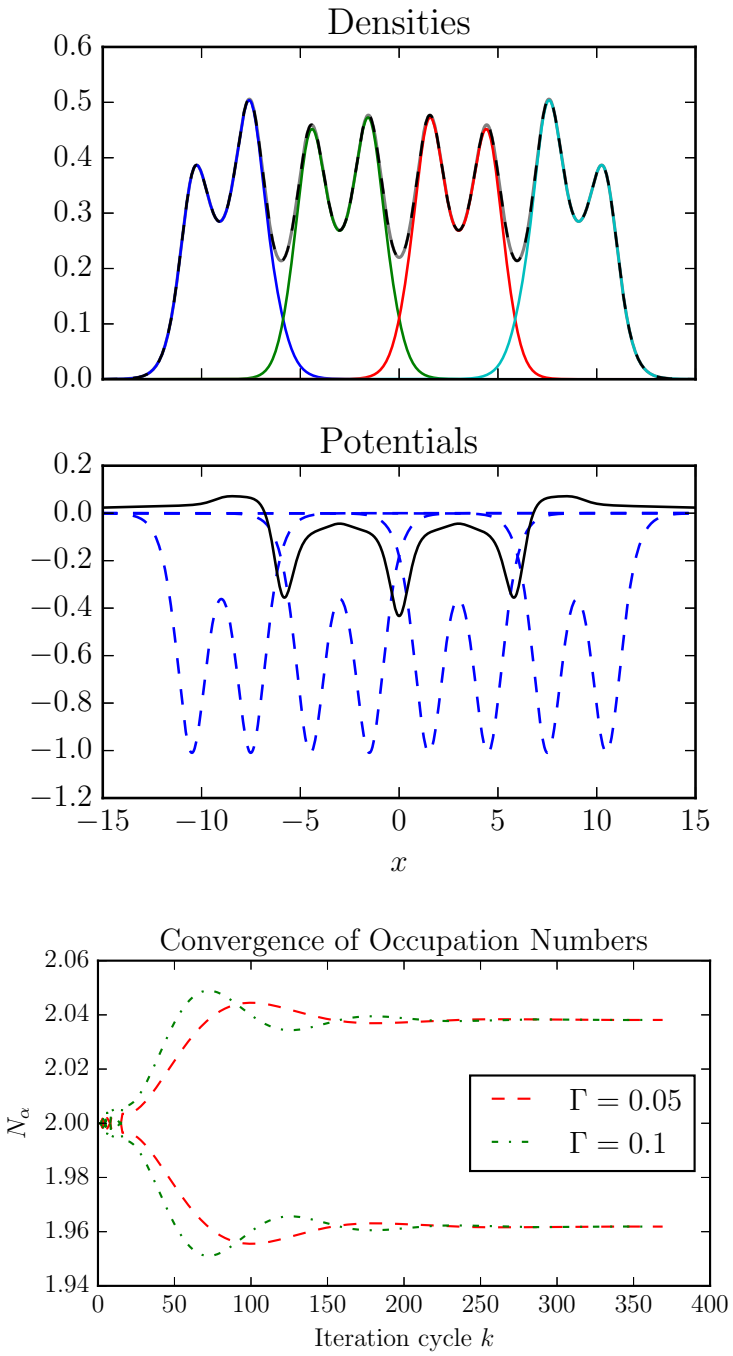

Figure 3.5. The fragment and molecular densities (top) for a system of eight noninteracting electrons in an external potential consisting of eight equally spaced inverse hyperbolic cosine squared potentials (dashed blue, middle). The converged partition potential (solid black, middle) for this system is attractive in the region $|x| < 6$ and repulsive in the region $|x| > 6$. The convergence of the fragment occupation numbers (bottom) shows that the system prefers nonintegral occupation values.

4. Inversions in Time-Dependent Density Functional Theory

This chapter contains work from the article entitled 'Numerical density-to-potential inversions in time-dependent density functional theory' written by Adam Wasserman and the author. [51]

We treat the density-to-potential inverse problem of time-dependent density functional theory as an optimization problem with a partial differential equation constraint. The unknown potential is recovered from a target density by applying a multilevel optimization method controlled by error estimates. We employ a classical optimization routine using gradients efficiently computed by the discrete-adjoint method. The inverted potential has both a real and imaginary part to reduce reflections at the boundaries and other numerical artifacts. We demonstrate this method on model one-dimensional systems. The method can be straightforwardly extended to a variety of numerical solvers of the time-dependent Kohn-Sham equations and to systems in higher dimensions.

4.1 Time-Dependent Density Functional Theory

Time-dependent density-functional theory (TDDFT) is a formally exact theory for time-dependent many-body systems. It uses the time-dependent density $n(\mathbf{r}, t)$ as the basic variable instead of the many-body wave function. This is made possible by the Runge-Gross theorem, which shows that for a given electronic Hamiltonian and initial state there exists a unique mapping between the density $n(\mathbf{r}, t)$ and the external potential $v_{\text{ext}}(\mathbf{r}, t)$ up to an arbitrary time-dependent constant. [52] The Kohn-Sham formalism can also be applied to TDDFT in what is known as Kohn-Sham time-dependent density functional theory.

4.1.1 The Direct and Inverse Problems

In Kohn-Sham TDDFT we define a non-interacting system of particles moving in an effective potential $v_s(\mathbf{r},t)$. The initial Kohn-Sham state Φ_0 from a DFT calculation is propagated in time via the time-dependent Kohn-Sham (TDKS) equations

$$\imath\frac{\partial}{\partial t}\phi_i(\mathbf{r},t) = \left[-\frac{1}{2}\boldsymbol{\nabla}^2 + v_s(\mathbf{r},t)\right]\phi_i(\mathbf{r},t), \tag{4.1}$$

where the TDKS potential is

$$v_s(\mathbf{r},t) = v_{\text{ext}}(\mathbf{r},t) + v_{\text{H}}(\mathbf{r},t) + v_{\text{xc}}(\mathbf{r},t). \tag{4.2}$$

The density is then given by

$$n_s(\mathbf{r},t) = \sum_i |\phi_i(\mathbf{r},t)|^2 \tag{4.3}$$

and is, by definition, equal to the density of the interacting system:

$$n_s(\mathbf{r},t) = n(\mathbf{r},t). \tag{4.4}$$

The existence of the TDKS potential v_s is guaranteed through the proof of Ref. [53]. The exchange-correlation portion of $v_s(\mathbf{r},t)$ is difficult to find because it is a functional of the history of the density $n(\mathbf{r},t'<t)$, the initial interacting state Ψ_0, and the initial KS state Φ_0. This added complication in TDDFT is currently its greatest weakness as we still do not have a useful universal functional of time. [6, Pg. 148] Adiabatic approximations are typically used but have varying levels of success. [54]

Time-dependent density functional theory (TDDFT) is a formally exact theory that has found widespread use in areas where interactions are important but the direct solution of the Schrödinger equation is too demanding. [55] The original theoretical basis for TDDFT comes from a proof of the one-to-one mapping between a given time-dependent density and external potential for a compatible initial interacting

many-body state. [52] The Kohn-Sham (KS) formulation of TDDFT uses the one-to-one mapping to define a noninteracting system that moves in an effective potential and reproduces the density of the interacting system. The effective potential is called the KS potential and the exchange-correlation part of this potential contains the complicated many-body effects. The exchange-correlation potential is approximated in all nontrivial TDDFT calculations.

The forward or direct problem in TDDFT is to find the time-dependent density from an approximate exchange-correlation potential via the time-dependent Kohn-Sham (TDKS) equations. [52] This forward problem is well posed in the sense of Hadamard, [13] which means that a solution exists, it is unique, and it depends continuously on the data. Thanks to these properties, there currently exist several numerically accurate and stable methods for solving the forward problem. [56] However, the inverse problem of numerically finding the potential from a given density requires extra precautions to avoid violating one or more of Hadamard's existence, uniqueness, and stability conditions. The goal of this paper is to explain what these extra precautions are and show how the inverse problem of TDDFT can also be solved with a variety of numerical methods.

The inverse problem of TDDFT is mainly of interest to developers of approximate exchange-correlation functionals. In this case the inverse problem is solved to find the exchange-correlation potential for systems where the many-body density is known and examined to see what important features should be present in approximate potentials. Such studies have shown dynamical step structures with spatial and temporal nonlocal density dependence, [57, 58] an initial-state dependence and corresponding memory effects, [30, 59] and v-representability problems for certain lattice systems. [60, 61] Similarly, related inverse problems for extensions of TDDFT such as time-dependent current density functional theory (TDCDFT) [62] and partition time-dependent density functional theory (P-TDDFT) [63] are also instrumental in developing new approximations.

4.2 Inversion Algorithms

Several density-to-potential inversion schemes for TDDFT already exist despite the challenging nature of the problem. In the case of one-orbital systems there are analytical inversion formulas [64, 65] that are numerically stable everywhere the density is nonzero but can produce unphysical oscillations in the inverted potential in certain low-density regions as seen in Ref. 65. The inversion algorithms in Refs. 58, 59 move beyond one-orbital systems and are successful provided that extra precautions are taken to maintain stability. The inversion method of Ref. 59 smooths the inverted potential at each time step in order to obtain stability and the algorithm of Ref. 58 uses a gauge transformation to improve numerical stability.

Our experience has shown that the stability problems hinted at in the previous paragraph arise mainly from two implementation issues. The first issue is the step-by-step (in time) nature of all but the one-orbital inversion formulas. In Refs. 58–60 the potential at a given time step is found from an iterative procedure that only uses information from the previous time step. As explained in Ref. 66, this is theoretically correct to do but assumes that the potential at a given time step can be recovered with negligible error. If the potential at a given time step does have a nonnegligible error then it will severely reduce the accuracy of the inversion at later time steps. This effect can be alleviated somewhat through smoothing, [59] gauge transformations, [58], or regularization methods [60] but it eventually ruins the solution in longer time runs or when the density comes close to failing the conditions for v-representability.

The second stability issue involves a division by the target density present in all of the current TDDFT inversion algorithms. [58, 59, 64, 65] Such divisions are also common in density functional theory (DFT) inversion algorithms. [32] In both cases the density division serves to rescale the problem and accelerate the inversion in the low-density regions. Unfortunately, the relative error of the density in the asymptotic regions of nonperiodic TDDFT problems can be inaccurate by orders of magnitude unless special boundary conditions are applied. [67] The inaccuracy can be lessened

somewhat by computing the interacting target density on the same grid with the same boundary conditions and similar propagator as the noninteracting KS system. [58] This restriction will give the densities more similar asymptotic properties but is a severe restriction on the systems that can be studied and is not guaranteed to work for longer time runs. We briefly illustrate this stability problem and other numerical issues in App. A.

In this paper we present an unconditionally stable TDDFT inversion algorithm that avoids the stability problems described above. The algorithm is based on a constrained partial differential equation (PDE) optimization framework and is described in Sec. 4.3. Section 4.3.1 contains a broad overview of the algorithm with details on how the method can be scaled to higher dimensions and applied to problems with missing or noisy data. Section. 4.3.2 contains numerical details specific to the inversion examples shown in Sec. 4.4. The various strengths and weaknesses of the algorithm are discussed in Sec. A.2 along with possible improvements.

4.3 Inversion via PDE-constrained optimization

The TDDFT density-to-potential inverse problem is a nonlinear parameter identification problem. The exchange-correlation potential $v_{\mathrm{xc}}(\mathbf{r},t)$ is usually the unknown parameter to be recovered from a given target density and initial conditions. The density $n(\mathbf{r},t)$ must satisfy the TDKS equations

$$\imath\frac{\partial}{\partial t}\phi_j(\mathbf{r},t) = \left[-\frac{1}{2}\boldsymbol{\nabla}^2 + v_{\mathrm{ext}}(\mathbf{r},t) + v_{\mathrm{H}}([n],\mathbf{r},t) + v_{\mathrm{xc}}([\Psi_0,\Phi_0,n],\mathbf{r},t)\right]\phi_j(\mathbf{r},t) \text{ and} \tag{4.5}$$

$$n(\mathbf{r},t) = 2\sum_{j=1}^{N}|\phi_j(\mathbf{r},t)|^2, \tag{4.6}$$

where $\{\phi_j\}$ are the KS orbitals, v_{ext} is the external potential, v_{H} is the Hartree potential, v_{xc} is the exchange-correlation potential, Ψ_0 is the initial interacting many-body

state, and Φ_0 is the initial noninteracting state. The already complicated functional dependence of the exchange-correlation potential is further complicated by a dependence on the history of the density $n(\mathbf{r}, t' < t)$. [57] Equations 4.5 and 4.6 are written for a closed-shell system with $2N$ electrons. A thorough explanation of the TDKS equations can be found in Ref. 66. The source of nonlinearity for this inverse problem is described in detail in Ref. 53.

In this section we show how to apply PDE-constrained optimization to the TDDFT inverse problem. In most of our examples the PDE constraint is the TDKS equations shown in Eqs. 4.5-4.6. PDE-constrained optimization is a common solution method for nonlinear parameter identification, optimal control, and optimal design problems governed by PDEs. [37] In fact, the mathematical structure and computational design of the quantum optimal control theory (QOCT) problem using TDDFT [68] is very similar to the inversion method we describe here. We also use insights gained from general QOCT problems described in Refs. 69, 70.

4.3.1 TDDFT inversion algorithm

In our TDDFT density-to-potential inversions we minimize the cost functional

$$F_n[v] = \frac{1}{2} \left\| n([v], \mathbf{r}, t) - \tilde{n}(\mathbf{r}, t) \right\|_2^2, \tag{4.7}$$

where $n([v], \mathbf{r}, t)$ is the probability density corresponding to the potential v and the subscript 2 refers to the L^2 norm. One can also minimize[2]

$$F_{\mathbf{j}}[v] = \frac{1}{2} \left\| \mathbf{j}([v], \mathbf{r}, t) - \tilde{\mathbf{j}}(\mathbf{r}, t) \right\|_2^2, \tag{4.8}$$

where $\mathbf{j}(\mathbf{r}, t)$ is the current probability density but it is only required if the system is periodic in space and TDCDFT is needed. [71] The target densities $\tilde{n}$ and $\tilde{\mathbf{j}}$ are fixed

[2]All of the examples in this chapter are finite systems so we only use Eq. (4.7). We have used Eq. (4.8) for some of these systems but the results are very similar with no clear advantage over Eq. 4.7.

during the minimization. In most cases the potential v corresponds to the exchange-correlation potential v_{xc} but it could also be the partition potential v_{p} as in Sec. 4.4.4. In most TDDFT inversions the external potential is given and the Hartree potential can be precomputed using the target density so that only the exchange-correlation potential is unknown.

Many classical optimization routines require derivatives of the cost functional being minimized. [72] We compute these derivatives with the discrete-adjoint method [73] due to the constraints of our inverse problem. In particular, we need a very large number of parameters to describe the potential being inverted and many of the propagators for the TDKS equations rely on iterative methods. [56] Finite difference, automatic differentiation, and continuous adjoint methods could also be used but we found the discrete-adjoint method to work best for our inversions. A thorough comparison of these different methods applied to a QOCT problem can be found in Ref. 69 and also concludes that the discrete-adjoint method is the most effective method for computing QOCT cost-functional derivatives. The discrete adjoint formula for a general cost functional and multistep TDKS propagator is given in App. B.

We employ a multilevel inversion scheme to accelerate our numerical inversions. The method is driven by error estimates to avoid fitting to errors in both the target density and the discretization method applied to the TDKS equations. The general method is similar to that described in Ref. 74 but we use an error estimate for the cost functional instead of the norm of the cost-functional gradient. A guess for the unknown potential is given at the first level, an error estimate is computed, and a gradient-based optimizer minimizes the cost functional. The optimizer stops when the error estimate from either the target density or the propagation method is reached. The grid is then refined, the potential at the current iteration is interpolated to the finer grid, and the process repeats until the potential converges to the user's desired accuracy or the target density error is reached. If the discretization method's spatial and temporal order of accuracies are similar then we quadratically increase the number of points on the temporal grid and linearly increase the number of points

on the spatial grid at each level. This refinement difference is due to the structure of the time-dependent Schrödinger equation as explained in Ref. 70.

The multilevel inversion scheme described above is efficient, flexible, and robust by design. Much of the efficiency comes from using a constrained-PDE formulation of the inverse problem and only searching over the space of potentials that satisfy the TDKS equations. The choice of optimization and discretization methods is flexible and this flexibility can further increase the scheme's efficiency as described below. The use of error estimates ensures that the inverted potential at each level of the multilevel scheme satisfies two different discretizations of the TDKS equations, (the two schemes used to produce the error estimate), to avoid fitting to numerical errors. Furthermore, by including the error estimate for the target density in the algorithm we are able to look at a wide range of target densities as shown in Sec. 4.4. The formulas in this section and App. B apply to multiple dimensions so our inversion method is not limited to one-dimensional toy problems.

Our inversion scheme also contains a number of disadvantages largely dependent on the choice of discretization and optimization methods. Some of these disadvantages are discussed here as well as in Sec. A.2 with suggestions for possible improvements. As is common in PDE-constrained optimization, the discretization of the TDDFT inverse problem tends to produce very large systems of equations with many unknown variables. [37] Furthermore, our optimization problems are poorly scaled because the densities in the asymptotic regions are orders of magnitude smaller than the densities near the nuclei. The multilevel method used in tandem with a large-scale optimization routine insensitive to poor scaling is very effective at dealing with these two issues. Our choice of classical optimizer and grid refinements described in Sec. 4.3.2 partially resolves these issues but still struggles in some of the low-density regions.

Our experience has shown that density reflections from the computational boundaries and the lack of norm preservation in propagators of the TDKS equations greatly hinder the optimization portion of our algorithm and lead to spurious numerical artifacts in the inverted potentials. In order to reduce the reflections from the boundaries

we implement the exponential complex absorbing boundary condition described in Ref. 75. Although we could use higher-order propagators to better preserve the norm of the density we instead allow the imaginary portion of the potential to be variable and make constant shifts at each time step. These constant shifts allow the optimizer to renormalize the density and avoid spurious potential jumps as explained in App. A.

The examples that we consider in Sec. 4.4 all appear to be well posed in that they approach a unique answer up to a purely time-dependent function. Analytically, the arbitrary purely time-dependent function in the Runge-Gross Theorem [52] doesn't affect the solution but numerically it does as shown in App. A. The optimizer appears to choose this function based on the initial guess and the grid parameters with a strong preference for continuous functions. A similar phenomenon occurs in the ground state DFT problem where the numerical PDE solver chooses the arbitrary phase of the KS orbitals based on the choice of grid parameters as seen in App. A.

In the case that we do encounter an ill-posed TDDFT inverse problem, (perhaps from incomplete experimental observations), a variety of regularization methods can be used to solve the problem. [14] One possibility is to use Tikhonov regularization by adding a Sobolev H^1 penalty functional

$$R\left([v],\alpha\right) = \alpha\left(\left\|\boldsymbol{\nabla} v\right\|_2^2 + \left\|\frac{\partial v}{\partial t}\right\|_2^2\right), \tag{4.9}$$

to the cost functional, where $\alpha > 0$ is the regularization parameter. This functional penalizes highly oscillatory potentials and is similar to the penalty functionals used in QOCT problems. [68] Other cost functionals could be devised that favor potentials satisfying exact conditions such as those described in Ref. 76.

4.3.2 Numerical implementation

In this section we describe the numerical details of the multilevel TDDFT inversion algorithm described in Sec. 4.3.1. We specify the finite difference schemes used for

discretizing the TDKS equations and how they are employed in the optimization procedure. Details about the optimization procedure, boundary conditions, initial guess, and grid refinement are given. The role of the imaginary part of the potential is also explained.

We mainly use two different finite difference schemes to discretize the TDKS equations during the inversion procedure. The Crank-Nicolson (CN) propagator [56] combined with a fourth-order finite difference approximation to the Laplacian is used at every iteration. This scheme is relatively simple to differentiate when implementing the discrete-adjoint method thanks to the linear nature of the operators as shown in App. B. During some of the iterations, we also implement the enforced time-reversal symmetry (ETRS) method [56] with an eighth-order finite difference approximation to the Laplacian. This higher-order method is used to compute error estimates and thus avoid fitting to numerical errors from the CN scheme. Both discretizations are for uniformly-spaced temporal and spatial grids with infinitely-high walls at the boundaries. The target densities in Secs. 4.4.3 and 4.4.5 are computed using different discretizations as explained in detail in those sections. The presence of an imaginary potential discussed below affects the stability of both discretization schemes. In particular, the negative imaginary portions of the potential become positive during backwards propagation of the TDKS equations and can lead to unbounded growth. We therefore store the TDKS orbitals during the forward propagation for use in the adjoint equations. Another way to avoid backwards propagations and reduce memory requirements is through the use of a checkpointing scheme. [77]

The examples in Secs. 4.4.1-4.4.4 use an initial grid spacing of 1 for both the temporal and spatial grids. The example in Sec. 4.4.5 uses initial grid spacings of 0.1 since the external potential is already known and the initial error is so small. The number of grid points increases according to the formulas $t\,(1+M^2)$ and $x\,(1+M)$, where M is the current level, t is the initial number of temporal grid points, and x is the initial number of spatial grid points. The solution at a given level is linearly interpolated to the new grid before beginning the next level of optimization. The

exponential complex absorbing potential of Ref. 75 is applied to 25% of the total grid at both boundaries with a value of $-\imath$ obtained at the edges for the examples in Secs. 4.4.1-4.4.4. The example in Sec. 4.4.5 uses a smaller value of $-\imath/100$ at the edges to avoid losing too much density. This absorbing potential is not optimized for any of the problems and simply reduces density reflections from the boundaries. We also allow the imaginary part of the potential between the absorbing portions to vary by constant shifts and thus renormalize the density that is lost at the boundaries.

We begin the inversion procedure by providing a guess for the unknown potential. Currently we use an initial guess of zero as this allows us to clearly see how the optimization is proceeding. (More physically-motivated guesses could be used perhaps based on the one-orbital formulas in Refs. 64, 65.) The error estimate F_n^{err} is then found using the formula

$$F_n^{\text{err}}[v] = \frac{1}{2}\left\|n^{\text{CN}}([v],\mathbf{r},t) - n^{\text{ETRS}}([v],\mathbf{r},t)\right\|_2^2 \tau, \tag{4.10}$$

where n^{CN} and n^{ETRS} are the densities found using the CN and ETRS discretizations, respectively and $\tau = 10$. (A similar formula can be used when the current density is the basic variable as in Eq. 4.8.) Since the L^2 norm can produce overflow we scale it by the product of the grid spacings. This scaling also allows us to compare costs on different grids as it is essentially a numerical approximation to the continuous L^2 norm computed with the midpoint integration rule.

The truncated-Newton (TN) algorithm of Ref. 39 as implemented in the SciPy library [26] is used to perform the optimization at each level of the multilevel scheme. This algorithm and other gradient-based optimization routines tend to produce large changes in the cost functionals during the initial iterations and smaller changes later in the optimization. Because of these large initial changes, we update the error estimate on a base-10 logarithmic scale during each optimization to avoid fitting to numerical errors. The optimization at a given level ends when the optimizer has reduced the cost functional to either the error estimate from Eq. 4.10 or the error estimate provided by

the user for the target density. If a line search fails during the optimization then we add 1% random noise to the potential at the current iteration. These two precautions of updating the error estimate and recovering from failed line searches only play a role in our examples in Sec. 4.4 when coarse grids are being used.

4.4 Inversion examples

In this section we present several benchmark inversion examples as well as some comparison examples from other TDDFT inversion algorithms. The benchmark examples illustrate many of the strengths and limitations of our inversion algorithm described in Sec. 4.3. The other inversion examples demonstrate the generality and unconditional stability of our algorithm.

4.4.1 Noninteracting harmonic potential theorem inversion

In our first benchmark example we form a noninteracting system of three orbitals satisfying the harmonic potential theorem [78]. The initial KS orbitals are the ground and first two excited states of the harmonic oscillator given in Eqs. C.6-C.7. The time-dependent density to be inverted

$$n\left(x,t\right)=\sum_{i=0}^{2}\left|\psi_{i}\left[x-x_{s}\left(t\right)\right]\right|^{2}, \tag{4.11}$$

is the initial density shifted harmonically by

$$x_{s}\left(t\right)=\frac{F_{0}}{1-\omega^{2}}\sin\left(\omega t\right). \tag{4.12}$$

The exact KS potential that produces Eq. 4.11 is

$$v\left(x,t\right)=\frac{1}{2}x^{2}-F_{0}\sin\left(\omega t\right)x+C\left(t\right), \tag{4.13}$$

where $C(t)$ is an arbitrary time-dependent function. In the following inversions we set $F_0 = 1$ and $\omega = 0.3$. The spatial grid runs from -10 to 10 and the temporal grid runs from 0 to approximately 63 for a total of three complete cycles.

The target density provided by Eq. 4.11 is analytic so our only limitations in this problem come from discretizing the TDKS equations. We perform eleven levels of our multilevel inversion algorithm with the final grid containing 6263 temporal points and 221 spatial points. In Fig. 4.1 we plot the inverted and exact potentials along with the error in the inverted density. We also plot several snapshots of the same data in Fig. 4.2. The potential is only recovered succesfully in the regions where the density is larger than 10^{-3} as seen clearly in Fig. 4.2. Furthermore, there are numerical artifacts in the form of small wiggles in the inverted potential indicating a lack of convergence. This example clearly indicates how the inversion procedure using the L^2 norm fits the larger densities first and then works down to the smaller densities in the asymptotic region.

4.4.2 Particle in a harmonic potential well

In this example we invert the density

$$n(x,t) = \left[\cos(\omega t)\,\psi_0(x) + \sin(\omega t)\,\psi_1(x)\right]^2, \tag{4.14}$$

where ψ_0 and ψ_1 are given in Eqs. C.6-C.7 and $\omega = 2\pi/100$. The initial KS orbital is $\psi_0(x)$. The original problem considered in Ref. 60 replaces the time variable with the function $\tau(t) = t^4/(1+t^3)$ in order to include only gentle perturbations of the density at times $t \ll 50$. Our results show that the nodes in the density of Eq. 4.14 are the main source of difficulty for this problem as opposed to the initial density changes as explained below.

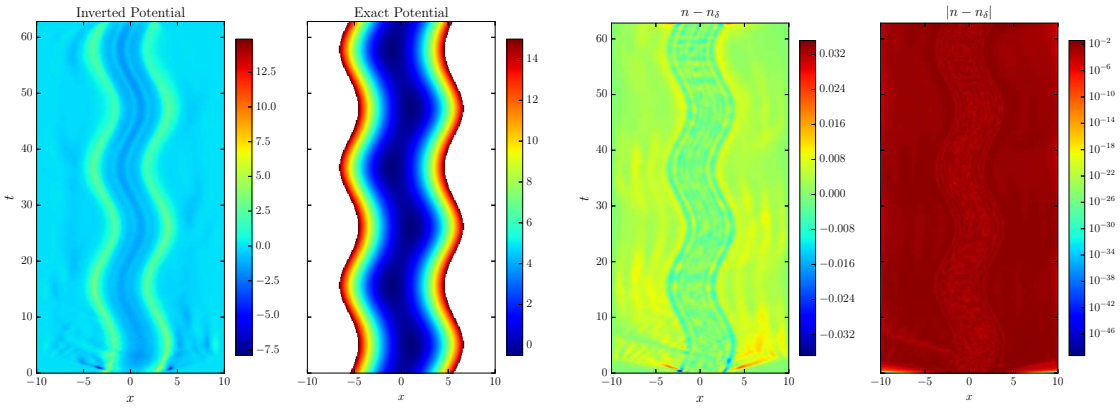

Figure 4.1. The inverted potential (left), exact potential (center left), and density error (right) for a system of three orbitals satisfying the harmonic potential theorem as described in Sec. 4.4.1. Values of the exact potential greater than 15 are masked for better comparison with the inverted potential. The exact density at the edge of the box at $t = 0$ is about 4×10^{-40} so the very small density differences on the order of 10^{-46} for short times ($t < 1$) show that the inverted and exact densities agree to about 6 digits of precision. This same level of accuracy will likely be required at later times to correctly invert the density in the asymptotic regions. A similar analysis applies to the logarithmic plots in Figs. 4.3, 4.5, 4.7, and 4.9.

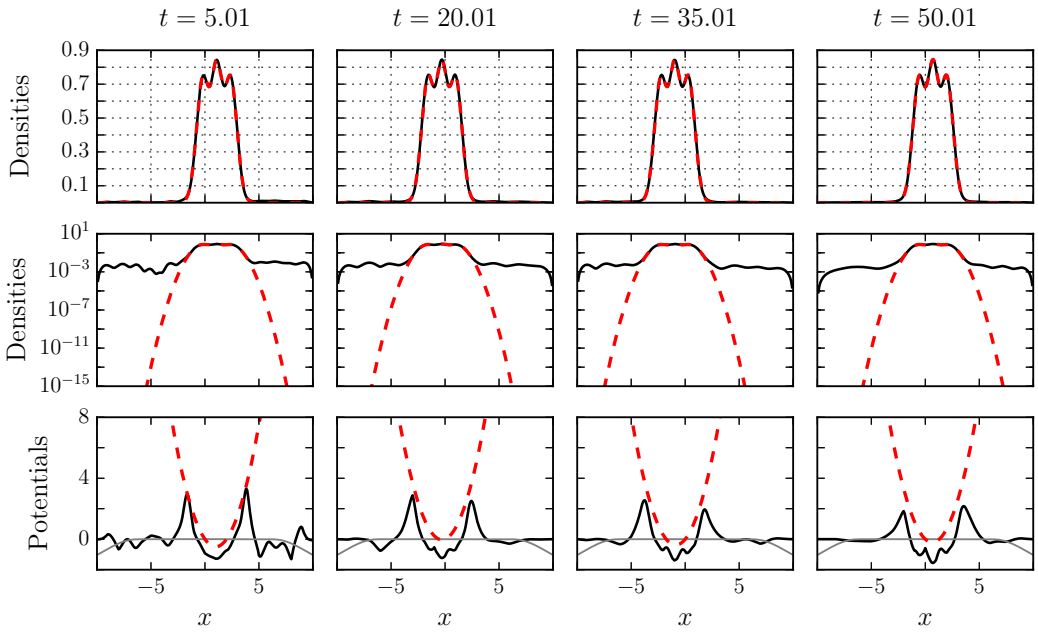

Figure 4.2. Snapshots of the inversion described in Sec. 4.4.1 for a noninteracting system of three orbitals satisfying the harmonic potential theorem. The red dashed lines indicate exact values and the solid black lines are the results of our numerical inversion algorithm. The solid gray line is the imaginary portion of the potential.

As a one-orbital system, the density in Eq. 4.14 can be inverted to find the KS potential using the one-orbital inversion formula of Ref. 64. The orbital at all times $t \neq 50n$, n an integer, is $\phi(x,t) = e^{\imath\alpha(x,t)} |f(x,t)|$, where

$$\begin{aligned}\alpha(x,t) =& \frac{\omega \log\left|\sqrt{2}\sin(\omega t)\, x + \cos(\omega t)\right|}{\tan(\omega t)} \\ &- \frac{\omega\cos^2(\omega t) - \omega}{\sin(\omega t)\left[\sqrt{2}\sin(\omega t)\, x + \cos(\omega t)\right]} \text{ and} \qquad (4.15)\end{aligned}$$

$$f(x,t) = \cos(\omega t)\,\psi_0(x) + \sin(\omega t)\,\psi_1(x)\,. \qquad (4.16)$$

The nodes in the density are located at $x = -1/\left[\sqrt{2}\tan(\omega t)\right]$ and produce strong singularities in the potential according to the formula

$$\delta\left[f(x,t)\right]\frac{\left[f_x(x,t)\right]^2}{|f(x,t)|}, \qquad (4.17)$$

where δ is the delta function. The inversion in Ref. 60 likely fails around $t = 5$ because the node is well within the computational box by that time and the inversion algorithm being used divides by the density.

The target density provided by Eq. 4.14 is analytic so our only limitations in this problem come from discretizing the TDKS equations. We perform eleven levels of our multilevel inversion algorithm with the final grid containing 5556 temporal points running from 0 to 55 and 177 spatial points running from -8 to 8. In Fig. 4.3 we plot the inverted and exact potentials along with the error in the inverted density. We also plot several snapshots of the same data in Fig. 4.4. Our inversion algorithm clearly captures the highly singular behavior of this potential without any special modifications to account for the singularities. It does, however, fail to recover the asymptotic behavior similar to the example in Sec. 4.4.1.

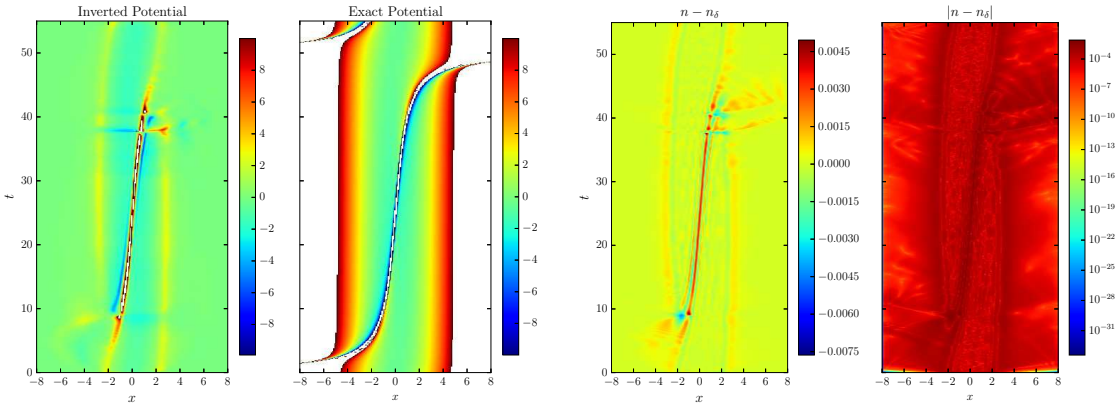

Figure 4.3. The inverted potential (left), exact potential (center left), and density error (right) for a particle in a harmonic potential well as described in Sec. 4.4.2. Values of the exact potential outside the range [-10, 10] are masked for better comparison with the inverted potential.

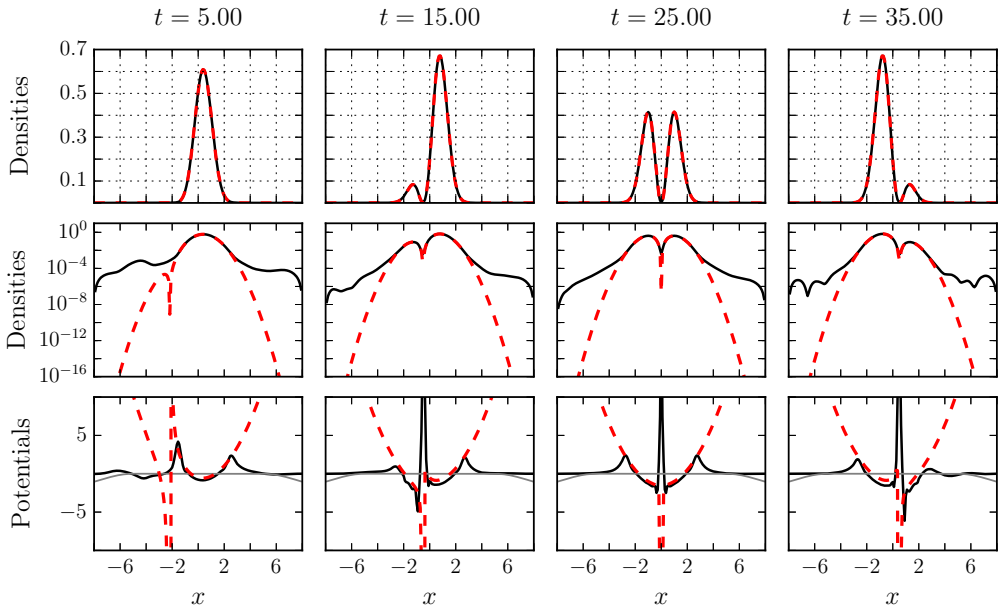

Figure 4.4. Snapshots of the inversion described in Sec. 4.4.2 for a particle in a harmonic potential well. The delta function for our inverted potential has a maximum value of approximately 92 and the delta function for the exact solution is not shown. The red dashed lines indicate exact values and the solid black lines are the results of our numerical inversion algorithm. The solid gray line is the imaginary portion of the potential.

4.4.3 Sudden turn-on potential inversion

In this benchmark problem we invert the density of a sudden turn-on potential. The potential to be inverted is

$$v(x,t) = -\cosh^{-1}(x+2) - \mathcal{H}(t-1)\cosh^{-1}(x-4), \tag{4.18}$$

where $\mathcal{H}$ is the Heaviside function. The wells are purposely placed asymetrically in the computational region to make sure that symmetry does not aid the inversion procedure. We approximate the Heaviside function using the formula

$$\mathcal{H}(t) \approx [1+\exp(-2kt)]^{-1}, \tag{4.19}$$

where $k = 10$. The initial KS system is the ground state of an electron in the left well. At $t = 1$ the right well suddenly appears and the electron very slowly shuttles back and forth between the two wells.

In this example we do not have an analytic form of the density so we compute it numerically along with an error estimate. If the same propagation method and grid are used for both the forward and inverse problems then it is possible to get nearly perfect results. Such a simulation is often referred to as an inverse crime and is not representative of a typical TDDFT inversion. (For a thorough review of inverse crimes see Ref. 16.) For this reason we compute the target density on a different grid with a different spatial discretization. We implement the infinite-to-finite spatial grid mapping of Ref. 31 with a scaling parameter of $\alpha = 8$ to reduce reflections at the boundaries. This mapping is used with both the CN and ETRS propagators, where the second derivative is sixth-order in the CN method and eighth-order in the ETRS method. The temporal grid has 20001 temporal grid points running from 0 to 500 and 2001 spatial grid points. The cost functional is computed once using the CN propagator and then again with the ETRS propagator to form an error estimate using Eq. 4.10.

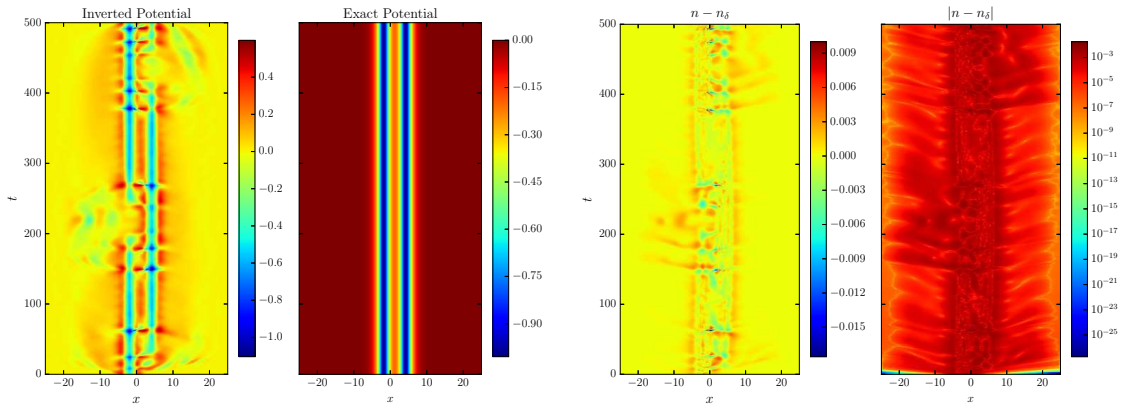

Figure 4.5. The inverted potential (left), exact potential (center left), and density error (right) for a sudden turn-on potential at $t = 1$ as described in Sec. 4.4.3.

We perform three levels of our multilevel inversion algorithm with the final grid containing 5001 temporal points and 201 spatial points. At this level of the algorithm the target density's error estimate is not obtained so the convergence criterion is just that of Eq. 4.10. In Fig. 4.5 we plot the inverted and exact potentials along with the error in the inverted density. We also plot several snapshots of the same data in Fig. 4.6. These results show that our inversion method is capable of performing very long density-to-potential inversions in time with no stability issues. However, we again see that the potential is not resolved in the asymptotic region and the density is only accurate to approximately 10^{-3}. Unfortunately, the density in the asymptotic region is the only density that changes significantly right after the second potential appears so our inversion misses this change and shows the second potential appearing later than it should. There are also several sharp wiggles as seen in Fig. 4.6 resulting from this delayed reaction as the optimizer unphysically shifts density from one well to the other that would have been in the correct location if the second well had appeared at the correct time.

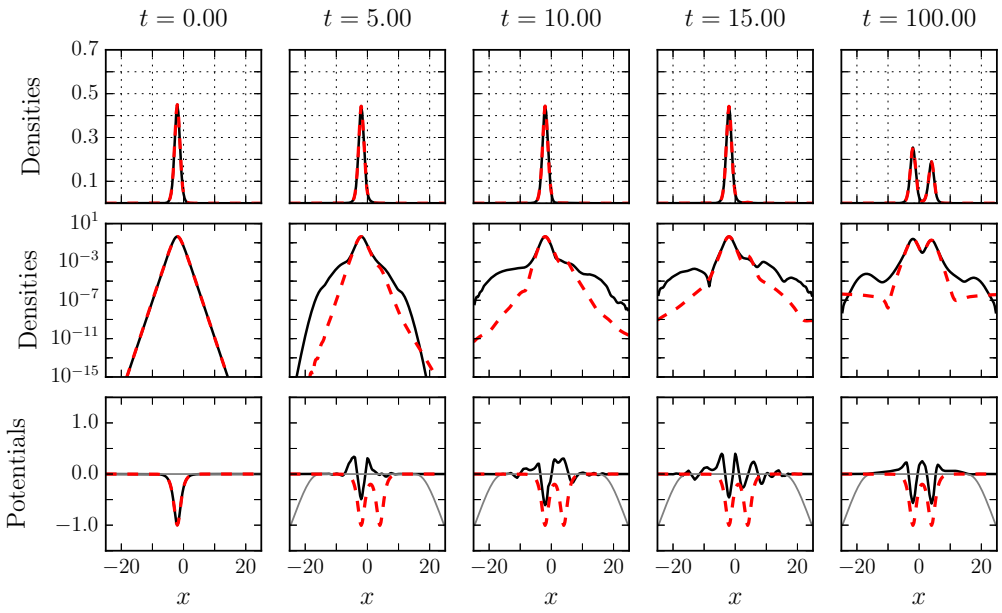

Figure 4.6. Snapshots of the inversion described in Sec. 4.4.3 for a sudden turn-on potential at $t = 1$. The red dashed lines indicate exact values and the solid black lines are the results of our numerical inversion algorithm. The solid gray line is the imaginary portion of the potential.

4.4.4 Partition Time-Dependent Density Functional Theory Inversion

In this example we have an electron subject to the electric field

$$v_E(x,t) = xE_0 \sin(\omega t) f(t), \tag{4.20}$$

where $\omega = 0.3$, $E_0 = 0.1$, and $f(t) = \exp(-t^2/25)$ is the pulse envelope. The pulse envelope is the only addition made here to the original example given in Ref. 63 in order to avoid excessive ionization. The static external potential is composed of two soft-Coulomb potentials of equal depth

$$v_a(x) = -1/\sqrt{(x+2)^2+1} \text{ and}$$
$$v_b(x) = -1/\sqrt{(x-2)^2+1}.$$

The target density is found using the same infinite-to-finite spatial grid mapping described in Sec. 4.4.3 with $\alpha = 4$. There are 1676 temporal grid points running from 0 to approximately 42. The other discretization parameters and procedures used to compute the target density are the same as those used in Sec. 4.4.3.

In the inverse P-TDDFT problem we search for the unknown partition potential satisfying the TDKS equations

$$\imath\frac{\partial}{\partial t}\phi_\alpha(x,t) = \left[-\frac{1}{2}\frac{\partial^2}{\partial x^2} + v_\alpha(x,t) + v_p(x,t)\right]\phi_\alpha(x,t), \tag{4.21}$$

where $\alpha = 1, 2$ and

$$v_1(x,t) = v_a(x) + v_E(x,t),$$
$$v_2(x,t) = v_b(x) + v_E(x,t).$$

For additional details about this partitioning choice and P-TDDFT in general, see Ch. 5 and Ref. 63. We perform 11 levels of our multilevel inversion algorithm with

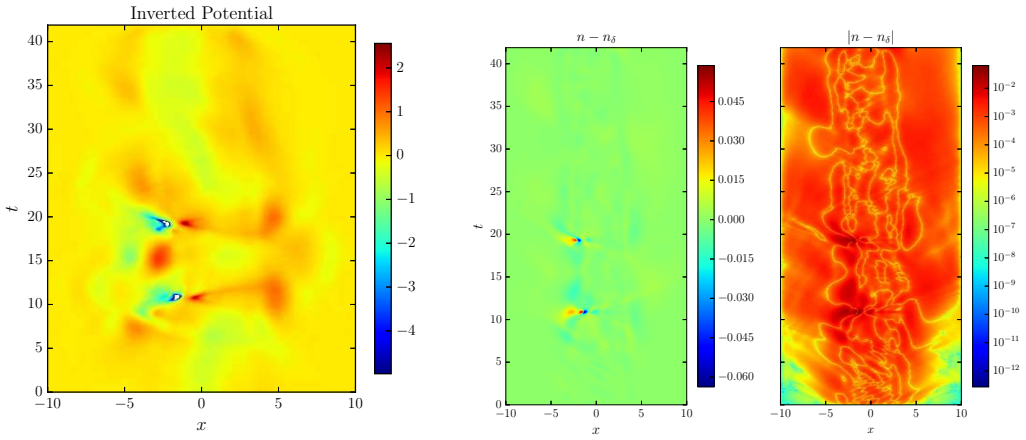

Figure 4.7. The inverted partition potential (left) and density error (right) for a one-electron system partitioned in two pieces with an applied electric field as described in Sec. 4.4.4. Values of the partition potential below -5 are masked.

the final grid containing 4142 temporal points and 221 spatial points. In Fig. 4.7 we plot the partition potential and the density error. We also plot several snapshots of the same data in Fig. 4.8. These results highlight our inversion method's ability to model rapidly changing systems with strong external fields. In contrast, the inversion algorithm in Ref. 63 fails to model this system shortly after $t = 5$. (These results are directly comparable since the envelope function does not suppress the electric field significantly until after $t = 5$.)

4.4.5 Two Interacting-Electrons Inversion

In this example we invert the density from two spinless electrons interacting through the soft-Coulomb interaction

$$V_{\text{ee}}(x_i, x_j) = (|x_i - x_j| + 0.1)^{-1}. \tag{4.22}$$

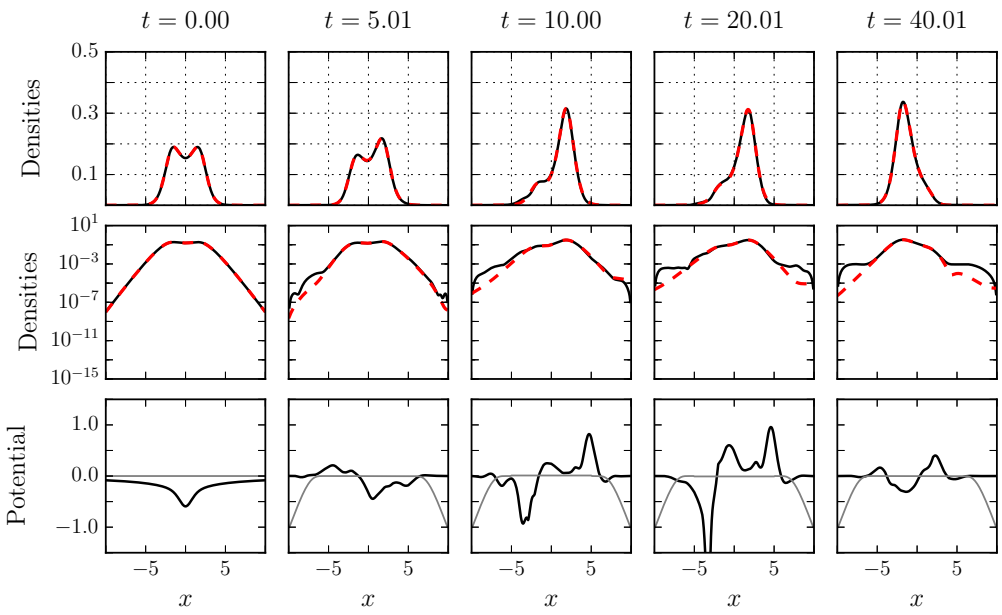

Figure 4.8. Snapshots of the P-TDDFT inversion described in Sec. 4.4.4 for a one-electron system partitioned in two pieces with an applied electric field. The red dashed lines indicate target values and the solid black lines are the results of our numerical inversion algorithm. The solid gray line is the imaginary portion of the potential.

The external potential is

$$V_{\text{ext}}(x_1, x_2, t) = \sum_{i=1}^{2} \alpha x_i^{10} - \beta x_i^4 - \varepsilon x_i \mathcal{H}(t), \tag{4.23}$$

where $\alpha = 5 \times 10^{-11}$, $\beta = 1.3 \times 10^{-4}$, $\varepsilon = 0.1$, and $\mathcal{H}$ is the Heaviside function. This external potential has a long flat barrier that the electrons can tunnel across and the uniform electric field drives this tunneling towards the right. This example is also studied in Ref. 58 and we use the same values to allow for a direct comparison.

We compute the interacting target density by combining the Peaceman-Rachford alternating direction implicit (ADI) method with the CN algorithm. We use a temporal grid spacing of 0.002 and a spatial grid spacing of 0.05 as in Ref. 58 but run our simulation for twice as long in time. Figures 4.9 and 4.10 show the results of our multilevel inversion algorithm for 5 levels, (2731 points in time and 1801 points in space). The effect of the Hartree exchange-correlation potential on the density during the times studied is minimal and our algorithm doesn't change it from the initial guess of zero. Since our algorithm uses the L^2 norm it focuses on the large densities and is not able to resolve the very small features in the central region studied in Ref. 58. Our algorith is, however, completely stable and the error estimates keep it from fitting to numerical errors in this example.

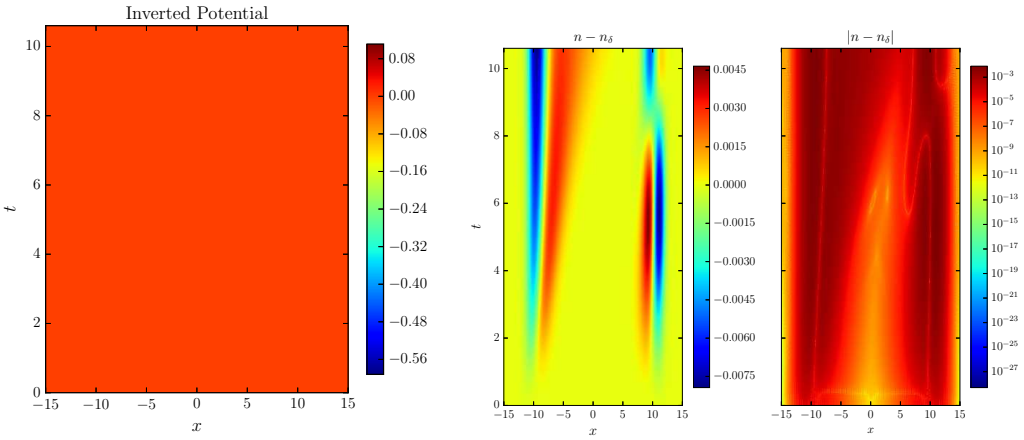

Figure 4.9. The Hartree exchange-correlation potential (left) and density error (right) for an interacting two-electron system as described in Sec. 4.4.5.

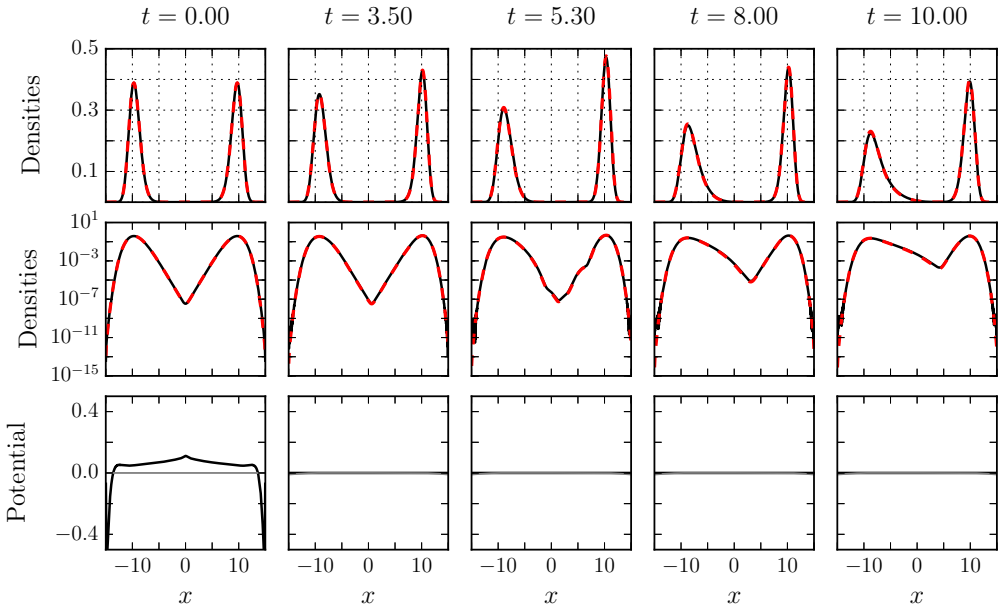

Figure 4.10. Snapshots of the interacting two-electron inversion described in Sec. 4.4.5. The red dashed lines indicate target values and the solid black lines are the results of our numerical inversion algorithm. The solid gray line is the imaginary portion of the potential.

5. Inversions in Partition Time-Dependent Density Functional Theory

This chapter contains work from the article entitled 'Fragment-Based Time-Dependent Density Functional Theory' written by Adam Wasserman, Martín Mosquera, and the author. [63]

5.1 Partition Time-Dependent Density Functional Theory

Partition time-dependent density functional theory (P-TDDFT) is an extension of partition density functional theory (PDFT) to time-dependent systems. For a given electronic Hamiltonian, initial state, and fragmentation choice, there is a unique single-particle time-dependent partition potential $v_{\mathrm{p}}(\mathbf{r},t)$. If $v_{\mathrm{p}}(\mathbf{r},t)$ is added to each fragment potential then the sum of the resulting fragment densities is equal to the exact molecular density at all times. The uniqueness of this time-dependent partition potential is shown in Ref. [63] using a proof analogous to the Runge-Gross theorem.

5.1.1 The Direct and Inverse Problems

In a P-TDDFT calculation the initial states resulting from a PDFT calculation are propagated *independently* in time via the time-dependent Kohn-Sham fragment equations,

$$\imath\frac{\partial}{\partial t}\phi_{i,\alpha}(\mathbf{r},t) = \left[-\frac{\Delta}{2} + v_{\mathrm{KS},\alpha}(\mathbf{r},t)\right]\phi_{i,\alpha}(\mathbf{r},t)\,, \tag{5.1}$$

where the fragment TDKS potentials are

$$v_{\mathrm{KS},\alpha}(\mathbf{r},t) = v_{\mathrm{xc},\alpha}(\mathbf{r},t) + v_{\mathrm{H}}(\mathbf{r},t) + v_{\alpha}(\mathbf{r},t) + v_{\mathrm{p}}(\mathbf{r},t)\,. \tag{5.2}$$

In practice the time-dependent partition potential $v_{\mathrm{p}}(\mathbf{r},t)$ must be approximated for nontrivial systems. The molecular density is then given by

$$n(\mathbf{r},t)=\sum_{\alpha}n_{\alpha}(\mathbf{r},t)=\sum_{i,\alpha}f_{i,\alpha}\left|\phi_{i,\alpha}(\mathbf{r},t)\right|^{2}. \tag{5.3}$$

The occupation numbers $f_{i,\alpha}$ are constant in time because the Hamiltonians

$$\hat{H}_{\alpha}(t)=\hat{T}+\hat{V}_{\mathrm{ee}}+\int \mathrm{d}^{3}\mathbf{r}\left[v_{\alpha}(\mathbf{r},t)+v_{\mathrm{p}}(\mathbf{r},t)\right]\hat{n}(\mathbf{r}) \tag{5.4}$$

are particle conserving.

The direct and inverse problems of P-TDDFT are similar to the PDFT problems described in Sec. 3.1.1. The partition potential is usually approximated in the direct problem and is the main unknown in the inverse problem. The exchange-correlation potential is also unknown similar to the inverse PDFT problem but the occupation numbers are not allowed to vary as they do in a PDFT inversion.

5.2 Inversion Algorithms

Our first P-TDDFT inversion method uses a step-wise optimization procedure to find the time-dependent partition potential $v_{\mathrm{p}}(\mathbf{r},t)$ given a target density $\tilde{n}(\mathbf{r},t)$, target current density $\tilde{\mathbf{j}}(\mathbf{r},t)$, and set of fragment potentials $\{v_{\alpha}(\mathbf{r},t)\}$. The density and current density of the total system are found at each time step using the Crank-Nicolson propagator with a second-order discretization of the Laplacian. (Other propagation methods may also be used.) A guess is made for the partition potential at the next unknown time and the fragment wave functions are propagated forward in time using this guess. (For small time steps the value of the partition potential at the previous time step works well.) The fragment densities $(\{n_{\alpha}\},\{j_{\alpha}\})$ are found using these fragment wave functions and added together to form an approximation to the total densities $(n,\, j)$. The errors $n_{\mathrm{err}}=n-\tilde{n}$ and $j_{\mathrm{err}}=j-\tilde{j}$ are computed and the residual norm $(n_{\mathrm{err}}/n_{\mathrm{exact}})+\mathrm{norm}\,(j_{\mathrm{err}}/j_{\mathrm{exact}})$ is used in the optimizer of Ref. [79],

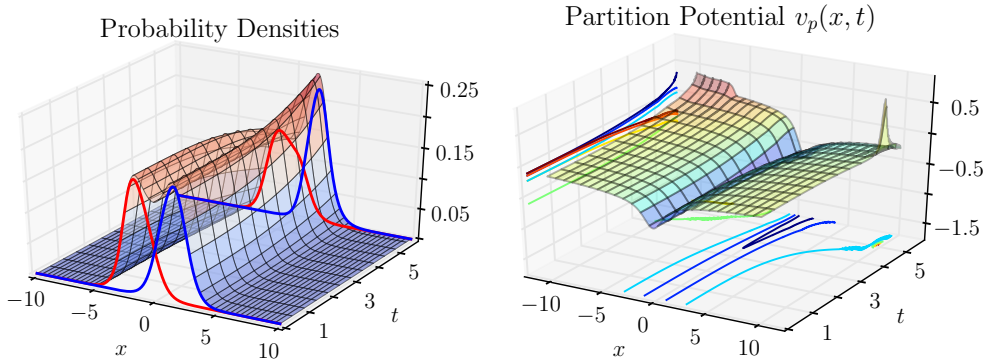

Figure 5.1. The fragment densities at times $t = 0$ and $t \approx T/4$, (T is the period of the laser pulse), along with the molecular density of a one-dimensional model of an electron in a laser field (left). The partition potential $v_{\mathrm{p}}(x,t)$ during this time period (right).

with the L^2 norm. The division by n_{exact} and j_{exact} weights the error in the asymptotic regions to help increase the convergence rate, similar to the weighting used in [80].

Figure 5.1 shows the results of a P-TDDFT calculation for the one-dimensional model of an electron in a laser field described in Sec. 4.4.4 but using the algorithm described above. The resulting fragment densities and potentials are shown in Fig. 5.1. Figure 5.2 shows the results of using a frozen and instantaneous approximate partition potential with the frozen approximation outperforming the instantaneous approximation. On this particular inversion problem, the algorithm described above is unstable at times greater than 6 and produces a divergent partition potential at those times. This instability arises from large relative errors in the asymptotic regions as described in Sec. A.2. The partial differential equation (PDE) constrained inversion method described in Sec. 4.3.1 is stable at all times and can be used to find the partition potential at later times as seen in Figs. 4.7 and 4.8.

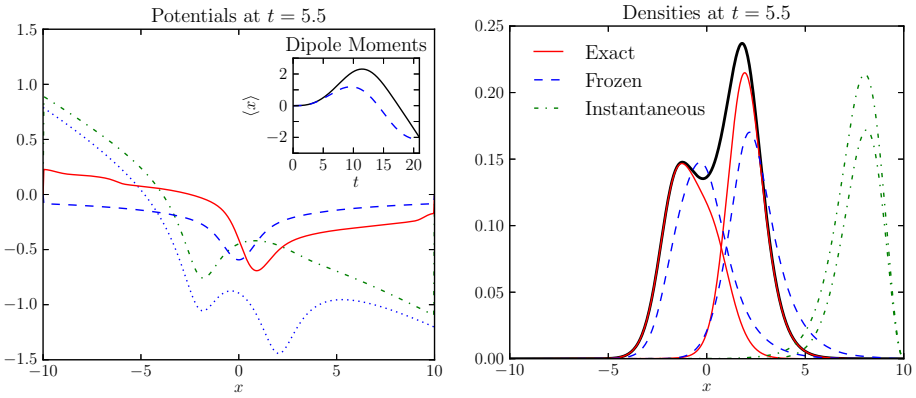

Figure 5.2. The fragment densities (left) and corresponding potentials (right) using the exact, frozen, and instantaneous partition potentials at $t \approx T/4$.

6. Summary

We have presented a series of algorithms for performing density-to-potential inversions in density functional theory (DFT), partition density functional theory (PDFT), time-dependent density functional theory (TDDFT), and partition time-dependent density functional theory (P-TDDFT). These algorithms have favorable scaling properties and permit large-scale inversions. Although the examples in this work are all one-dimensional model systems, the algorithms are written in multiple dimensions to help transition to more realistic systems in the future. We have also presented a detailed numerical analysis that points to the relative error as the main limitation in density-to-potential inversions and the need for error estimates in performing these inversions properly.

Due to the somewhat separate development of the time-independent (Chs. 2-3) and time-dependent (Chs. 4-5) inversion algorithms, some features are missing in the time-independent schemes while present in the time-dependent schemes and vice versa. In particular, the multilevel idea used in Ch. 4 is not yet implemented in the time-independent inversion algorithms and is likely to dramatically reduce the execution time as it does in time-dependent inversions. Likewise, the orbital scaling introduced in Sec. 2.3.4 for DFT inversions is likely needed to recover the asymptotic potentials in time-dependent inversions. It also remains to be seen if the constrained variational method described in Sec. 2.3.4 can be adapted for time-dependent density-to-potential inversions.

The inversion methods presented in this work use the finite difference method for solving the governing partial differential equations (PDEs) but are by no means restricted to this solution method. We would also like to apply these methods to the common basis function methods described in Ref. 6 (Pgs. 233-234). The insight we have gained through our many test cases and numerical analysis with the finite

difference method will likely guide this development. This insight can also be used to improve other inversion methods as hinted at in Sec. 2.4.1. In particular, the scaled-orbital regularization presented in Sec. 2.3.4 is perhaps a more natural regularization than the potential regularization presented in Ref. [36] for improving the Wu-Yang algorithm. This regularization should also make it possible to examine more realistic examples including possibly ill-posed densities from experimental data.

Our original intent in developing inversion algorithms was to benchmark approximate exchange-correlation approximations and create new approximations within DFT. During this development, however, several new and interesting applications have come to light that warrant further study. For example, by allowing the optimizers to choose boundary conditions for the potential in both the DFT and TDDFT inversions, it should be possible to extract new approximate boundary conditions and compare them to other state-of-the-art methods. [67] Likewise, the orbital scaling introduced in Sec. 2.3.3 could be modified for the direct DFT problem as an alternative to using adaptive grid methods. [19] Thanks to the very similar structure between the optimized effective potential (OEP) method and the DFT inverse problem, algorithm development in one area can lead directly to improvements in the other as seen in the development of the Wu-Yang inversion algorithm from a previous OEP optimization method. [17] Similarly, the TDDFT version of quantum optimal control theory (QOCT) [68] has a very similar structure to the TDDFT inverse problem and can likely benefit mutually from new developments in our TDDFT inversion methods. We plan to continue exploring these new areas of DFT and refine the density-to-potential inversion methods described in this work.

LIST OF REFERENCES

LIST OF REFERENCES

[1] Daniel Jensen. Real-Space Approach to Time Dependent Current Density Functional Theory. Master's thesis, Brigham Young University - Provo, July 2010.

[2] Jos Thijssen. *Computational Physics*. Cambridge University Press, Cambridge, UK ; New York, 2 edition edition, April 2007.

[3] Wolfram Koch and Max C. Holthausen. *A Chemist's Guide to Density Functional Theory, 2nd Edition*. Wiley-VCH, 2 edition, July 2001.

[4] Eugene Merzbacher. *Quantum Mechanics 3ed*. JOHN WILEY & SONS@, New York, 3rd edition edition, 1998.

[5] Claude Le Bris. Computational chemistry from the perspective of numerical analysis. *Acta Numerica*, 14:363–444, May 2005.

[6] Richard M. Martin. *Electronic Structure: Basic Theory and Practical Methods*. Cambridge University Press, Cambridge, UK ; New York, April 2004.

[7] P. Hohenberg and W. Kohn. Inhomogeneous Electron Gas. *Physical Review*, 136(3B):B864–B871, November 1964.

[8] W. Kohn and L. J. Sham. Self-Consistent Equations Including Exchange and Correlation Effects. *Physical Review*, 140(4A):A1133–A1138, November 1965.

[9] J. T. Chayes, L. Chayes, and Mary Beth Ruskai. Density functional approach to quantum lattice systems. *Journal of Statistical Physics*, 38(3-4):497–518, February 1985.

[10] Kieron Burke. Perspective on density functional theory. *The Journal of Chemical Physics*, 136(15):150901, 2012.

[11] Miguel A. L. Marques, Micael J. T. Oliveira, and Tobias Burnus. Libxc: A library of exchange and correlation functionals for density functional theory. *Computer Physics Communications*, 183(10):2272–2281, October 2012.

[12] Andreas Kirsch. *An Introduction to the Mathematical Theory of Inverse Problems*. Springer, New York, 2nd ed. 2011 edition edition, April 2011.

[13] Jacques Hadamard. Sur les problèmes aux dérivés partielles et leur signification physique. *Princeton University Bulletin*, 13:49–52, 1902.

[14] Curtis R Vogel. *Computational methods for inverse problems*. Society for Industrial and Applied Mathematics, Philadelphia, 2002.

[15] Richard C Aster and Clifford H Thurber. *Parameter estimation and inverse problems*. Academic Press, Waltham, MA, 2012.

[16] Jennifer Siltanen Samuli Mueller. *Linear and nonlinear inverse problems with practical applications*. 2012.

[17] Qin Wu and Weitao Yang. A direct optimization method for calculating density functionals and exchange–correlation potentials from electron densities. *The Journal of Chemical Physics*, 118(6):2498–2509, February 2003.

[18] Xavier Andrade, David Strubbe, Umberto De Giovannini, Ask Hjorth Larsen, Micael J. T. Oliveira, Joseba Alberdi-Rodriguez, Alejandro Varas, Iris Theophilou, Nicole Helbig, Matthieu J. Verstraete, Lorenzo Stella, Fernando Nogueira, Alán Aspuru-Guzik, Alberto Castro, Miguel A. L. Marques, and Angel Rubio. Real-space grids and the Octopus code as tools for the development of new simulation approaches for electronic systems. *Physical Chemistry Chemical Physics*, 17(47):31371–31396, November 2015.

[19] Alberto Castro, Heiko Appel, Micael Oliveira, Carlo A. Rozzi, Xavier Andrade, Florian Lorenzen, M. a. L. Marques, E. K. U. Gross, and Angel Rubio. octopus: a tool for the application of time-dependent density functional theory. *physica status solidi (b)*, 243(11):2465–2488, September 2006.

[20] Thomas L. Beck. Real-space mesh techniques in density-functional theory. *Reviews of Modern Physics*, 72(4):1041–1080, October 2000.

[21] Bengt Fornberg. Generation of finite difference formulas on arbitrarily spaced grids. *Mathematics of Computation*, 51(184):699–706, 1988.

[22] P. Maragakis, José Soler, and Efthimios Kaxiras. Variational finite-difference representation of the kinetic energy operator. *Physical Review B*, 64(19):193101, October 2001.

[23] Pablo García-Risueño, Joseba Alberdi-Rodriguez, Micael J. T. Oliveira, Xavier Andrade, Michael Pippig, Javier Muguerza, Agustin Arruabarrena, and Angel Rubio. A survey of the parallel performance and accuracy of Poisson solvers for electronic structure calculations. *Journal of Computational Chemistry*, 35(6):427–444, March 2014.

[24] Thomas E. Baker, E. Miles Stoudenmire, Lucas O. Wagner, Kieron Burke, and Steven R. White. One-dimensional mimicking of electronic structure: The case for exponentials. *Physical Review B*, 91(23):235141, June 2015.

[25] Lucas O. Wagner, E. M. Stoudenmire, Kieron Burke, and Steven R. White. Reference electronic structure calculations in one dimension. *Physical Chemistry Chemical Physics*, 14(24):8581–8590, May 2012.

[26] Eric Jones, Travis Oliphant, Pearu Peterson, et al. SciPy: Open source scientific tools for Python (Version 0.14.1).

[27] P. Pulay. Improved SCF convergence acceleration. *Journal of Computational Chemistry*, 3(4):556–560, 1982.

[28] Ilya G. Ryabinkin and Viktor N. Staroverov. Determination of Kohn–Sham effective potentials from electron densities using the differential virial theorem. *The Journal of Chemical Physics*, 137(16):164113–164113–8, October 2012.

[29] Lee J. Bain and Max Engelhardt. *Introduction to Probability and Mathematical Statistics*. Cengage Learning, Boston, 2 edition edition, March 2000.

[30] Neepa T. Maitra and Kieron Burke. Demonstration of initial-state dependence in time-dependent density-functional theory. *Physical Review A*, 63(4):042501, March 2001.

[31] François Ladouceur. Boundaryless beam propagation. *Optics Letters*, 21(1):4–5, January 1996.

[32] R. van Leeuwen and E. J. Baerends. Exchange-correlation potential with correct asymptotic behavior. *Physical Review A*, 49(4):2421–2431, April 1994.

[33] Lucas O. Wagner, Thomas E. Baker, E. M. Stoudenmire, Kieron Burke, and Steven R. White. Kohn-Sham calculations with the exact functional. *Physical Review B*, 90(4):045109, July 2014.

[34] Jonathan Nafziger and Adam Wasserman. Fragment-based treatment of delocalization and static correlation errors in density-functional theory. *The Journal of Chemical Physics*, 143(23):234105, December 2015.

[35] Weitao Yang and Qin Wu. Direct Method for Optimized Effective Potentials in Density-Functional Theory. *Physical Review Letters*, 89(14):143002, September 2002.

[36] Felipe A. Bulat, Tim Heaton-Burgess, Aron J. Cohen, and Weitao Yang. Optimized effective potentials from electron densities in finite basis sets. *The Journal of Chemical Physics*, 127(17):174101–174101–9, November 2007.

[37] Lorenz T. Biegler, Omar Ghattas, Matthias Heinkenschloss, and Bart van Bloemen Waanders. Large-Scale PDE-Constrained Optimization: An Introduction. In Lorenz T. Biegler, Matthias Heinkenschloss, Omar Ghattas, and Bart van Bloemen Waanders, editors, *Large-Scale PDE-Constrained Optimization*, number 30 in Lecture Notes in Computational Science and Engineering, pages 3–13. Springer Berlin Heidelberg, January 2003.

[38] J. E. Hicken and D. W. Zingg. Dual consistency and functional accuracy: a finite-difference perspective. *Journal of Computational Physics*, 256:161–182, January 2014.

[39] S. Nash. Newton-Type Minimization via the Lanczos Method. *SIAM Journal on Numerical Analysis*, 21(4):770–788, August 1984.

[40] Robert G. Parr and Yang Weitao. *Density-Functional Theory of Atoms and Molecules*. Oxford University Press, USA, May 1994.

[41] Andreas Wächter and Lorenz T. Biegler. On the implementation of an interior-point filter line-search algorithm for large-scale nonlinear programming. *Mathematical Programming*, 106(1):25–57, April 2005.

[42] David G. Tempel, Todd J. Martínez, and Neepa T. Maitra. Revisiting Molecular Dissociation in Density Functional Theory: A Simple Model. *Journal of Chemical Theory and Computation*, 5(4):770–780, April 2009.

[43] Peter Elliott, Daniel Jensen, Adam Wasserman, and Kieron Burke. Comment on "Application of partition density-functional theory to one-dimensional models". *Physical Review A*, 89(2):026501, February 2014.

[44] Jonathan Nafziger and Adam Wasserman. Density-Based Partitioning Methods for Ground-State Molecular Calculations. *The Journal of Physical Chemistry A*, 118(36):7623–7639, September 2014.

[45] Morrel Cohen and Adam Wasserman. On Hardness and Electronegativity Equalization in Chemical Reactivity Theory. *Journal of Statistical Physics*, 125(5):1121–1139, 2006.

[46] Peter Elliott, Kieron Burke, Morrel H. Cohen, and Adam Wasserman. Partition density-functional theory. *Physical Review A*, 82(2):024501, 2010.

[47] John P. Perdew, Robert G. Parr, Mel Levy, and Jose L. Balduz. Density-Functional Theory for Fractional Particle Number: Derivative Discontinuities of the Energy. *Physical Review Letters*, 49(23):1691–1694, December 1982.

[48] Morrel H. Cohen and Adam Wasserman. On the Foundations of Chemical Reactivity Theory. *J. Phys. Chem. A*, 111(11):2229–2242, 2007.

[49] Jonathan Nafziger. *Partition density functional theory*. PhD thesis, Purdue University, 2015.

[50] Jonathan Nafziger, Qin Wu, and Adam Wasserman. Molecular binding energies from partition density functional theory. *The Journal of Chemical Physics*, 135(23):234101, December 2011.

[51] Daniel S. Jensen and Adam Wasserman. Numerical density-to-potential inversions in time-dependent density functional theory. *Physical Chemistry Chemical Physics*, March 2016.

[52] Erich Runge and E. K. U. Gross. Density-Functional Theory for Time-Dependent Systems. *Physical Review Letters*, 52(12):997–1000, March 1984.

[53] M. Farzanehpour and I. V. Tokatly. Time-dependent density functional theory on a lattice. *Physical Review B*, 86(12):125130, September 2012.

[54] Johanna I. Fuks and Neepa T. Maitra. Challenging adiabatic time-dependent density functional theory with a Hubbard dimer: the case of time-resolved long-range charge transfer. *Physical Chemistry Chemical Physics*, 16(28):14504–14513, June 2014.

[55] Miguel A.L. Marques, Carsten A. Ullrich, Fernando Nogueira, Angel Rubio, Kieron Burke, and Eberhard K. U. Gross, editors. *Time-Dependent Density Functional Theory*. Lecture Notes in Physics. 2006. DOI: 10.1007/b11767107.

[56] Alberto Castro, Miguel A. L. Marques, and Angel Rubio. Propagators for the time-dependent Kohn–Sham equations. *The Journal of Chemical Physics*, 121(8):3425, August 2004.

[57] P. Elliott, J. I. Fuks, A. Rubio, and N. T. Maitra. Universal Dynamical Steps in the Exact Time-Dependent Exchange-Correlation Potential. *Physical Review Letters*, 109(26):266404, December 2012.

[58] M. J. P. Hodgson, J. D. Ramsden, J. B. J. Chapman, P. Lillystone, and R. W. Godby. Exact time-dependent density-functional potentials for strongly correlated tunneling electrons. *Physical Review B*, 88(24):241102, December 2013.

[59] S. E. B. Nielsen, M. Ruggenthaler, and R. van Leeuwen. Many-body quantum dynamics from the density. *EPL (Europhysics Letters)*, 101(3):33001, February 2013.

[60] Roi Baer. On the mapping of time-dependent densities onto potentials in quantum mechanics. *The Journal of Chemical Physics*, 128(4):044103–044103–4, January 2008.

[61] Yonghui Li and C. A. Ullrich. Time-dependent V-representability on lattice systems. *The Journal of Chemical Physics*, 129(4):044105–044105–8, July 2008.

[62] Giovanni Vignale. Mapping from current densities to vector potentials in time-dependent current density functional theory. *Physical Review B*, 70(20):201102, November 2004.

[63] Martín A. Mosquera, Daniel Jensen, and Adam Wasserman. Fragment-Based Time-Dependent Density Functional Theory. *Physical Review Letters*, 111(2):023001, July 2013.

[64] Paul Hessler, Neepa T. Maitra, and Kieron Burke. Correlation in time-dependent density-functional theory. *The Journal of Chemical Physics*, 117(1):72–81, July 2002.

[65] Manfred Lein and Stephan Kümmel. Exact Time-Dependent Exchange-Correlation Potentials for Strong-Field Electron Dynamics. *Physical Review Letters*, 94(14):143003, April 2005.

[66] Michael Ruggenthaler, Markus Penz, and Robert van Leeuwen. Existence, uniqueness, and construction of the density-potential mapping in time-dependent density-functional theory. *Journal of Physics: Condensed Matter*, 27(20):203202, May 2015.

[67] Xavier Antoine, Anton Arnold, Christophe Besse, Matthias Ehrhardt, and Achim Schädle. A Review of Transparent and Artificial Boundary Conditions Techniques for Linear and Nonlinear Schrödinger Equations. *Communications in Computational Physics*, 4(4):729–796, 2008.

[68] A. Castro, J. Werschnik, and E. K. U. Gross. Controlling the Dynamics of Many-Electron Systems from First Principles: A Combination of Optimal Control and Time-Dependent Density-Functional Theory. *Physical Review Letters*, 109(15):153603, October 2012.

[69] A. Auger, A. Ben Haj Yedder, E. Cances, C. Le Bris, C. M. Dion, A. Keller, and O. Atabek. Optimal laser control of molecular systems: Methodology and results. *Mathematical Models and Methods in Applied Sciences*, 12(09):1281–1315, 2002.

[70] Gregory von Winckel. *Computational Techniques for Optimal Control of Quantum System*. PhD thesis, University of New Mexico, December 2011.

[71] Neepa T. Maitra, Ivo Souza, and Kieron Burke. Current-density functional theory of the response of solids. *Physical Review B*, 68(4):045109, July 2003.

[72] Jorge Nocedal and Stephen J Wright. *Numerical optimization*. Springer, New York, 2006.

[73] Michael B. Giles and Niles A. Pierce. An Introduction to the Adjoint Approach to Design. *Flow, Turbulence and Combustion*, 65(3-4):393–415, December 2000.

[74] J. J. Alonso J. E. Hicken. PDE-constrained optimization with error estimation and control. *Journal of Computational Physics*, 263:136–150, 2014.

[75] G. G. Balint-Kurti and Á Vibók. Complex Absorbing Potentials in Time Dependent Quantum Dynamics. In Charles Cerjan, editor, *Numerical Grid Methods and Their Application to Schrödinger's Equation*, number 412 in NATO ASI Series, pages 195–205. Springer Netherlands, 1993. DOI: 10.1007/978-94-015-8240-7_11.

[76] K. Burke. Exact Conditions. In Miguel A. L. Marques, Carsten A. Ullrich, Fernando Nogueira, Angel Rubio, Kieron Burke, and Eberhard K. U. Gross, editors, *Time-Dependent Density Functional Theory*, number 706 in Lecture Notes in Physics, pages 181–194. Springer Berlin Heidelberg, 2006. DOI: 10.1007/3-540-35426-3_11.

[77] Q. Wang, P. Moin, and G. Iaccarino. Minimal Repetition Dynamic Checkpointing Algorithm for Unsteady Adjoint Calculation. *SIAM Journal on Scientific Computing*, 31(4):2549–2567, January 2009.

[78] John F. Dobson. Harmonic-Potential Theorem: Implications for Approximate Many-Body Theories. *Physical Review Letters*, 73(16):2244–2247, October 1994.

[79] José Luis Morales and Jorge Nocedal. Remark on “algorithm 778: L-BFGS-B: Fortran subroutines for large-scale bound constrained optimization”. *ACM Trans. Math. Softw.*, 38(1):7:1–7:4, December 2011.

[80] K. Peirs, D. Van Neck, and M. Waroquier. Algorithm to derive exact exchange-correlation potentials from correlated densities in atoms. *Physical Review A*, 67(1):012505, January 2003.

[81] M. J. D. Powell. An efficient method for finding the minimum of a function of several variables without calculating derivatives. *The Computer Journal*, 7(2):155–162, January 1964.

[82] CARL S. RUDISILL and YEE-YEEN CHU. Numerical Methods for Evaluating the Derivatives of Eigenvalues and Eigenvectors. *AIAA Journal*, 13(6):834–837, 1975.

[83] N. van der Aa, H. ter Morsche, and R. Mattheij. Computation of eigenvalue and eigenvector derivatives for a general complex-valued eigensystem. *Electronic Journal of Linear Algebra*, 16(1), January 2007.

APPENDICES

A. Numerical Issues

This appendix contains a discussion of several numerical issues that arise in performing density-to-potential inversions. The description of each numerical issue is accompanied by an example to better illustrate its difficulty and importance. We treat the time-independent and time-dependent inversions separately although some of the time-independent numerical issues also apply to the time-dependent case.

A.1 Time-Independent Inversions

A number of numerical problems arise in performing time-independent density-to-potential inversions that are often very difficult to isolate. In this section we use very basic one-dimensional models to show how boundary conditions, relative error, and rounding errors all set convergence limits on density-to-potential inversions. We employ the one-orbital formula shown in Eq. (2.7) and a grid ranging from -4 to 4 with 51 points in the examples of this section unless otherwise noted.

Many of the inversion schemes mentioned in Sec. 2.3 impose boundary conditions on the orbitals that don't have to agree with the target density's boundary conditions. A mismatch in boundary conditions can place severe constraints on the accuracy of density-to-potential inversions in the boundary regions as we illustrate here with an example. For simplicity, we take the density of the ground state of the simple harmonic oscillator and set it to zero at the edge of our simulation box as typically occurs with box-type (Dirichlet) boundary conditions. The one-orbital formula should give us the exact potential for this problem but for this modified density the potential is not recovered properly near the boundaries. The number of incorrect points near the boundaries increases as higher-order finite difference schemes are used to represent

the Laplacian due to the increased nonlocality of the finite difference operators. The adverse effects of these mismatched boundary conditions are illustrated in Fig. A.1.

One common method for avoiding the mismatch in boundary conditions described above is to compute the target density with the same boundary conditions and a very similar numerical method. In Fig. A.2 we compute the ground state density of the harmonic oscillator numerically with box-type boundary conditions and a second-order finite difference approximation to the Laplacian as explained in Sec. 2.2. If the same finite difference approximation is used in the one-orbital formula then the resulting potential is almost exact everywhere. This type of inversion is known as an inverse crime and is explained in more detail in Sec. 1.5. It is a very fragile method as a simple change to a fourth-order approximate Laplacian with the same box-type boundary conditions does not have the same error cancellation and produces worse values than the second-order method.

Both of the preceding examples assume a perfect knowledge of the target density but this is not a realistic assumption for most inverse problems. The wave function numerical methods used in computing interacting densities are often very different from density functional theory (DFT) numerical methods [24] and the correct boundary conditions are not always known beforehand. It is far more realistic to assume that the target density in a density-to-potential inversion has some numerical error that must be accounted for to avoid overfitting. In order to illustrate the effects of numerical noise in the target density, we take the ground state orbital of the simple harmonic oscillator, add in a small amount of noise generated from the standard normal distribution $\mathrm{N}(\mu, \sigma^2)$, [29] and put the density corresponding to this modified orbital in the one-orbital formula. The results of this inversion in Fig. A.3 are very poor especially in the asymptotic region. If we add a relative error to the ground state orbital instead of the uniform error described above then the resulting potential is still noisy but the noise level is now the same everywhere as seen in Fig. A.4. These two examples show that the relative error of the target density sets a limit on the convergence in density-to-potential inversions. Figure A.5 shows that simply increas-

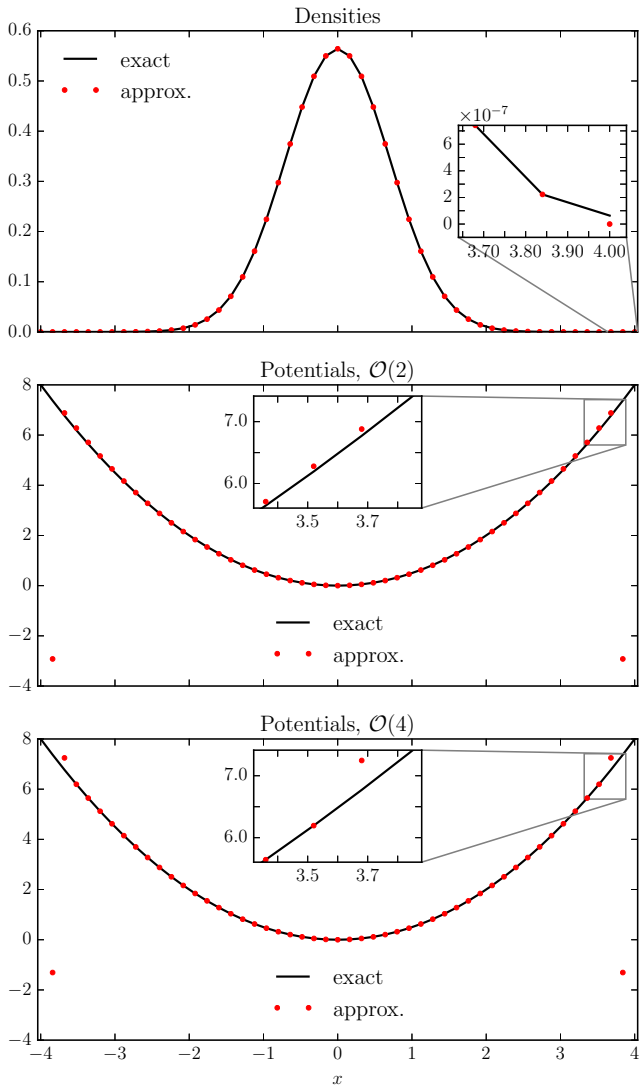

Figure A.1. The degradation of a density-to-potential inversion when forcing incorrect boundary conditions on the orbitals. The ground-state density of the simple harmonic oscillator is modified to be exactly zero at the boundaries as commonly occurs when box-type (Dirichlet) boundary conditions are enforced (top). The potentials produced from this density with the one-orbital inversion formula and a second-order discretization of the Laplacian are incorrect near the boundaries (middle). More points are incorrect when a fourth-order approximation to the Laplacian is used in the one-orbital formula (bottom).

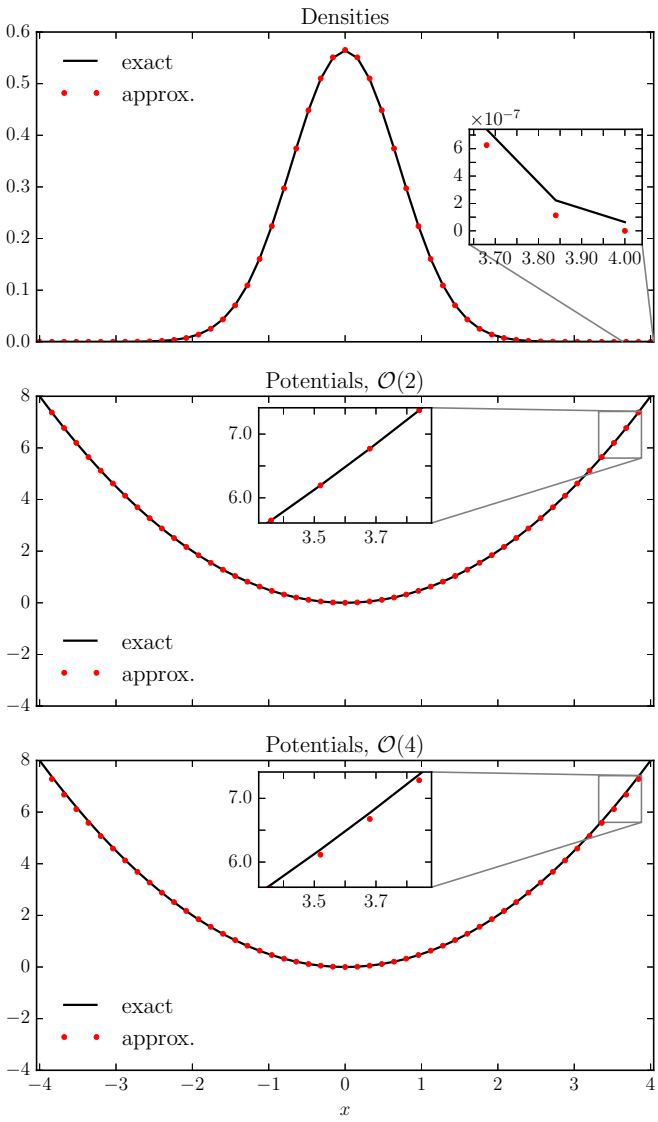

Figure A.2. The frailty of inverse crimes in a density-to-potential inversion. The ground state density of the harmonic oscillator is computed numerically using a second-order approximation to the Laplacian (top). Applying the one-orbital formula to this density with a second-order approximate Laplacian produces nearly the exact potential (middle) and is an inverse crime. A fourth-order approximation in the one-orbital formula actually gives worse values most noticeable near the boundaries (bottom).

ing the number of grid points actually makes the inverted potential worse when the same amount of error is present in the target density.

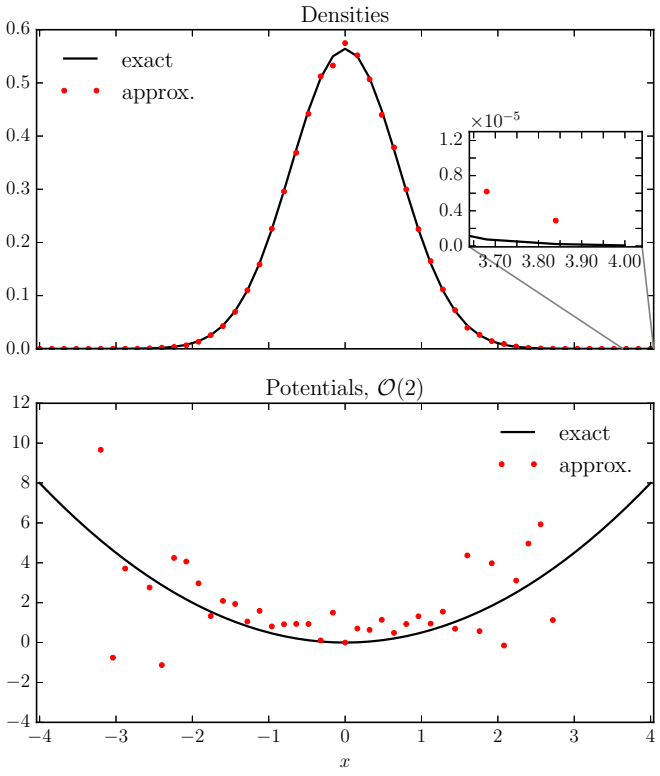

Figure A.3. The effects of random noise in a density-to-potential inversion. When the ground-state of the simple harmonic oscillator contains noise, (i.e. $\tilde{n}_0 = [\phi_0 + N(\mu = 0, \sigma^2 = 2.5 \times 10^{-5})]^2$), the resulting potential is very noisy everywhere but especially in the asymptotic region.

As mentioned in the previous examples, higher-order finite difference operators don't always improve density-to-potential inversions and boundary conditions often have a dramatic impact on the quality of an inversion. Another way to study the delicate balance between finite difference operators and boundary conditions is to use the ground state density of a particle in a box in the one-orbital formula. If we compute the derivative in Eq. (2.7) with one finite difference operator on the left side of the simulation box and a different operator on the right then the resulting second

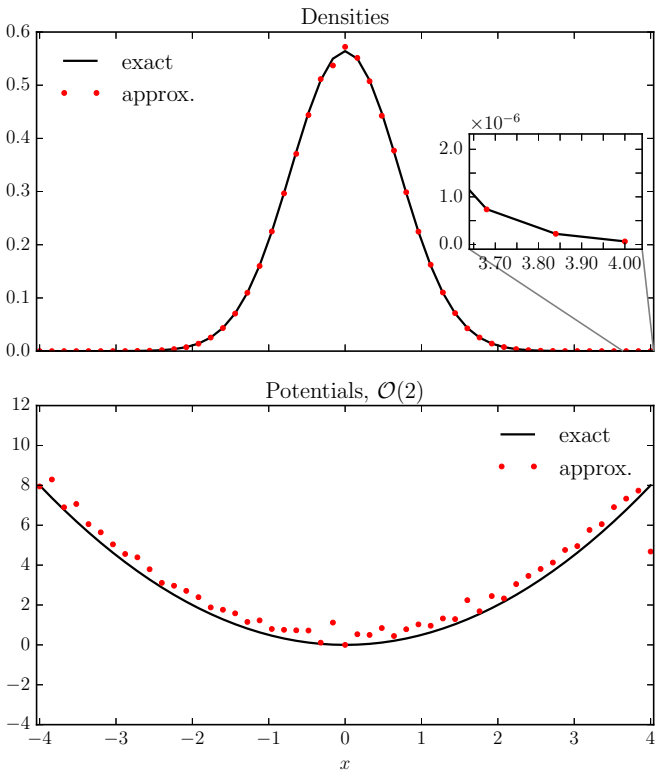

Figure A.4. The effects of weighted random noise in a density-to-potential inversion. When the ground-state of the simple harmonic oscillator contains noise weighted by the orbital, (i.e. $\tilde{n}_0 = \{\phi_0 [1 + N(\mu = 0, \sigma^2 = 2.5 \times 10^{-5})]\}^2$), the resulting potential is uniformly noisy. This indicates that the relative error in the target density sets a convergence limit in density-to-potential inversions.

derivative has different error patterns on both sides of the box. The resulting potential has a jump between the left and right sides of the box as seen in Fig. A.6. Although one usually doesn't mix finite difference operators inside the simulation box, different operators are often used at the boundaries and produce similar jumps even if the operators are the same order of accuracy. An example of this jump at the boundary can be seen in Fig. A.6 at the right boundary where a fourth-order backwards finite-difference operator produces a different error pattern than the fourth-order centered operator used elsewhere. (See Eq. (2.4) for the matrix representation of this fourth-order finite-difference operator.)

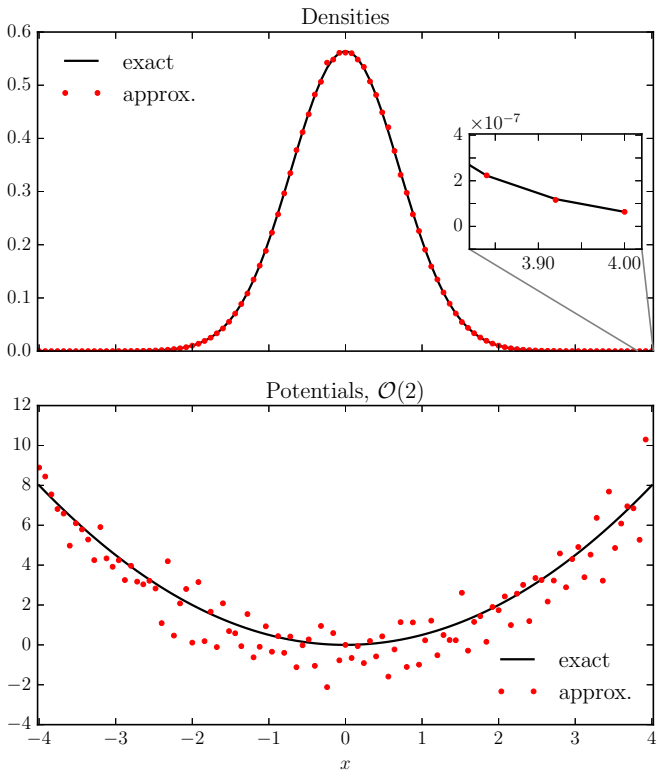

Figure A.5. The effects of weighted random noise and increased grid resolution in a density-to-potential inversion. When twice the number of grid points are used in the example displayed in Fig. A.4 the resulting potential is actually worse and shows that increased resolution does not necessarily improve density-to-potential inversions.

Many of the somewhat counterintuitive behaviors shown in the preceding examples can be understood mathematically by studying the effects of errors in the one-orbital formula. If we have the exact density of a one orbital system then the potential is given by the formula

$$v_i = \frac{\phi_i'' + \varepsilon_i^{\mathrm{fd}}}{2\phi_i}, \tag{A.1}$$

where $\phi_i = \sqrt{n_i}$ and $\varepsilon_i^{\mathrm{fd}}$ is the error of the approximate second derivative at the point x_i. In the example shown in Fig. A.6 there are different error patterns $\varepsilon_i^{\mathrm{fd}}$ for the left- and right-hand sides of the box and this difference is magnified during the inversion

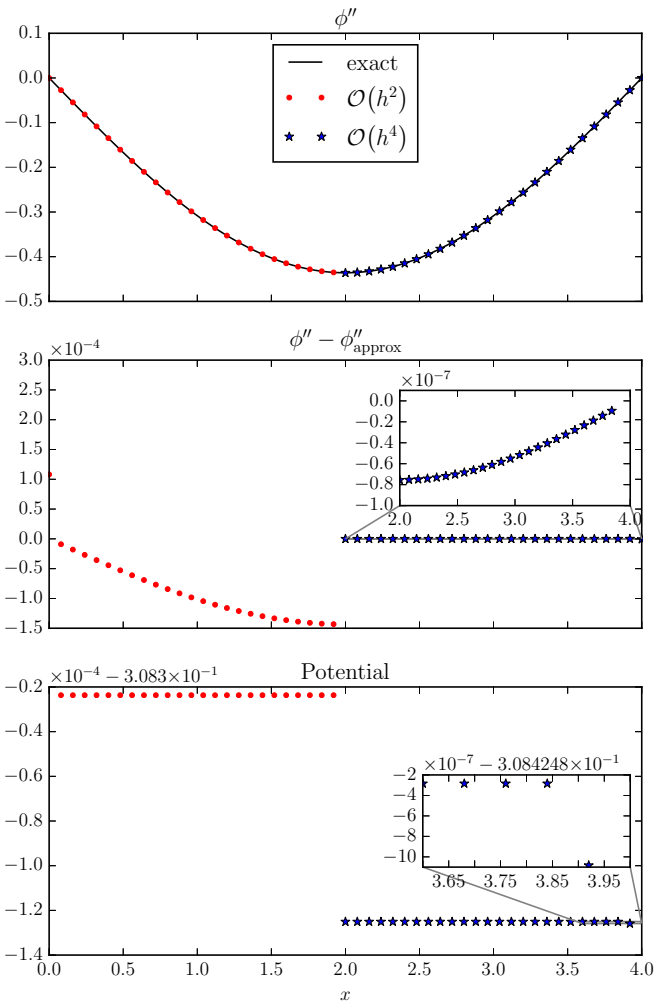

Figure A.6. The effects of combining two different finite difference operators in a density-to-potential inversion. The second derivative is computed with a second-order method on the left side of the box and a fourth-order method on the right (top). The error patterns on both sides of the box are smooth but there is a distinct gap between them (middle). The resulting potential (bottom) also has a gap corresponding to the difference in error patterns and a small gap at the right boundary where a backwards finite-difference operator is used (bottom inset).

because of the division by the square root of the density. A more realistic example

includes some numerical error ε_i^n in the density being inverted and the inversion formula becomes

$$v_i = \frac{(\phi_i + \varepsilon_i^n)''}{2\,(\phi_i + \varepsilon_i^n)} = \frac{\phi_i'' + \varepsilon_i^{\mathrm{fd}} + (\varepsilon_i^n)''}{2\,(\phi_i + \varepsilon_i^n)}. \tag{A.2}$$

If the noise ε_i^n is not smooth then its second derivative will be very noisy and dominate the other terms in Eq. (A.2). Figure A.7 shows an example where a very small normally distributed error severely limits the accuracy of the potential.

Rounding errors play an important role in many of the inversions methods dependent upon numerical optimization methods. The Wu-Yang algorithm discussed in Sec. 2.3 needs to compute the kinetic energy at each iteration of a given numerical optimization routine. If the density of a system decays exponentially then the kinetic energy from the asymptotic regions is very small in comparison to values near the nuclei. Even if the values of the kinetic energy density can be computed accurately in all regions of a simulation, adding all of the values together to get the total kinetic energy will often result in rounding errors due to the large differences in magnitude involved. In Fig. A.8 we apply the Wu-Yang inversion algorithm to the ground-state density of the harmonic oscillator on a grid with 51 points ranging from -8 to 8. Both the gradient-based truncated-Newton (TN) algorithm [39] and the non-gradient-based modified Powell's method [81] fail to resolve the density in the asymptotic region, ($|x| > 5.5$), when used in the Wu-Yang inversion method. The abrupt cutoffs near -5.5 and 5.5 are a result of rounding errors when computing the kinetic energy with double-precision floating point numbers. If we use the midpoint integration rule to compute the kinetic energy in the region $|x| < 5.5$ the result in double precision arithmetic is 0.2500000000000231 and the same method used in the region $|x| > 5.5$ produces the value $-2.32460041955568 \times 10^{-14}$. When the two numbers above are added together, most of the smaller number's significant digits are lost and this loss of information limits the accuracy of the recovered potential in the asymptotic region. The same example performed using single-precision floating point

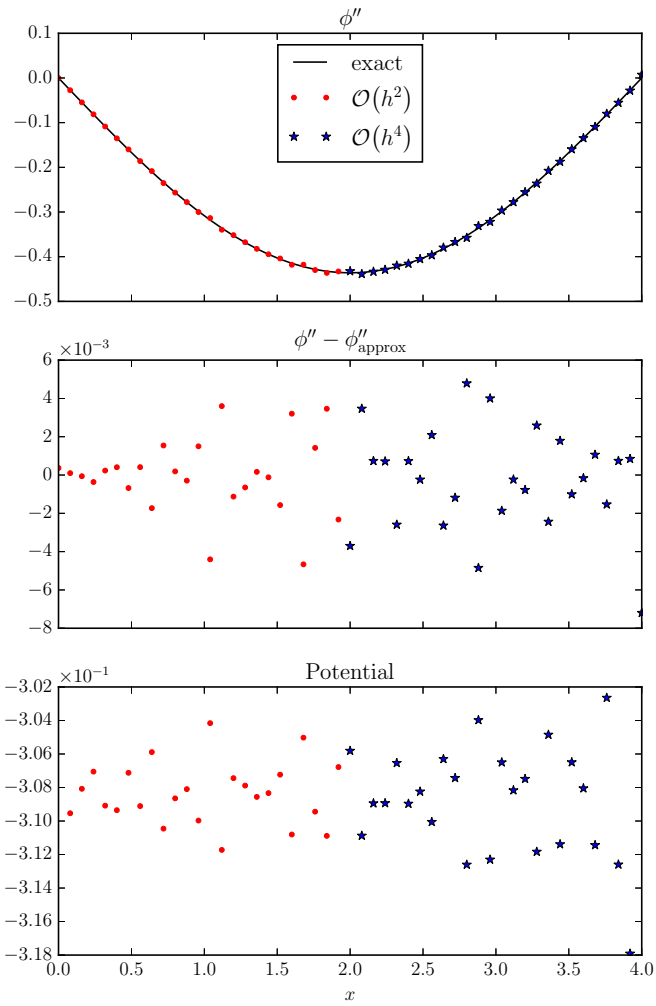

Figure A.7. The effects of combining two different finite difference operators in a density-to-potential inversion with a noisy density. This example is identical to the one shown in Fig. A.6 except the input density contains noise, (i.e. $\tilde{n}_0 = \{\phi_0 [1 + N(\mu = 0, \sigma^2 = 1 \times 10^{-10})]\}^2$). This is another example where higher-order methods can actually produce worse results than simpler lower-order methods.

numbers gives an even stricter cutoff near -3.5 and 3.5 as seen in Fig. A.9. In this second example the kinetic energy in the region $|x| < 3.5$ is 0.25000963 when using single-point precision numbers compared to a value of $-9.6271506e-06$ in the region $|x| > 3.5$, which again results in a loss of significant figures when added together.

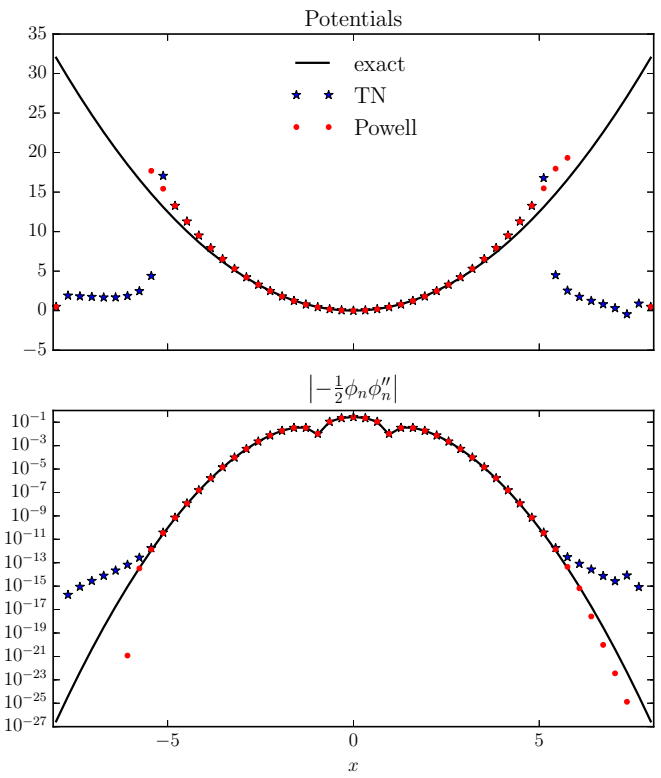

Figure A.8. The effects of rounding errors in a density-to-potential inversion with double-precision numbers. Both the TN and modified Powell's optimizers fail to resolve the potential in the region $|x| > 5.5$ (top) when used in the Wu-Yang algorithm and an initial guess of zero. The kinetic energy density is orders of magnitude smaller in the asymptotic region than it is in the region $|x| < 5.5$ (bottom) and this leads to loss of precision when computing the total kinetic energy.

The preceding examples of time-independent density-to-potential inversions illustrate many of the pitfalls in performing numerical density-to-potential inversions. Simply refining the grid or increasing the accuracy of the kinetic energy operator does not guarantee an improved density-to-potential inversion and in many cases will worsen the solution. In cases where the error pattern is not known explicitly it is actually not correct to fit the density exactly as even small density errors can lead to large artifacts in the potential. Finally, inversions reliant on numerical optimization

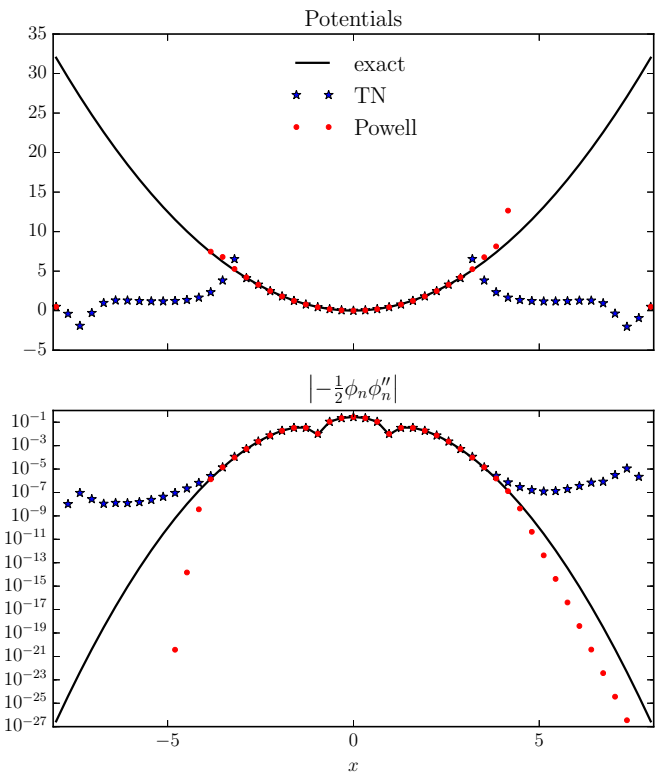

Figure A.9. The effects of rounding errors in a density-to-potential inversion with single-precision numbers. This example is identical to the one shown in Fig. A.8 except that the kinetic energy sum uses single-precision numbers. In this case the potential is only recovered in the region $|x| < 3.5$ due to more severe rounding errors from the use of single-precision numbers.

routines often suffer from rounding errors, which set yet another hard limit on the convergence of density-to-potential inversions.

A.2 Time-Dependent Inversions

In this section we illustrate how the numerical discretization of the time-dependent Kohn-Sham (TDKS) equations affects time-dependent density-to-potential inversion algorithms. We show how spatially constant shifts in the potential change the normalization of the density depending on the propagation scheme. An analogy with

the arbitrary phase in ground-state DFT calculations is made. The sensitivity of the density in the asymptotic regions to different grid spacings is also examined for a model problem.

Theoretically, the potentials in the TDKS equations are only unique up to an arbitrary purely time-dependent function. [52] However, in most numerical implementations a spatially constant shift in time will change the norm of the density. We illustrate this by examining the time development of the ground state of the harmonic oscillator, (Eq. C.6), propagating in the potential $v(x,t) = \alpha\mathcal{H}(t-1) + x^2/2$, where $\mathcal{H}$ is the Heaviside function and the TDKS equations are discretized using the Crank-Nicolson (CN) propagator. In Fig. A.10 we see a 20% loss in density when $\alpha = 100$ and $dt = 0.01$, where dt is the temporal grid spacing. (This result is largely independent of the spatial grid spacing.) The CN method struggles to accurately simulate changes in the potential on the order of the inverse grid spacing $1/dt$. Of course higher-order methods and smaller grid spacings will reduce this loss but the discretization choice still removes some of the potential's nonuniqueness. This situation is similar to the arbitrary phase in the ground-state Kohn-Sham (KS) orbitals being chosen by the numerical solver as illustrated in Fig. A.11.

We now illustrate the sensitivity of the density in the asymptotic region to the discretization of the TDKS equations as mentioned in Sec. 4.2. For this illustration we propagate the ground state of the harmonic oscillator, (Eq. C.6), in the potential given by Eq. 4.13 using the CN propagator and two different discretizations of the Laplacian. (Similar results are obtained by using the same discretization of the Laplacian and varying the number of grid points.) Even though all of the other parameters in the problem are identical, we can clearly see in Fig. A.12 that the relative error in the asymptotic regions is orders of magnitude worse than the central region. This error is largely a result of the particle-in-a-box boundary conditions that we use and indicates a need for better boundary conditions. The error is not very important when performing the forward time-dependent density functional theory (TDDFT) problem but it places serious constraints on the inverse problem. In particular, algorithms

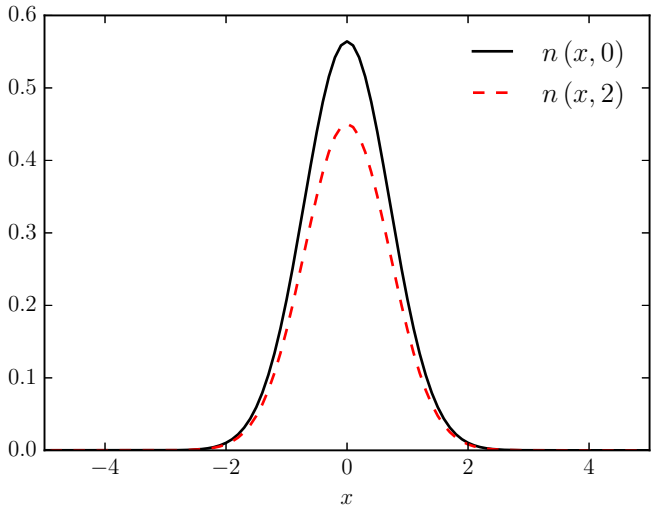

Figure A.10. The large change in density when a spatially constant shift in time is on the same order as the inverse of the temporal grid spacing as explained in App. A.

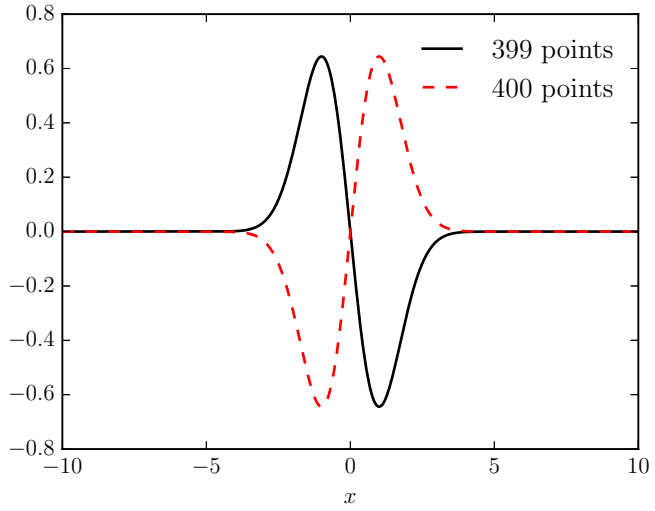

Figure A.11. The arbitrary phase of the ground-state KS orbitals chosen by the `eig_banded` solver in the SciPy libary according to the number of grid points used as mentioned in App. A.

that divide by the density will fail after this relative error has accumulated, (in our example at $t = 5$), unless special precautions are taken.

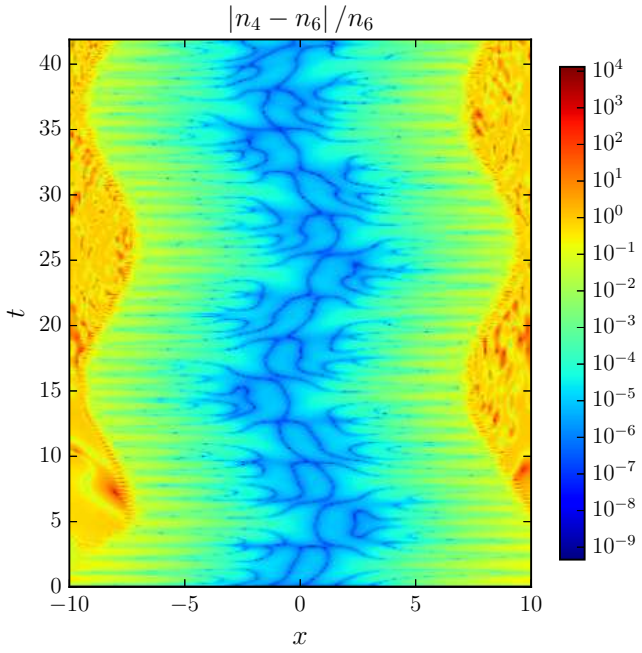

Figure A.12. The sensitivity of the density's relative error in the asymptotic region as explained in App. A. The density n_4 (n_6) uses a fourth-order (sixth-order) approximation to the Laplacian. The relative error in the asymptotic region is relatively small in this example until about $t = 5$.

B. Discrete-Adjoint Method

The discrete-adjoint method is a very efficient method for computing cost functional derivatives (discrete functional derivatives) in constrained-partial differential equation (PDE) problems. [74] The main advantage to using adjoint methods is the ability to accurately compute these derivatives for very large systems at the same or similar cost required to compute the cost functionals. In this appendix we derive the discrete adjoint equations for both time-independent and time-dependent density-to-potential inversions.

Table B.1.
The notation for the discrete-adjoint derivations of Secs. B.1-B.2.

Notation	Description
$\mathbf{i}$	Discrete spatial indices i_x, i_y, i_z
$\sum_{\mathbf{i}=\mathbf{1}}^{N_\mathbf{x}}$	Sum over all spatial indices $\sum_{i_x=1}^{N_x}\sum_{i_y=1}^{N_y}\sum_{i_z=1}^{N_z}$
F_n and $F_\mathbf{j}$	Cost functionals
$\mathcal{L}$	Lagrangian
$\tilde{n}$	The target density
N_orbs	Number of Kohn-Sham orbitals
ϕ^m and χ^m	The m^th orbital and corresponding adjoint orbital
$\underline{\phi}$	All N_orbs orbitals grouped into a vector
$w_{\mathbf{i},n}$	Optional cost-functional weighting
$\square_{,n}$	The vector form of a quantity $\square$ at time step n

B.1 Time-Independent Adjoint

The derivatives of the cost functional used in Sec. 2.3.3 for time-independent density-to-potential inversions can be computed accurately and efficiently using the discrete-adjoint method. In this section we show how these derivatives amount to a sparse linear solve for each occupied orbital. This particular derivation is only valid for

systems without degeneracies because it is based on the algebraic method described in Ref. [82]. A similar derivation can be performed for systems with degeneracies using the method of Ref. [83].

The discretized cost functional

$$F\left[\underline{\phi}\right] = \frac{1}{2}\sum_{\mathbf{i}=\mathbf{1}}^{N_{\mathbf{x}}}\left(\sum_{m=1}^{N_{\text{orbs}}}\phi_{\mathbf{i}}^{m\,*}\phi_{\mathbf{i}}^{m} - \tilde{n}_{\mathbf{i}}\right)^{2} w_{\mathbf{i}} \tag{B.1}$$

can be differentiated with respect to an arbitrary orbital

$$\frac{\partial F}{\partial g_{\boldsymbol{\alpha}}^{\gamma}} = w_{\boldsymbol{\alpha}}\left(\sum_{m=1}^{N_{\text{orbs}}}\phi_{\boldsymbol{\alpha}}^{m\,*}\phi_{\boldsymbol{\alpha}}^{m} - \tilde{n}_{\mathbf{i}}\right)\phi_{\boldsymbol{\alpha}}^{\gamma\,*}, \tag{B.2}$$

where γ is the orbital index, and $\boldsymbol{\alpha} = \alpha_x, \alpha_y, \alpha_z$ is the spatial index. The orbitals are constrained to satisfy the Kohn-Sham (KS) equations and be normalized to one by introducing the Lagrangian

$$\mathcal{L}\left[v, \underline{\phi}, \underline{\chi}\right] = 2\,\mathrm{Re}\left\{\sum_{\mathbf{i}=\mathbf{1}}^{N_{\mathbf{x}}}\sum_{m=1}^{N_{\text{orbs}}}\chi_{\mathbf{i},n}^{m}\left[H\left(v\right)\phi^{m} - E^{m}\phi^{m}\right]_{\boldsymbol{i}}^{*}\right\} + \sum_{m=1}^{N_{\text{orbs}}}\varepsilon^{m}\left(\phi_{i}^{m\,*}\phi_{i}^{m} - 1\right) \tag{B.3}$$

in the total functional

$$J\left[v, \underline{\phi}, \underline{\chi}\right] = F\left[\underline{\phi}\right] - \mathcal{L}\left[v, \underline{\phi}, \underline{\chi}\right]. \tag{B.4}$$

Differentiating the total functional J with respect to the adjoint orbitals $\underline{\chi}$ and normalization multipliers $\{\varepsilon^{m}\}$ gives the standard KS equations

$$0 = \frac{\partial J}{\partial \chi_{\boldsymbol{\alpha}}^{\gamma}}\,\forall\boldsymbol{\alpha},\gamma \;\Rightarrow\; H(v)\,\phi^{m} = E^{m}\phi^{m} \text{ and} \tag{B.5}$$

$$0 = \frac{\partial J}{\partial \varepsilon^{\gamma}}\,\forall\gamma \;\Rightarrow\; \sum_{\mathbf{i}=\mathbf{1}}^{N_{\mathbf{x}}}\phi_{\mathbf{i}}^{m\,*}\phi_{\mathbf{i}}^{m} = 1. \tag{B.6}$$

The adjoint equations are found by differentiating with respect to the KS orbitals and eigenvalues to produce a set of sparse linear equations

$$\begin{bmatrix} \left(\frac{\partial F}{\partial \phi^\gamma}\right)^* \\ \left(\frac{\partial F}{\partial E^\gamma}\right)^* \end{bmatrix} = \begin{bmatrix} H^\dagger(v) - (E^\gamma)^* & \phi^\gamma \\ -(\phi^\gamma)^\dagger & 0 \end{bmatrix} \begin{bmatrix} \chi^\gamma \\ \varepsilon^\gamma \end{bmatrix}. \tag{B.7}$$

After solving the direct and adjoint equations in Eqs. (B.5)-(B.7), the total derivative is given by the expression

$$\frac{\partial J}{\partial v_{\boldsymbol{\alpha},\beta}} = -\frac{\partial \mathcal{L}}{\partial v_{\boldsymbol{\alpha}}} = -2 \sum_{m=1}^{N_{\text{orbs}}} \sum_{\mathbf{i}=\mathbf{1}}^{N_{\mathbf{x}}} \text{Re}\left\{ (\chi_{\mathbf{i}}^m)^* \frac{\partial H(v)}{\partial v_{\boldsymbol{\alpha}}} \phi_{\mathbf{i}}^m \right\}. \tag{B.8}$$

B.2 Time-Dependent Adjoint

The derivatives of the cost functionals F_n and $F_{\mathbf{j}}$ in Eqs. 4.7-4.8 are important quantities needed when using classical optimization routines. In this appendix we show how the discrete-adjoint method can be used to compute this gradient at the cost of a backwards propagation of nonhomogeneous time-dependent Kohn-Sham-like equations. The derivation below is for the F_n cost functional but only Eqs. B.9-B.10 change when using other real-valued cost functionals. The notation used below is similar to that found in Refs. 68, 69 and is summarized in Table B.1.

We begin our derivation by discretizing the cost functional

$$F_n\left[\underline{\phi}\right] = \frac{1}{2} \sum_{n=1}^{N_t} \sum_{\mathbf{i}=\mathbf{1}}^{N_{\mathbf{x}}} \left(\sum_{m=1}^{N_{\text{orbs}}} \phi_{\mathbf{i},n}^{m\,*} \phi_{\mathbf{i},n}^m - \tilde{n}_{\mathbf{i},n} \right)^2 w_{\mathbf{i},n}, \tag{B.9}$$

and taking its first derivative with respect to an arbitrary orbital

$$\frac{\partial F_n}{\partial \phi_{\boldsymbol{\alpha},\beta}^\gamma} = w_{\boldsymbol{\alpha},\beta} \left(\sum_{m=1}^{N_{\text{orbs}}} \phi_{\boldsymbol{\alpha},\beta}^{m\,*} \phi_{\boldsymbol{\alpha},\beta}^m - \tilde{n}_{\boldsymbol{\alpha},\beta} \right) \phi_{\boldsymbol{\alpha},\beta}^{\gamma\,*}, \tag{B.10}$$

where γ is the orbital index, β is the time index, and $\boldsymbol{\alpha} = \alpha_x, \alpha_y, \alpha_z$ is the spatial index. The KS orbitals are constrained to satisfy a discretization of the KS equations by including the Lagrangian

$$\mathcal{L}\left[v, \underline{\phi}, \underline{\chi}\right] = 2\,\mathrm{Re}\left\{\sum_{n=1}^{N_t}\sum_{\mathbf{i}=\mathbf{1}}^{N_{\mathbf{x}}}\sum_{m=1}^{N_{\mathrm{orbs}}} \chi_{\mathbf{i},n}^{m}\left[A\left(v_{,n}\right)\phi_{,n}^{m} - \sum_{p=1}^{N_p} B_p\left(v_{,n-p}\right)\phi_{,n-p}^{m}\right]_{\boldsymbol{i}}^{*}\right\} \tag{B.11}$$

in the total functional

$$J\left[v, \underline{\phi}, \underline{\chi}\right] = F\left[\underline{\phi}\right] - \mathcal{L}\left[v, \underline{\phi}, \underline{\chi}\right]. \tag{B.12}$$

We now take various derivatives of the total functional in Eq. B.12 to derive the total derivative of the cost functional. The forward propagation equations come from a differentiation with respect to the adjoint variables:

$$0 = \frac{\partial J}{\partial \chi_{\boldsymbol{\alpha},\beta}^{\gamma}}\,\forall \boldsymbol{\alpha}, \beta, \gamma \;\Rightarrow\; A\left(v_{,n}\right)\phi_{,n}^{m} = \sum_{p=1}^{N_p} B_p\left(v_{,n-p}\right)\phi_{,n-p}^{m}, \tag{B.13}$$

where $n = 1, \ldots, N_t$, $m = 1, \ldots, N_{\mathrm{orbs}}$, and N_p is the number of steps in a multistep discretization of the time-dependent Kohn-Sham (TDKS) equations with the generic operators A and $\{B_p\}$. The adjoint equations come from a differentiation with respect to the KS orbitals:

$$\begin{aligned} 0 = \frac{\partial J}{\partial \phi_{\boldsymbol{\alpha},\beta}^{\gamma}} = \frac{\partial F}{\partial \phi_{\boldsymbol{\alpha},\beta}^{\gamma}} - \frac{\partial \mathcal{L}}{\partial \phi_{\boldsymbol{\alpha},\beta}^{\gamma}} \Rightarrow \frac{\partial \mathcal{L}}{\partial \phi_{\boldsymbol{\alpha},\beta}^{\gamma}} = \frac{\partial F}{\partial \phi_{\boldsymbol{\alpha},\beta}^{\gamma}} \\ \Rightarrow A\left(v_{,n}\right)^{\dagger}\chi_{,n}^{m} = \left(\frac{\partial F}{\partial \phi_{,n}^{m}}\right)^{*} + \sum_{p=1}^{N_p} B_p\left(v_{,n-p}\right)^{\dagger}\chi_{,n+p}^{m}, \end{aligned} \tag{B.14}$$

where $\chi^m_{,n} = 0$ for all $n > N_t$. After solving for the KS and adjoint orbitals in Eqs. B.13 and B.14 we can find the total derivative using the expression

$$\frac{\partial J}{\partial v_{\boldsymbol{\alpha},\beta}} = -\frac{\partial \mathcal{L}}{\partial v_{\boldsymbol{\alpha},\beta}} = 2\sum_{m=1}^{N_{\text{orbs}}}\sum_{\mathbf{i}=\mathbf{1}}^{N_{\mathbf{x}}} \text{Re}\Bigg\{ -\chi^m_{\mathbf{i},\beta}\left[\frac{\partial}{\partial v_{\boldsymbol{\alpha},\beta}} A\left(v_{,\beta}\right)\phi^m_{,\beta}\right]^*_{\mathbf{i}} + \sum_{p=1}^{N_p} \chi^m_{\mathbf{i},p+\beta}\frac{\partial}{\partial v_{\boldsymbol{\alpha},\beta}} B_p\left(v_{,\beta}\right)\phi^m_{,\beta}\Bigg\}, \quad \text{(B.15)}$$

In the case of complex potentials we replace $\partial/\partial v_{\boldsymbol{\alpha},\beta}$ in Eq. B.15 with $\partial/\partial \,\text{Re}\left(v_{\boldsymbol{\alpha},\beta}\right)$ for the derivative with respect to the real part of the potential and then again with $\partial/\partial \,\text{Im}\left(v_{\boldsymbol{\alpha},\beta}\right)$ for the derivative with respect to the imaginary part.

We conclude this appendix by giving an example of the discrete-adjoint method applied to the Crank-Nicolson discretization of the TDKS equations in one dimension. The operators for this method are $A\left(v_{,n}\right) = \mathbb{I} + \frac{\imath\Delta t}{2} H_n$ and $B\left(v_{,n}\right) = \mathbb{I} - \frac{\imath\Delta t}{2} H_n$, where $H_n = T + V_n$, T is a discretization of the kinetic energy operator, and V_n is a diagonal matrix with the potential $v_{,n}$ along the diagonal. The A operator real derivative is

$$\frac{\partial}{\partial \,\text{Re}\left(v_{\alpha,\beta}\right)} A_{i,j}\left(v_{,n}\right) = \begin{cases} \frac{\imath\Delta t}{2} & \text{if } \alpha = i,j \text{ and } \beta = n \\ 0 & \text{otherwise} \end{cases} \quad \text{(B.16)}$$

and the imaginary derivative is found from the same expression with -1 replacing $\imath$. The real and imaginary derivatives of the B operator are the negatives of the corresponding A operator derivatives.

C. Test Cases

This appendix contains the many formulas used in creating test cases for our density-to-potential inversions. Most of the examples are for noninteracting systems where the orbitals and potentials are known analytically for easier benchmarking as explained in Sec. 1.6. All of the formulas are written in atomic units in the coordinate representation. These examples can be used to test both the direct and inverse problems of density functional theory (DFT).

C.1 Particle in a Box

The one dimensional particle-in-a-box potential $v(x) = 0$

$$v(x) = \begin{cases} 0 & \text{if } 0 < x < L \\ \infty & \text{otherwise} \end{cases} \tag{C.1}$$

has eigenstates

$$\phi_m(x) = \sqrt{\frac{2}{L}} \sin\left(\frac{m\pi x}{L}\right) \tag{C.2}$$

and energies $E_m = \frac{1}{2}\left(\frac{m\pi}{L}\right)^2$, where m is a positive integer. Although somewhat trivial, this example is especially helpful in isolating programming errors associated with the kinetic energy operator. It is also helpful in showing how error patterns affect density-to-potential inversions as explained in Sec. A.1. In N_d dimensions the potential is

$$v(\mathbf{x}) = \begin{cases} 0 & \text{if } 0 < x_i < L_i,\ i = 1, \ldots, N_d \\ \infty & \text{otherwise} \end{cases} \tag{C.3}$$

with corresponding eigenstates

$$\phi_{\mathbf{m}}(\mathbf{x}) = \prod_{i=1}^{N_d} \sqrt{\frac{2}{L_i}} \sin\left(\frac{m_i \pi x_i}{L_i}\right), \tag{C.4}$$

where $\mathbf{m}$ is a N_d-dimensional vector of positive integers.

The particle-in-a-box example also serves as a useful test case for time-dependent systems if the time-dependent Schrödinger equation is modified with a nonhomogeneous term f so that

$$\imath\psi_t = -\frac{1}{2}\Delta\psi + v\psi + f. \tag{C.5}$$

One easily visualized formulation in one dimension is

$$\begin{aligned}
\psi(t,x) &= \sqrt{\frac{2}{L}} \sin\left(\frac{\pi x}{L}\right) \exp\left(\imath g(t)\right), \\
V(t,x) &= \sqrt{\frac{2}{L}} \cos\left(\frac{\pi x}{L}\right) \sin\left(\omega_t t\right), \\
f(t,x) &= -\left(\frac{\mathrm{d}}{\mathrm{d}t} g(t) + \frac{\omega_x^2}{2} + V(t,x)\right) \psi(t,x),
\end{aligned}$$

where $g(t) = t$ or t^2. (This formulation uses the ground state but other eigenstates are equally valid.) This can be generalized to multiple dimensions and serves as a useful test case for time-dependent propagation code.

C.2 Simple Harmonic Oscillator

The simple harmonic oscillator is a standard example given in most quantum mechanics texts. [4] The potential in one dimension is $v(x) = \frac{1}{2}x^2$ and the energies are $E_m = m + \frac{1}{2}$ for all nonnegative integers m. The first three eigenstates are

$$\psi_0(x) = \pi^{-1/4} e^{-\frac{x^2}{2}}, \tag{C.6}$$

$$\psi_1(x) = \frac{\sqrt{2}x}{\pi^{1/4}} e^{-\frac{x^2}{2}}, \text{ and} \tag{C.7}$$

$$\psi_2(x) = \frac{(2x^2 - 1)}{\sqrt{2}\pi^{1/4}} e^{-\frac{x^2}{2}}. \tag{C.8}$$

Simple time-dependent test cases using the harmonic potential can be formed through the use of the harmonic potential theorem described in Ref. 78. Although typically used when modeling interacting systems, target densities can also be formed using a sum of densities from noninteracting electrons satisfying the harmonic potential theorem. Section. 4.4.1 shows one particular noninteracting example formed from the orbitals

$$\phi_i(t, x) = \psi_i[x - x_s(t)] \exp\{\imath[\dot{x}_s(t)\, x - S(t) - E_i t]\}, \tag{C.9}$$

where

$$A = \frac{F_0}{1 - \omega^2}, \tag{C.10}$$

$$x_s(t) = A \sin(\omega t), \tag{C.11}$$

$$v(t, x) = \frac{1}{2}x^2 - F_0 \sin(\omega t)\, x, \text{ and} \tag{C.12}$$

$$S(t) = \frac{A^2}{2}\left\{\omega^2\left[\frac{t}{2} + \frac{\sin(2\omega t)}{4\omega}\right] - \left[\frac{t}{2} - \frac{\sin(2\omega t)}{4\omega}\right]\right\} \text{ if } t_0 = 0. \tag{C.13}$$

VITA

VITA

Daniel S. Jensen

Education

Physics — **Purdue University**
Ph.D., GPA: 3.90 — *2010–2016*

Physics — **Brigham Young University**
M.S., GPA: 3.79 — *2007–2010*

Mathematics and Physics — **Brigham Young University**
B.S., GPA: 3.93 — *2000–2007*

Doctoral Dissertation

Title: *Density-to-Potential Inversions in Density Functional Theory*

Supervisor: Adam Wasserman

Description: Implementation of multilevel PDE-constrained inversion methods for density functional theories

Master's Thesis

Title: *Real-space Time-domain Approach to Time Dependent Current Density Functional Theory*

Supervisor: Bret C. Hess

Description: Implementation of time-dependent current density functional theory for studying optical properties of periodic structures

Employment History

Purdue Chemistry Department — **West Lafayette, IN**
Research Assistant — *2012–2016*

Purdue Physics Department — **West Lafayette, IN**
Teaching Assistant — *2010–2012*

BYU Physics Department **Provo, UT**
Teaching Assistant *2007–2010*

BYU Physics Department **Provo, UT**
Research Assistant *2004–2007*

StageRight **Clare, MI**
Information Systems Assistant *2000, 2003*

Computer Skills

OS: **Linux**, Windows

Languages: C, **Fortran** (including MPI and OpenMP bindings), HTML, Java, LaTeX, **Python**, and Unix shell scripting (Bash)

Numerical: Matlab, NumPy, Octave, **SciPy**

Symbolic: Maple, Mathematica, Maxima, SymPy

RCS: CVS, GIT, SVN

Build: distutils, CMake, make

DFT Codes: Fireball, Octopus, NWChem

Languages

English: Native

Spanish: Limited working proficiency

Publications

[1]D. S. Jensen and A. Wasserman, "Numerical density-to-potential inversions in time-dependent density functional theory", Physical Chemistry Chemical Physics (2016) 10.1039/C6CP00312E.

[2]P. Elliott, D. Jensen, A. Wasserman, and K. Burke, "Comment on "Application of partition density-functional theory to one-dimensional models"", Physical Review A **89**, 026501 (2014).

[3]M. A. Mosquera, D. Jensen, and A. Wasserman, "Fragment-Based Time-Dependent Density Functional Theory", Physical Review Letters **111**, 023001 (2013).

[4]B. C. Hess, D. S. Jensen, and I. G. Okhrimenko, "Spatial distribution of electron densities during optical excitation of C_{60}", Journal of Physics: Condensed Matter **22**, 445502 (2010).

Achievements

2014: MCC Travel Grant for the 6th Time-Dependent Density-Functional Theory: Prospects and Applications School and Workshop

Spring 2013: Computational Science and Engineering Student Conference tie for first-place graduate talk

Winter 2009: Outstanding Lab TA

2003–2004: BYU full-tuition scholarship

2000, 2005: BYU half-tuition scholarship

2000: Valedictorian, Clare High School

1997: Eagle Scout Award, Boy Scouts of America

Specialty Courses

Purdue University

- Computational Biomolecular Phys (570)
- Quantum Mechanics I (660)
- Quantum Mechanics II (661)
- Statistical Mechanics (617)
- Quantum Computing (526)
- Meth Theoret Phys IIIB (603)

Brigham Young University

- Physics 641: Mathematical Theory of Electricity and Magnetism
- Physics 642: Mathematical Theory of Electricity and Magnetism

Presentations

Oct 2015: *Density-to-Potential Inversions in TDDFT*, The International Workshop on Quantum Control of Light and Matter (Purdue Quantum Center Kickoff), Purdue University, West Lafayette, IN, USA (poster)

Jun 2014: *Fragment-based Time-dependent Density-functional Theory*, Midwest Theoretical Chemistry Conference, Northwestern University, Evanston, IL, USA (poster)

Mar 2014: *Density-to-Potential Inversions in TDDFT*, American Physical Society March meeting, Denver, CO, USA (poster)

Jan 2014: *Density-to-Potential Inversions in TDDFT and P-TDDFT*, 6th Time-Dependent Density-Functional Theory: Prospects and Applications meeting, Centro de Ciencias de Benasque Pedro Pascual, ES (poster)

Sep 2013: *Fragment-based Time-dependent Density-functional Theory*, 246th American Chemical Society meeting, Indianapolis IN (talk)

Aug 2013: *Density-to-Potential Inversions in Fragment-based TDDFT*, Time-Dependent Density-Functional Theory Gordon Research Conference, University of New England, Biddeford, ME, USA (poster)

May 2013: *Fragment-based Time-dependent Density-functional Theory*, Midwest Theoretical Chemistry Conference, University of Illinois at Urbana-Champaign, Urbana, IL, USA (poster)

Apr 2013: *Fragment-based Density-functional Theory*, 5th Computational Science and

Engineering Student Conference, Purdue University, West Lafayette, IN, USA

Jun 2012: *Adiabatic Approximations in Time-dependent Partition Density Functional Theory*, Midwest Theoretical Chemistry Conference, University of Wisconsin-Madison, Madison, WI, USA (poster)